

APPLICATION OF ELECTRICAL  
CAPACITANCE TOMOGRAPHY IMAGE  
RECONSTRUCTION ALGORITHMS TO  
REAL DATA

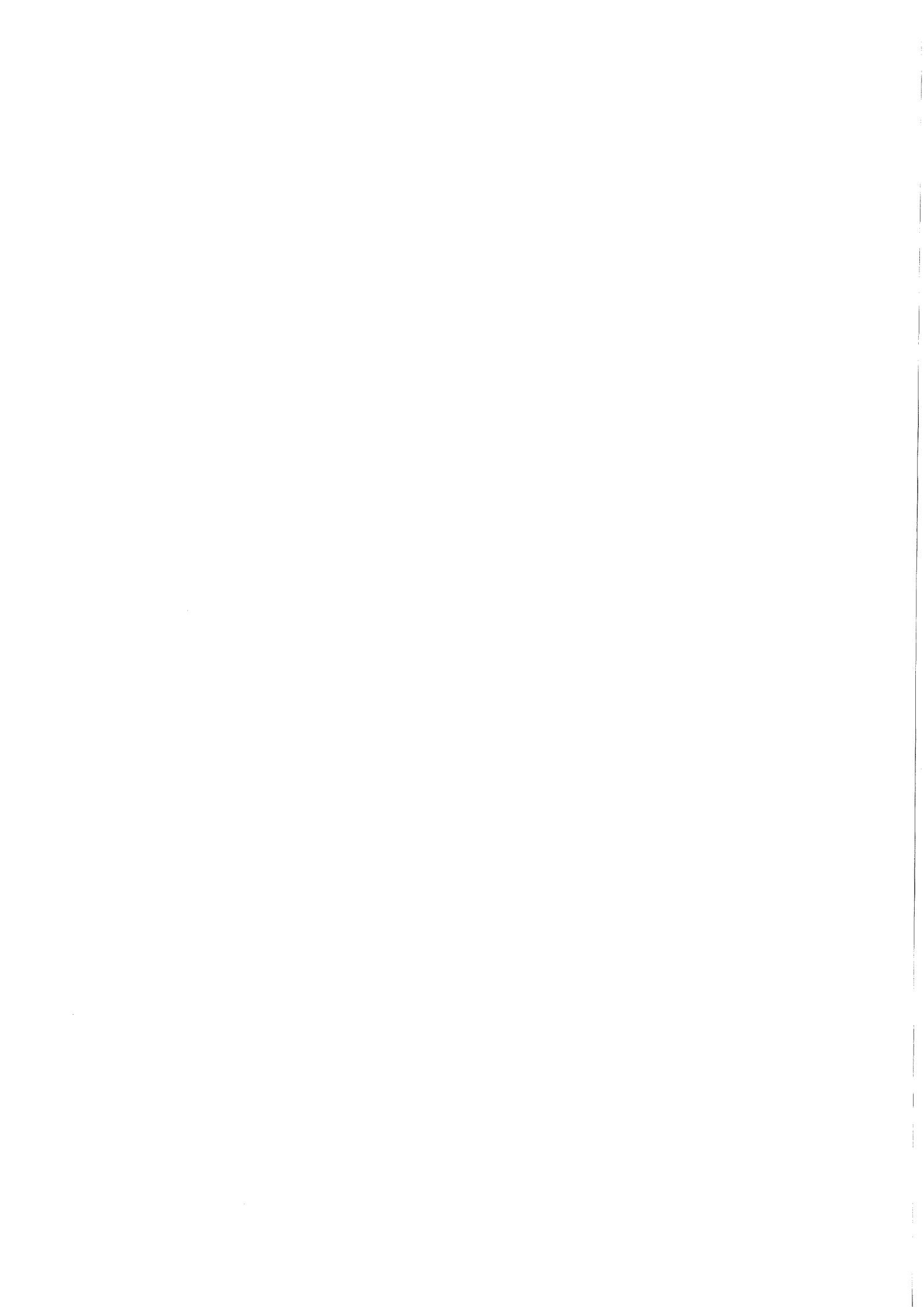
J.W.W. Mulder

Delft University of Technology  
Department of Applied Physics

Delft, October 1997

Kramers Laboratorium voor  
Fysische Technologie  
Prins Bernhardlaan 6  
2628 BW Delft

Professor: prof. dr.ir. H.E.A. van den Akker  
Supervisors: dr. R.F. Mudde  
Dipl-Ing. F.T. Kühn



# Summary

Electrical capacitance tomography (ECT) has recently been developed for the in-situ measurement of the cross-sectional gas-solid distribution in a duct carrying a non-conductive 2-phase flow. The technique relies on the detection of electrical capacitances between electrodes placed on the periphery of the duct. The data depend on the permittivity distribution inside the cross-section, which has to be reconstructed. Information on the flow regime, vector velocity, and gas-solid distribution in process vessels and pipelines can be determined from the reconstructed images.

The main bottleneck is still the poor quality of the image reconstruction part. In the frame of the ECT project at Delft University of Technology (DUT), research is done towards a new direct reconstruction algorithm, based on the least squares solution.

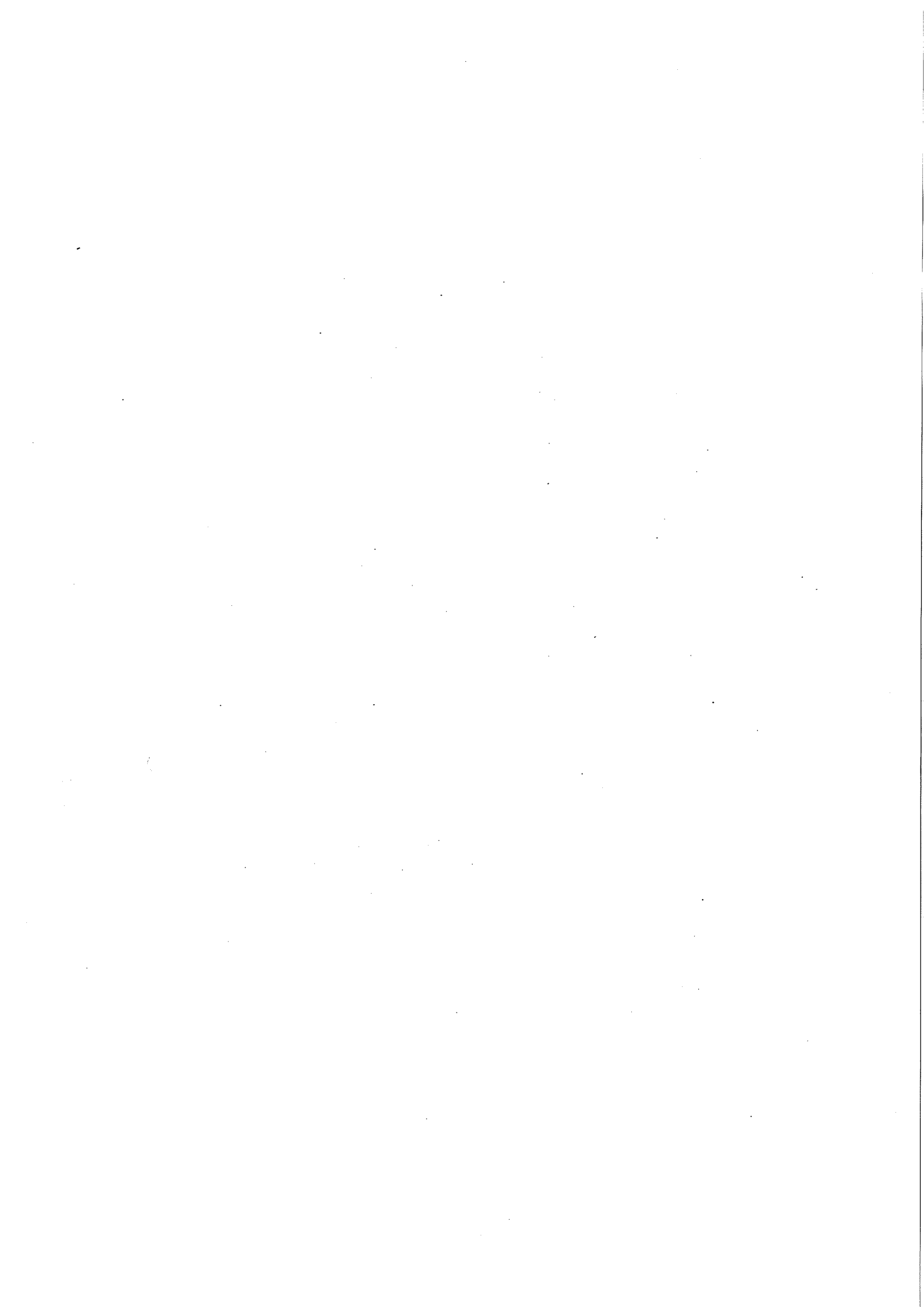
The investigation has two goals. The investigation of the influence of noise on the data and the reconstruction of the permittivity distribution from measured data using well known material distributions as test cases to determine the spatial resolution.

To investigate the influence of noise on the reconstruction, simulated noise is added to synthetic data. The reconstructions show that the more constraints are added to the least squares solution, the more robust the algorithm becomes. Noise measurements show that the noise level of real measured data has a negligible influence on the constrained least squares reconstruction.

Reconstruction of a rod (about  $\frac{1}{6}$  of the pipe diameter) near the wall of the sensor is possible. In the centre region of the pipe the quality of the reconstructed image decreases due to the under-determinacy in the centre of the pipe.

Two rods can be reconstructed when both positioned close to the pipe-wall. However, they can not be seen separately in the centre region and when they are close to one another.

Bubbles (about  $\frac{1}{10}$  of the pipe diameter) are hard to reconstruct when positioned in the pipe centre. Due to their finite height 3-D effects disturb the interpretation of the measurements. The bubbles, however, can be detected when looking at the raw data.



# Samenvatting

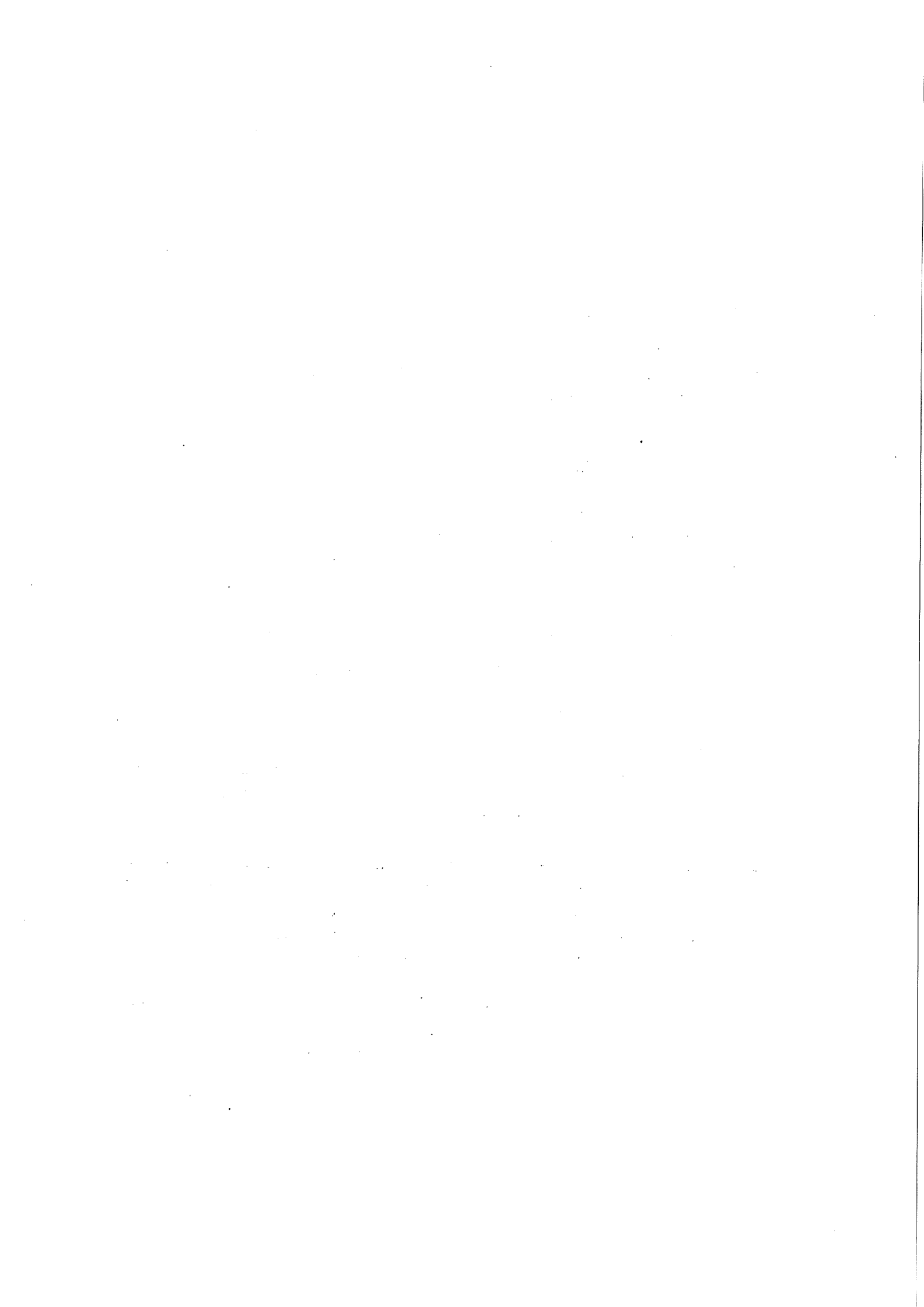
Recentelijk is *Electrical Capacitance Tomography* (ECT) ontwikkeld voor het meten van gas-vaste stof verdelingen in een buis met een niet-geleidende 2-fasen stroming. De techniek maakt gebruik van elektrische capaciteitsmetingen tussen electrodes die om de buitenkant van de buis zijn geplaatst. De data hangen af van de permittiviteits-verdeling in de doorsnede die moet worden gereconstrueerd. Informatie over het stromingsregime, snelheden en gas-vaste stof verdeling in proces vaten en pijpleidingen kunnen worden bepaald uit de gereconstrueerde doorsneden.

Het grootste probleem is nog steeds de slechte kwaliteit van het reconstructie gedeelte. Binnen het kader van het ECT project aan de Technische Universiteit Delft werd onderzoek gedaan naar een nieuw direct reconstructie algoritme, gebaseerd op de kleinste kwadraten methode.

Het doel van dit onderzoek is tweeledig: onderzoek naar de invloed van meet ruis op de reconstructie en de reconstructie van de permittiviteits verdeling uit gemeten data van vooraf bekende materiaal verdelingen om het oplossend vermogen te bepalen.

Om de invloed van ruis op de reconstructie te onderzoeken is er ruis toegevoegd aan gesimuleerde data. De reconstructies laten zien dat hoe meer beperkingen aan de kleinste kwadraten oplossing worden toegevoegd, hoe robuuster het algoritme wordt. Ruismetingen tonen aan dat het ruisniveau van echte, gemeten data een verwaarloosbare invloed heeft op de ingeperkte kleinste kwadraten reconstructie.

De reconstructie van een staaf (ca.  $\frac{1}{6}$  van de buis diameter) dichtbij de wand van de sensor is mogelijk. In het midden van de sensor daalt de kwaliteit van de reconstructie als gevolg van de onder-bepaaldheid van het probleem in het midden van de sensor. Twee staven kunnen worden gereconstrueerd als ze beide dichtbij de wand zijn gepositioneerd. Echter, ze kunnen niet afzonderlijk worden gezien in het midden gebied van de buis en wanneer ze dicht bij elkaar zijn gepositioneerd. Bellen (ca.  $\frac{1}{10}$  van de buis diameter) zijn moeilijk te reconstrueren wanneer ze zich in het midden gebied van de sensor bevinden. Door hun eindige afmetingen in axiale richting verstoren 3-D effecten de interpretatie van de metingen. De bellen kunnen overigens wel gedetecteerd worden, wanneer naar de ruwe data wordt gekeken.



# Contents

Summary	i
Samenvatting	iii
Contents	v
<b>1 Introduction</b>	<b>1</b>
1.1 Tomographic Technology . . . . .	1
1.2 Electrical capacitance tomography . . . . .	3
1.3 Aim of this project . . . . .	4
1.4 Structure of this report . . . . .	4
<b>2 The electrical capacitance tomography problem</b>	<b>5</b>
2.1 Introduction . . . . .	5
2.2 Capacitance sensor . . . . .	5
2.3 The forward problem and the inverse problem . . . . .	6
2.3.1 Forward problem . . . . .	6
2.3.2 Inverse problem . . . . .	8
<b>3 Simulations</b>	<b>11</b>
3.1 Introduction . . . . .	11
3.2 Implementation of the ECT problem in SEPRAN . . . . .	11
3.2.1 The forward problem . . . . .	11
3.2.2 General mathematical formulation of the sensor model . . . . .	12
3.2.3 Pipe geometry . . . . .	12
3.2.4 Boundary values . . . . .	14
3.2.5 Discrete numerical solution of the forward problem using SEPRAN .	15

3.3	Principal components analysis . . . . .	16
3.3.1	Introduction . . . . .	16
3.3.2	Over- and under-determinacy . . . . .	16
3.3.3	Singular value decomposition . . . . .	16
3.3.4	SCREE test . . . . .	18
3.3.5	Pixel shape . . . . .	19
3.4	Simulations using SEPRAN . . . . .	20
3.4.1	Simulation of the 12 electrode system . . . . .	20
3.4.2	Upgrading to an 16 electrode system . . . . .	21
3.4.3	Comparison of the sensitivity of the 12 electrode and 16 electrode system . . . . .	24
3.4.4	A new view on the 12 electrode system . . . . .	26
3.5	Conclusions of the simulations . . . . .	28
3.5.1	Comparison of 12-electrode system with 16-electrode system . . . . .	28
3.5.2	The 12 electrode system using coupled source electrodes . . . . .	28
4	Least squares based reconstruction algorithms . . . . .	29
4.1	Introduction . . . . .	29
4.2	Mathematical model of the capacitance tomography system . . . . .	29
4.2.1	Discrete representation of the permittivity distribution . . . . .	29
4.2.2	Direct reconstruction methods . . . . .	30
4.2.3	Linearisation of the ECT problem . . . . .	30
4.3	Least squares based reconstruction methods . . . . .	31
4.3.1	Euclidean norm . . . . .	31
4.3.2	General linear least squares solution . . . . .	32
4.3.3	Linear least squares derivatives . . . . .	33
4.3.4	Hybrids of least squares derivatives . . . . .	35
5	Noise in ECT sensor electronics . . . . .	37
5.1	Introduction . . . . .	37
5.2	The UMIST system and the DUT system . . . . .	37
5.2.1	The UMIST system . . . . .	37
5.2.2	The DUT system . . . . .	38
5.2.3	The two circuits . . . . .	38

5.3	Noise measurements . . . . .	40
5.3.1	Signal to noise ratio . . . . .	40
5.3.2	Experimental system . . . . .	40
5.4	Results . . . . .	41
5.4.1	UMIST electronics . . . . .	41
5.4.2	DUT electronics . . . . .	42
5.4.3	DUT electronics versus UMIST electronics . . . . .	44
5.5	Conclusions . . . . .	44
<b>6</b>	<b>Robustness of the least squares inversion methods</b>	<b>45</b>
6.1	Introduction . . . . .	45
6.2	Definition of the $SS_{mod}$ and the $SS_{res}$ . . . . .	45
6.2.1	General definition of a norm . . . . .	45
6.2.2	Definition of the $SS_{mod}$ . . . . .	46
6.2.3	Definition of the $SS_{res}$ . . . . .	46
6.2.4	Is there a relation between the $SS_{mod}$ and $SS_{res}$ ? . . . . .	46
6.3	Definition of the test cases . . . . .	48
6.4	Reconstructions without adding noise . . . . .	48
6.5	Results achieved when adding simulated noise . . . . .	50
6.5.1	Adding noise to the exact calculated capacitances . . . . .	50
6.5.2	Influence of noise on the linear least squares solution . . . . .	51
6.5.3	Influence of noise on the constrained least squares solution . . . . .	52
6.6	Discussion of $SS_{mod}$ and $SS_{res}$ . . . . .	53
6.7	Conclusions . . . . .	54
<b>7</b>	<b>Reconstructions with least squares based methods</b>	<b>57</b>
7.1	Introduction . . . . .	57
7.2	Measurement system . . . . .	57
7.2.1	Capacitance sensor . . . . .	57
7.2.2	Data acquisition module . . . . .	59
7.2.3	Computer system and software . . . . .	59
7.2.4	Calibration . . . . .	59
7.3	Measurements . . . . .	59
7.3.1	The used permittivity components. . . . .	59

7.3.2	The objects to be measured . . . . .	60
7.4	Reconstructions of real measurements . . . . .	60
7.4.1	The 10 cm sensor . . . . .	60
7.4.2	The 40 cm sensor . . . . .	63
7.4.3	The 30 cm sensor . . . . .	65
7.5	Reconstructions using different Jacobian matrices . . . . .	68
7.6	Phillips-Towmey damping . . . . .	70
7.7	Noise in the three sensors . . . . .	75
7.8	Conclusions . . . . .	76
<b>8</b>	<b>Sensitivity of the capacitance sensor</b>	<b>79</b>
8.1	Introduction . . . . .	79
8.2	Measurement setup . . . . .	79
8.2.1	Aim of the measurements . . . . .	79
8.2.2	The phantoms . . . . .	80
8.3	Measurements . . . . .	80
8.3.1	The 10 cm Sensor . . . . .	81
8.3.2	The 30 cm Sensor . . . . .	81
8.4	The 40 cm sensor . . . . .	86
8.5	Conclusions . . . . .	86
<b>9</b>	<b>Conclusions and recommendations</b>	<b>89</b>
9.1	Conclusions . . . . .	89
9.1.1	The simulations . . . . .	89
9.1.2	Noise measurements . . . . .	90
9.1.3	Addition of simulated noise . . . . .	90
9.1.4	Reconstructions . . . . .	91
9.1.5	Sensitivity of the capacitance system . . . . .	92
9.2	Recommendations . . . . .	92
<b>A</b>	<b>Appendix A</b>	<b>95</b>
<b>B</b>	<b>Matlab scripts, conversion program ptl.c and circ.pl</b>	<b>97</b>
B.1	Matlab scripts . . . . .	97

B.2	ptl.c	101
B.3	circ.pl	104
C	Capacitance measurements from simulations in SEPRAN	107
C.1	Capacitance measurements	107
D	Mesh-input file for the 16 electrode mesh	113
	Bibliography	121



# Symbols

## Roman symbols

Symbol	quantity	dimension
A	main block of smoothing matrix R	—
B	main block of smoothing matrix R	—
C	main block of smoothing matrix R	—
$C_{i,scaled}$	normalised capacitance	—
$C_{ij}^{norm}$	normalised capacitance from the UMIST electronics	—
$C_{empty}$	capacitance when the sensor is empty	F
$C_{full}$	capacitance when the sensor is full	F
$C_{\epsilon_1}$	capacitance when the sensor is filled with the lower permittivity material	F
$C_{\epsilon_2}$	capacitance when the sensor is filled with the higher permittivity material	F
c	data vector carrying the capacitances	F
$\bar{c}$	mean capacitance	F
$c_i$	$i^{th}$ element of the capacitance vector	F/m
$C_{ij}$	capacitance between electrode i and j	F
$c_{i,j}$	capacitance between electrode i and j	F
$c_i^{meas}$	measured capacitance	F
$c_i^{pre}$	capacitance calculated from the forward solution	F/m
D	electric flux density	Cm <sup>-2</sup>
E	electric field strength	Vm <sup>-1</sup>
$E$	overall error	Fm <sup>-1</sup>
e	distance between measured data and predicted data	F
$e_1, e_2$	offset voltage	V
f	frequency	s <sup>-1</sup>
J	jacobian matrix	Fm <sup>-1</sup>
$J_{ij}$	first derivative of datum i with respect to parameter p	Fm <sup>-1</sup>
j	$j^{th}$ ring of the reconstruction mesh	—
$j_i$	$i^{th}$ row of the jacobian matrix	Fm <sup>-1</sup>
L	diagonal matrix carrying singular values	V
$l_{ax}$	axial electrode length	m
$l_j$	line over electrode j	m

$M$	number of model parameters	—
$N$	number of electrodes	—
$\mathbf{n}$	normal outward pointing vector	—
$\mathbf{n}_e$	error vector	$Fm^{-1}$
$n$	pixel size exponent	—
$P$	electric polarisation	$Cm^{-2}$
$p$	number of rings	—
$Q$	electric charge	$C$
$Q_j$	electric charge on electrode $j$	$C$
$R$	damping matrix to achieve solution smoothness	—
$R_1, R_2, R_3$	dimensions of the sensor	$m$
$R_1, R_2, R_3$	resistances used in the active differentiator circuit	$\Omega$
$R_f$	feedback resistance used in the charge transfer circuit	$\Omega$
$r_{ij}$	correlation coefficient	—
$r$	radius of	$m$
$r_{max}$	half the inner pipe diameter	$m$
$S$	covariance matrix	$F^2M^{-2}$
$SS_{mod}$	sum of squares of the differences between the presumed and the reconstructed parameters	—
$SS_{res}$	misfit of the model	$F^2m^{-2}$
$s_i$	standard deviation of datum $i$	$Fm^{-1}$
$s_{ij}$	covariance of datum $i$ and $j$	$F^2m^{-2}$
$U$	orthogonal matrix carrying singular vectors	—
$u_i$	$i^{th}$ singular vector	—
$V$	random matrix	—
$V$	electric potential	$V$
$V_{out}$	output voltage of the active differentiator circuit	$V$
$V_1, V_2$	output voltage of the charge transfer circuit	$V$
$V_{ij}$	potential difference between electrode $i$ and electrode $j$	$V$
$W_e$	weighting matrix	$m^2F^{-2}$

## Greek symbols

Symbol	quantity	dimension
$\beta$	smoothing factor	—
$\Gamma_i$	surface of electrode $i$	$m^2$
$\Gamma_s$	surface of the outer surface	$m^2$
$\delta$	Kronecker delta	—
$\epsilon$	permittivity vector	—
$\epsilon$	permittivity	$Fm^{-1}$
$\epsilon_i$	$i^{th}$ element of the permittivity vector	—
$\epsilon_0$	permittivity of free space	$Fm^{-1}$
$\epsilon_r$	relative permittivity	—

$\epsilon_{basis}$	relative permittivity being the basis for perturbations when calculating the Jacobian matrix	—
$\epsilon_{high}$	relative permittivity of the higher permittivity material	—
$\epsilon_{low}$	relative permittivity of the lower permittivity material	—
$\rho$	total charge density	$Cm^{-3}$
$\rho_f$	free charge density	$Cm^{-3}$
$\Phi$	objective function	$F^2m^{-2}$
$\phi$	potential	$V$
$\Psi^i$	potential on parts of the boundary	$V$
$\sigma_i$	standard deviation of datum i	$Fm^{-1}$
$\sigma_{i,normalised}$	normalised standard deviation of datum i	—

## Other

Symbol	Meaning
<i>ECT</i>	Electrical Capacitance Tomography
<i>PC</i>	Principal component
<i>PCA</i>	Principal Component Analysis
<i>SNR</i>	Signal to Noise Ratio



# List of Tables

3.1	Geometry parameters of the sensors used for the noise measurements . . . .	14
5.1	Geometry parameters of the sensors used for the noise measurements . . . .	41
5.2	Relative standard deviation of the noise when averaging over subsequent measurements. N represents the number of measurements in one segment. .	43
5.3	Relative standard deviation of the noise when smoothing using previous and subsequent measurements. N represents the number of measurement used for smoothing. . . . .	44
6.1	$SS_{mod}$ and $SS_{res}$ of the different least squares based solutions of the three phantom distributions. . . . .	49
7.1	Geometry parameters of the sensors used for the noise measurements . . . .	58
8.1	Diameters of the rods used to investigate the smallest object detectable in the capacitance sensor. . . . .	80
8.2	Diameters of the smallest rods detectable in the three capacitance sensors. .	86



# List of Figures

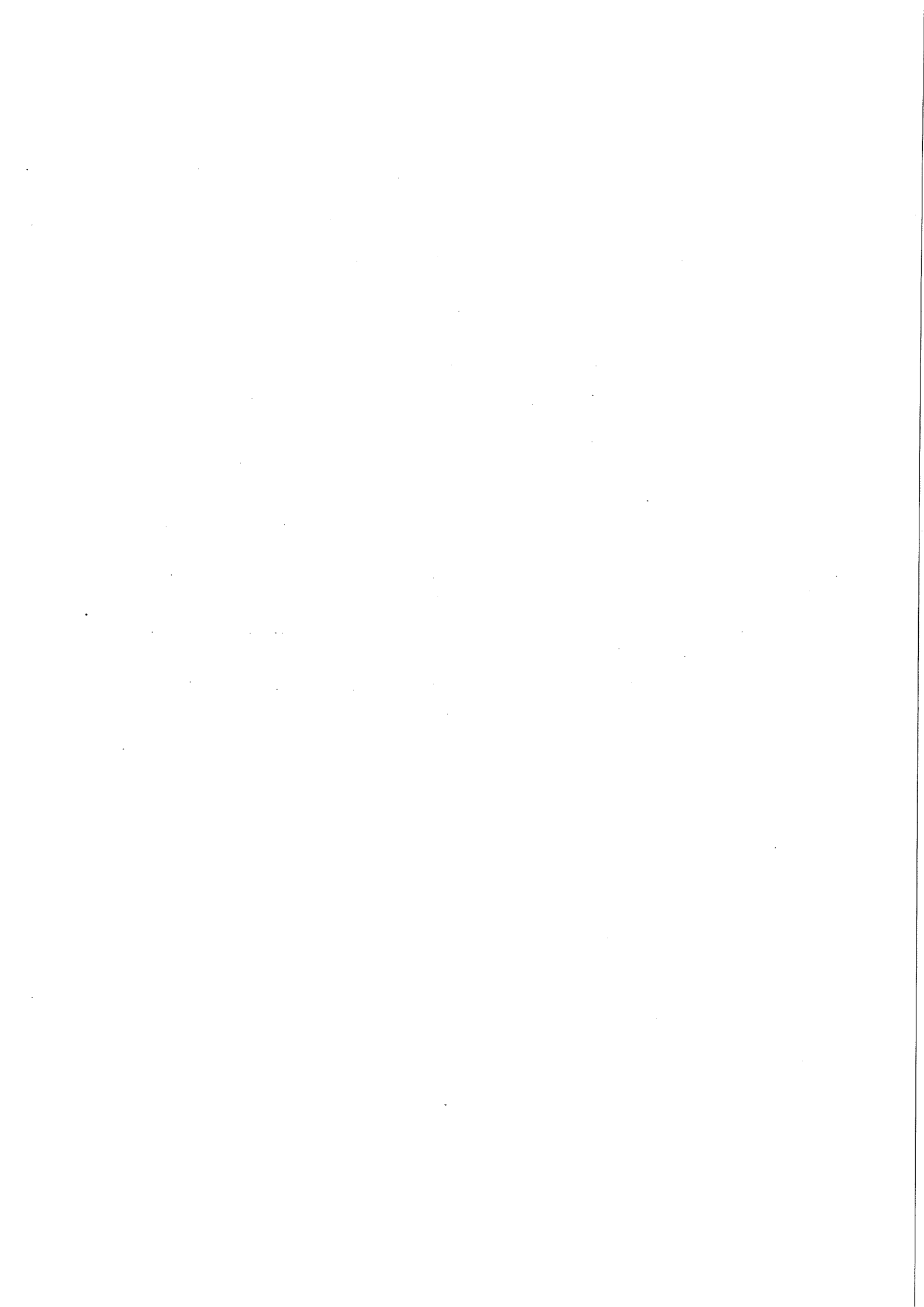
1.1	Different tomographic techniques. . . . .	2
1.2	A capacitance based pipe flow imaging system. Electrodes are mounted circumferentially around the pipe. The measurements and data acquisition are done by the sensor electronics and the data acquisition unit. The data are sent to the control and data processing unit for reconstruction and image presentation. . . . .	3
2.1	Cross-section of the ECT system. . . . .	6
2.2	the ECT sensor. . . . .	7
3.1	How to calculate the capacitance values for a given distribution $\epsilon(x, y)$ . . .	11
3.2	2-dimensional geometry of the electrical capacitance tomography sensor. . .	13
3.3	Pie shaped segment of the sensor geometry. Rotation of this segment results in the total sensor geometry. The numbers in the figure refer to the curve numbers. . . . .	13
3.4	Plot of the potential gradient calculated by SEPRAN. To get accurate estimates of the capacitances of neighbouring electrodes, the mesh has to be refined there where the potential gradient is large. . . . .	14
3.5	The pipe geometry of the 2-dimensional capacitance sensor, when the pie-shaped segment is rotated N times over $\frac{2\pi}{N}$ . . . . .	15
3.6	The line integration over the 'detecting' electrode, resulting in the total charge found on the detecting electrode . . . . .	15
3.7	PCA plots of non correlated data (a) and correlated data (b) . . . . .	18
3.8	Example of the SCREE test, which is a graphical technique to define the number of retained PC's when performing a principal components analysis. . . . .	18
3.9	Polar pixel distribution in the cross-section of the capacitance sensor. . . . .	19
3.10	Condition number of the Hessian matrix as a function of the pixel size exponent n. . . . .	20
3.11	Principal components analysis of a 12 electrodes system with one source electrode. . . . .	22

3.12	Principal Components Analysis of the 16 electrodes system with one source electrode. . . . .	23
3.13	First and second eigenvector of the 16 electrodes system. . . . .	24
3.14	Third and fourth eigenvector of the 16 electrodes system. . . . .	25
3.15	Principal components analysis of the 16 electrode system with one source electrode when omitting adjacent electrode measurements and when omitting opposite electrode measurements. . . . .	26
3.17	Permittivity distribution in the cross-section. . . . .	26
3.16	Principal components analysis of the 12 and 16 electrode system with one source electrode. . . . .	27
3.18	PCA of 12 electrodes system with coupled source electrodes. . . . .	27
4.1	Two different smoothing ways when using the damped least squares solution	34
5.1	The charge transfer principle used in the electrical capacitance tomography system developed by UMIST. . . . .	38
5.2	The capacitance to voltage transducer, developed at the DUT. The unknown capacitance $C_x$ is used as an element in an active differentiator. . . . .	39
5.3	Circuit providing the input signal, $V_{in}$ , to the measurement electrode $C_x$ . . . . .	39
5.4	Cross-section of the two ECT sensors used for the noise measurements. . . . .	40
5.5	Histogram of the noise measured between electrode 1 and electrode 7 using the UMIST electronics. . . . .	41
5.6	Histogram of the noise measured between electrode 1 and electrode 7 using the DUT electronics. . . . .	43
6.1	General interpretation of the $SS_{mod}$ (a) and the $SS_{res}$ (b). . . . .	47
6.2	plots of the presumed phantom distributions: (a) the core flow (a), The pie-shaped segment (b), and the 'dart-board' like distribution (c). Black refers to a permittivity value of 2, white refers to a permittivity value of 1. . . . .	48
6.3	Reconstructions of the phantom distributions when no noise is added, using the constrained least squares solution. . . . .	49
6.4	Reconstruction of phantom distribution 3 when no noise is added, using the weighted least squares solution. . . . .	50
6.5	$SS_{mod}$ (a) and $SS_{res}$ (b) as a function of the noise level for the linear least squares solution. . . . .	51
6.6	$SS_{mod}$ (a) and $SS_{res}$ (b) as a function of the noise level for the constrained least squares solution . . . . .	53

6.7	Reconstructions of test case 2, adding different noise levels in % of the minimum signal, using the constrained least squares solution. . . . .	54
6.8	Example of the permittivity values of pixel 1 and pixel 2 as a function of the noise level for the constrained least squares solution of test case 2 . . .	55
7.1	Electrical capacitance tomography system used to perform capacitance measurements and test the inverse algorithms. . . . .	58
7.2	Plots of the position of a single rod in the 10 cm sensor. The exact positions are depicted in the left sub-figures (a), (c) and (e). The corresponding reconstructions using the constrained least squares method in sub-figures (b), (d) and (f) . . . . .	61
7.3	Plots of the position of a single rod in the 10 cm sensor. The exact positions are depicted in the left sub-figures (a) and (c). The corresponding reconstructions using the constrained least squares method in sub-figures (b) and (d). . . . .	62
7.4	Plots of the positions of two phantoms in the 10 cm sensor. The exact positions are depicted in the left sub-figures (a), (c), (e) and (g), and their reconstructions using the constrained least squares method, (b), (d), (f) and (h) . . . . .	64
7.5	Plots of the positions of two phantoms in the 10 cm sensor. The exact positions are depicted in sub-figures (a), (c), (e), (g) and (i), and their reconstructions using the constrained least squares method, (b), (d), (f), (h) and (j). . . . .	65
7.6	Plots of the positions of one phantom in the 40 cm sensor. The exact positions are depicted in the left sub-figures (a), (c), (e) and (g), and their reconstructions using the constrained least squares method, (b), (d), (f) and (h). . . . .	66
7.7	Reconstruction of the empty pipe data. Since the calibration data are not that accurate, the reconstruction of the empty pipe data gives false estimates for some permittivity values, as can be seen from sub-figure (b). .	67
7.8	Reconstruction of the rod in the 40 cm, after subtraction of the empty pipe data. The positions refer to the . . . . .	68
7.9	Plots of the capacitance values when a 'bubble' passes the through the cross-section of the sensor. The bubble passes the middle of electrode 12 and rises along the wall. . . . .	69
7.10	Plots of the capacitance values when a 'bubble' passes the through the cross-section of the sensor. The centre of the bubble passes electrode 12 at 5cm from the sensor wall. . . . .	70
7.11	Plots of the capacitance values when a 'bubble' passes the through the cross-section of the sensor. The centre of the bubble passes electrode 12 at 10cm from the sensor wall. . . . .	71

7.12	Reconstructions of a bubble rising near the wall: just before the bubble is in the 'measuring cross-section', (a), (d) and (g), when the bubble is in the 'measuring cross-section' (b), (c), (e), (f), (h) and (i). Figures (a), (b) and (c) refer to the situation when the bubble rises along the sensor wall, Figures (d), (e) and (f) to the situation when the centre of the bubble is at 5 cm from the sensor wall, and Figures (g), (h) and (i) to the situation when the centre of the bubble passes at 10 cm from the sensor wall. . . . .	72
7.13	The Jacobian matrix is approximated by finite differences. In this figure the effect on the elements of the Jacobian matrix is illustrated when the derivative is calculated at different positions, i.e. for different values of $\Delta\epsilon_j$ .	73
7.14	Constrained least squares reconstructions of the 64 mm rod at position 1 in the 40 cm sensor using three different Jacobian matrices. Note that the scale of the y-axis of sub-figure (a) differs from the scale of the y-axis of sub-figures (b) and (c). . . . .	74
7.15	Reconstruction of a rod, diameter of 64 mm, in the 40 cm sensor, using the damped constrained least squares method. This damping is accomplished by linking the pixels to one another in radial and axial direction. The effort is to reduce the oscillatory behaviour of the centre pixels due to the underdeterminacy of those pixels. . . . .	75
7.16	Relative standard deviation of the noise for the three sensors (10cm, 30cm and 40cm diameter, when the sensors are filled with polystyrene particles. The standard deviation was calculated from a static measurement of 1000 frames for every sensor. . . . .	76
8.1	Plots of the radial positions of the different rods in the three sensors. Figure (a) the positions in the 10 cm sensor, Figure (b) the positions in the 30 cm sensor and the positions in the 40 cm sensor in Figure (c). . . . .	80
8.2	Plots of the measured capacitances, average over 1000 frames, when a rod (diameter 9mm) is placed at different positions in the 10 cm sensor (a). The rod moves from the centre of the sensor (position 1) to the wall (position 5) with steps of 1 cm. The standard deviation of the capacitance data per position is plotted in subfigure (b). . . . .	82
8.3	The measured capacitances vs the position of the rod (diameter 9mm) in the 10 cm sensor for the electrode combinations $c_{1-2}$ to $c_{1-12}$ . . . . .	83
8.4	Plots of the measured capacitances, average over 1000 frames, when a rod (diameter 25mm) is placed at different radial positions in the 30 cm sensor (a). The rod moves from the centre of the sensor (position 1) to the wall (position 7) with steps of 2 cm. The standard deviation of the capacitance data per position is plotted in subfigure (b). . . . .	84
8.5	The measured capacitances vs the position of the rod (diameter 25mm) in the 30 cm sensor for the electrode combinations $c_{1-2}$ to $c_{1-12}$ . . . . .	85

8.6	Plots of the measured capacitances, average over 1000 frames, when a rod (diameter 33mm) is placed at different positions in the 40 cm sensor (a). The rod moves from the centre of the sensor (position 1) to the wall (position 9) with steps of 2 cm. The standard deviation of the capacitance data per position is plotted in subfigure (b). . . . .	87
8.7	The measured capacitances vs the position of the rod (diameter 33mm) in the 40 cm sensor for the electrode combinations $c_{1-2}$ to $c_{1-12}$ . . . . .	88
A.1	Plots of the reconstructed distributions using the constrained least squares method for the first 6 noise levels added to test case 2 . . . . .	95
A.2	plots of the reconstructed distributions using the constrained least squares method for the last 9 noise levels added to test case 2 . . . . .	96
C.1	Permittivity distribution in the cross-section. . . . .	107
C.2	The sum of charge on the different electrodes for the two different methods explained above. The '*' refer to calculation method 1, the 'o' to calculation method 2. . . . .	108
C.3	The sum of charge on the different electrodes when the cross-section is filled with air (permittivity 1), converted to capacitances values. The '*' refer to calculation method 1, the 'o' to calculation method 2. . . . .	109
C.4	Plots of the Capacitance values $C_{1-2}$ and $C_{1-7}$ , when one pixel is increased from a permittivity 1 to a permittivity 2 in steps of 0.1. . . . .	110
C.5	Equipotential-lines for the permittivity distribution, when one centre pixel is set to a permittivity 2 in an empty pipe, i.e. all other pixel have permittivity 1. . . . .	111



# Chapter 1

## Introduction

*This thesis is the result from a graduation project at the Kramers Laboratorium voor Fysische Technologie (KLFT) of the Faculty of Applied Physics, Delft. At this laboratory research is done towards modelling of single and multi-fluid flow in columns, vessels and other conceivable geometries.*

*These models can be used to control industrial processes, to give a better understanding of the principles of transport phenomena or to improve the design and operation equipment of industrial processes.*

### 1.1 Tomographic Technology

The use of tomography techniques for scientific and industrial applications is becoming widespread and numerous image reconstructions methods have been developed. The techniques used cover almost the whole energy spectrum ranging from high frequencies to low frequencies. For each technique, different operating modes and reconstruction algorithms are used. Tomographic techniques have been used for some time, although applications in engineering and particle processing have become commonplace only more recently.

Tomography is defined as a technique that is able to acquire an image of the distribution of components from a multiplicity of sensors that are placed on the periphery of the process cross-section that is under interrogation, or from sensor pairs around the cross-section that are rotated or switched relative to the process vessel or pipe. Information on the flow regime, vector velocity, and concentration distribution in process vessels and pipelines will be determined from the images.

In Figure 1.1 different tomographic techniques are displayed. In Figure 1.1a different ways of tomographic measuring techniques are shown. One can rotate the object with respect to a source and detecting sensor (left figure), use one source together with several detection sensors (middle figure), or use a system with multiple sensors and detectors (right figure). The source can be any radiation source, such as X-ray or  $\gamma$ -ray sources, optical sources, acoustic sources, or an electrical source. A well known optical method is Particle Image Velocimetry (PIV), which is widely used to image flow fields in stirred vessels.

In Figure 1.1b three different electrical tomography techniques are shown: The electrical

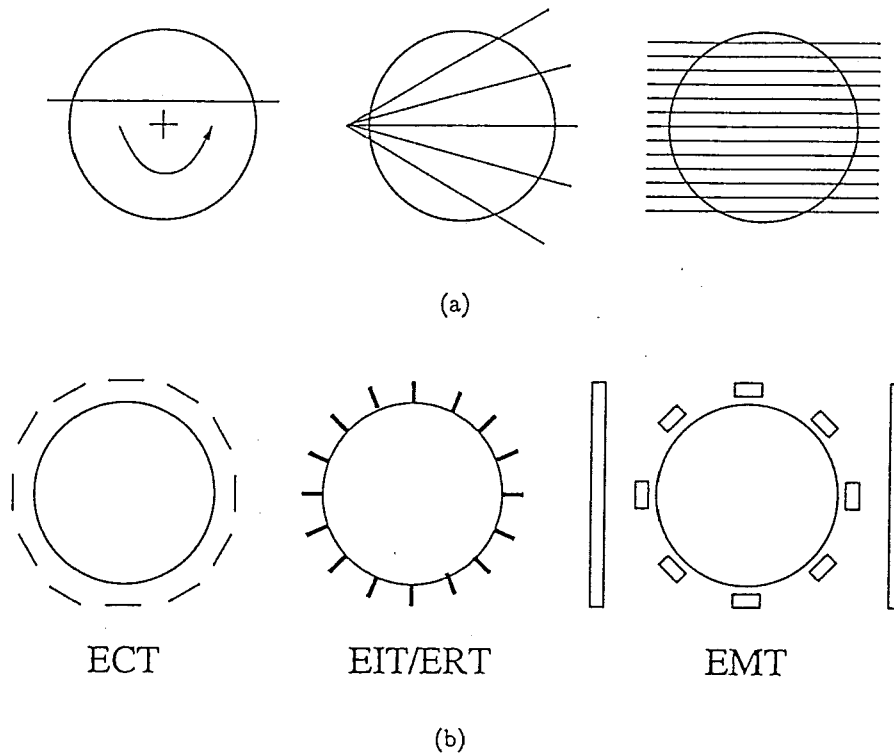


Figure 1.1: Different tomographic techniques.

capacitance tomography, the electrical inductance/resistance tomography and the electrical magnetic tomography.

The three different electrical tomography methods have their own application. ECT is used for both imaging flows consisting of two electrically isolating components and flame imaging, ERT/EIT for flows having one electrically conductive continuous phase and EMT for measuring the permeability distribution of two conductive components.

*Process Tomography* is a relative new research field compared to *Medical Tomography*. The objective of process tomography is to image process parameters in time and space. In pipe flow imaging this means to image the flowing medium over the cross-section as a function of time and position along the pipe. Compared to medical tomography, for which the patient often is placed inside some tomography system for a given time period, a process tomography system has to be adapted to the process of interest. For a pipe flow imaging system this implies that the system has to be mounted around the pipe, and be able to operate at a speed determined by how fast the medium changes.

Spatial resolution using electro-magnetic radiation can be as good as good as 1%, but these methods have a limited range of applications due to, for example, optical opacity when using light, slow speed and radiation containment when using ionising radiation, expense when using magnetic resonance, need for operator invention and radio-active particles when using positron emission tomography. Electrical tomography sensors offer a modest spatial resolution, but they are very fast, inexpensive and suitable for a wide range of vessel sizes.

At the Kramers Laboratorium voor Fysische Technologie, research is done towards the

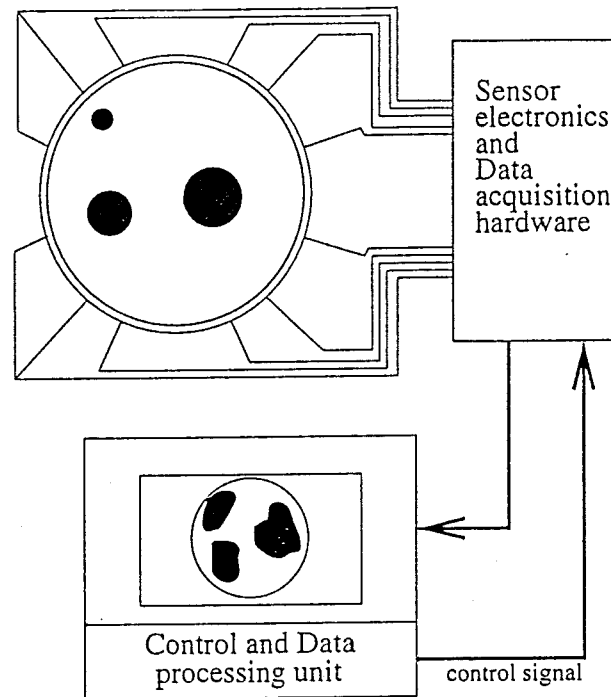


Figure 1.2: A capacitance based pipe flow imaging system. Electrodes are mounted circumferentially around the pipe. The measurements and data acquisition are done by the sensor electronics and the data acquisition unit. The data are sent to the control and data processing unit for reconstruction and image presentation.

dynamics of *fluidised bed* reactors and transport phenomena of pipe lines. In this research it is investigated if the ECT system is a valuable measuring technique for distinguishing between two non-conducting phases in a cross-section of a pipe.

## 1.2 Electrical capacitance tomography

The fluidised bed tomography system consists of three parts: The sensor, the sensor electronics and a computer network (Figure 1.2). The most commonly used reconstruction algorithm for a capacitance based process tomography system is the *linear back projection algorithm* (LBP), originally developed for medical tomography-systems. The LBP-algorithm is very fast, but not very accurate due to smoothing effects. In medical tomography application, hard field sensor systems, i.e. sensor system for which the field distribution is independent of the medium between the source and the detector, are most frequently used. A typical example is the CAT-scanner which utilises X-rays. For such sensor systems several reconstruction algorithms superior to the original LBP-algorithm have been developed. In process tomography application, however, soft field sensor system are most common, and thus the improved reconstruction algorithms are no longer valid. Hence an important activity within process tomography is to develop specialised reconstruction algorithms, which are capable of reconstructing the object of interest at an acceptable accuracy.

### 1.3 Aim of this project

Knowledge of unsteady solid concentration is vital to characterise the dynamic behaviour of a fluidised bed. The flow pattern of the fluidised bed is determined by particle-particle, particle-gas interaction and bubble coalescence. These interactions, in a time domain can therefore be characterised by both large and small scale fluctuations. The rapid fluctuations of the voidage in the bed, normally negate the possibility of using radiation based tomography sensors, but such phenomena can be sensed using electrical methods.

At the *Chemical department* of the Delft University of Technology research is done towards the behaviour of fluidised beds by doing pressure measurements. These pressure measurements, however, are not sufficient for measuring bubble size distributions.

Therefore experiments and simulations have been performed in this research to test a new set of least squares based reconstruction algorithms, developed at the Delft University of Technology, and investigate their sensitivity to noise. Furthermore, the smallest object to be detected by the ECT system was determined.

### 1.4 Structure of this report

In Chapter 2 the basic principles of the Electrical Capacitance Tomography problem are described. Chapter 3 deals with simulations, performed to test novel sensor concepts and to define the amount of information provided by the data.

In chapter 4 the new developed reconstruction algorithms are described. Chapter 5 gives the results from noise measurements using the ECT sensor electronics. Subsequently Chapter 6 deals with the influence of the noise measured on the reconstruction algorithms described in chapter 3. This influence was investigated by adding simulated noise to exact data from simulations. In Chapter 7 the reconstruction algorithms are tested using real data. In Chapter 8 the sensitivity of the ECT system is investigated. Finally, in Chapter 9 the conclusions and recommendations are given.

## Chapter 2

# The electrical capacitance tomography problem

### 2.1 Introduction

This chapter describes the tomographic technique and the theory of the electrical capacitance tomography system. First a description of the electrical capacitance sensor is given and second the theory on which the technique relies.

The measuring technique uses the measurements of electrical capacitances in different locations and directions of the cross-section of a three-dimensional object of non conductive components. These measurement data can be used to reconstruct the dielectric or permittivity distribution over the cross-section which is under investigation.

### 2.2 Capacitance sensor

Figure 2.1 displays a cross-section of a 12-electrode capacitance sensor. The sensor is set up by mounting a number of electrodes, in this case 12, around the periphery of the duct to be imaged. To perform a 'body scan' of the cross-section, the capacitances between all electrode pair combinations should be measured. The technique relies on changes in capacitance values between electrodes owing to the change in permittivities of flow components.

An earthed outer screen is used to shield the electrode system from stray fields. The empty space between this screen and the pipe wall outer surface is filled with air, which insulates the electrodes from the shield.

Figure 2.2 shows a side-view of the capacitance sensor. For the field lines to be as parallel as possible to the sensor plane, the axial shield is cut into segments. These axial shields are as large in circumferential direction as the measuring electrodes. Applying the same potential to the axial shield electrodes above and under the measuring electrode as to the measuring electrode itself, reduces the so-called 2D/3D-error. Since we want to reconstruct the distribution of components in the cross-section only, the electrostatic field must be aligned in one plane. These axial shield electrodes avoid the field lines from

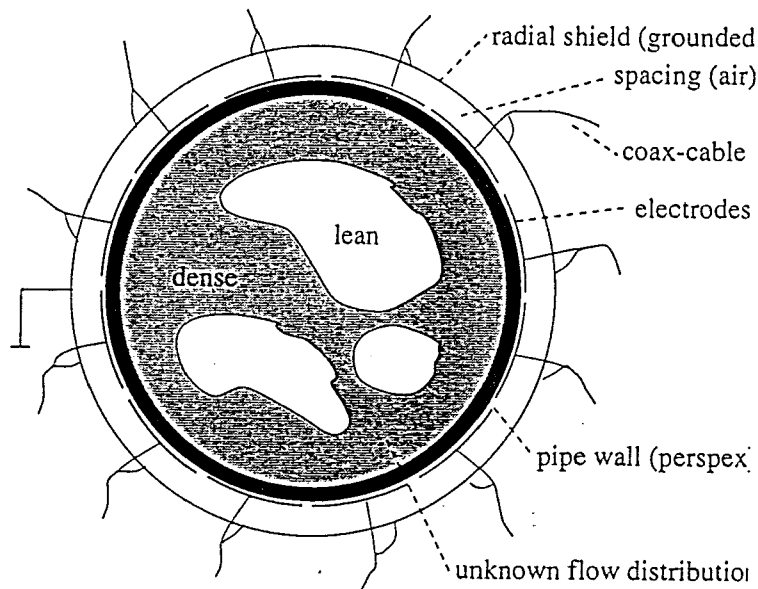


Figure 2.1: Cross-section of the ECT system.

bending in axial direction, yielding a better approach to the assumption of dealing with a two-dimensional electrostatic field [Kühn et al., 1996]. This sensor type is often referred to as the *METC-type sensor*, since this sensor type had first been used by the Morgantown Energy Technology Center (METC), USA [Halow and Fasching, 1993].

## 2.3 The forward problem and the inverse problem

### 2.3.1 Forward problem

The electrical capacitance tomography problem can be subdivided into two problems. On the one hand we have the problem of calculating the capacitance values for a given permittivity distribution. This can be accomplished using a numerical method, like a *Finite Element Method*. On the other hand there is the problem of estimating the permittivity distribution inside the cross-section using the measured capacitances, i.e. obtaining a dielectric distribution  $\epsilon(x, y)$  which theoretically yields capacitance values equal to the measured ones. The former is referred to as the *forward problem*, the latter as the *inverse problem* [Xie et al., 1992].

Excitation sources (voltage or current) for use with electrical capacitance tomography systems are generally of low frequency. Therefore electrical capacitance imaging systems are described by equations governing the electrostatic field. These partial differential equations for electrostatic fields are special cases of the generalised inhomogeneous Helmholtz equation [Silvester and Ferrari, 1990]:

$$\nabla \cdot [m(\mathbf{r})\nabla u(\mathbf{r})] + k^2 u(\mathbf{r}) = f(\mathbf{r}) \quad (2.1)$$

where  $u(\mathbf{r})$  is a scalar variable which is the system unknown.  $m(\mathbf{r})$  represents the property of the medium,  $f(\mathbf{r})$  is a given driving function, and  $k$  is a position-invariant constant.

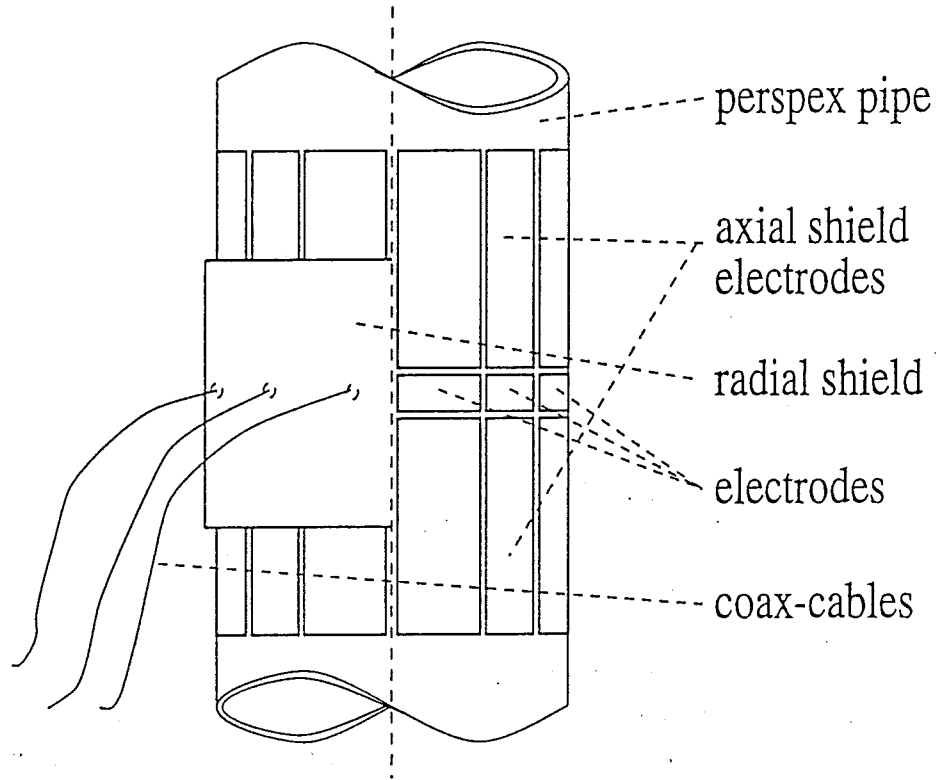


Figure 2.2: the ECT sensor.

In the *forward problem* the electric field is assumed to be *static* and *2-dimensional*. Under these assumptions, the electric field in the electrode system shown in Figure 2.1 is governed by *Poisson's* equation:

$$\nabla \cdot \mathbf{E} = \frac{\rho}{\epsilon_0} \quad (2.2)$$

where  $\mathbf{E}$  is the *electric field strength*,  $\rho$  the *total charge density* and  $\epsilon_0$  the permittivity of free space.

By definition, the *electric flux density*,  $\mathbf{D}$ , is

$$\mathbf{D} = \epsilon_0 \mathbf{E} + \mathbf{P} = \epsilon \mathbf{E} \quad (2.3)$$

where  $\mathbf{E}$  is the *electric field strength*,  $\epsilon$  the permittivity of free space,  $\epsilon_0$  multiplied by the relative permittivity,  $\epsilon_r$ , and  $\mathbf{P}$  the *electric polarisation*. The right hand side of equation 2.3 is only valid for dielectrics which are *linear* and *isotropic*.

The Poisson equation can also be written as follows:

$$\nabla \cdot \mathbf{D} = \rho_f \quad (2.4)$$

where  $\rho_f$  is the free charge density. In the ECT system the two phases are non conducting, so the free charge density,  $\rho_f$ , is zero. Since  $\mathbf{E} = -\nabla\phi$  where  $\phi$  is the *potential*, it follows that Equation 2.2 can be written as follows:

$$\nabla \cdot \mathbf{D} = \nabla \cdot \epsilon \mathbf{E} = \nabla \cdot (\epsilon \nabla \phi) = 0 \quad (2.5)$$

The 2-dimensional forward problem involves the calculation of the capacitance values for a given dielectric distribution  $\epsilon(x,y)$ . For this 2-dimensional case Equation 2.5 can be rewritten as:

$$\nabla \cdot (\epsilon(x,y)\nabla\phi(x,y)) = 0 \quad (2.6)$$

better known as *Gauß's law*. Here  $\phi(x,y)$  is the potential distribution over the cross-section. This Laplace-like *partial differential equation* (PDE) can be solved numerically using a *finite element method* software package [Lorrain et al., 1987].

To solve Equation 2.6 the Dirichlet boundary conditions are applied. The Dirichlet boundary conditions say that parts of the boundary are applied with a constant potential.

$$\Psi^i = \begin{cases} V & (x,y) \subseteq \Gamma_i \\ 0 & (x,y) \subseteq \text{all } \Gamma_k \quad (k \neq i) \quad \& \quad (x,y) \subseteq \Gamma_s \end{cases} \quad (2.7)$$

Here  $\Gamma_i$  refers to the surface of electrode  $i$  and  $\Gamma_s$  to the outer shield surface. In the sensor shown in Figure 2.1, the electrodes and the outer shield are set to a constant potential.

To obtain a total 'body scan' the capacitances between all electrode pair combinations have to be measured. Applying one electrode, the *source electrode*, with a signal and setting all other electrodes, the *detecting electrodes*, to earth, all capacitances between the source electrode and detecting electrodes can be measured. Then the adjacent electrode can be set to be the source electrode and all capacitances between the new source electrode and the detecting electrodes can be measured. Setting every electrode subsequently to the be source electrode results in all capacitances between all possible electrode combinations. The governing Equation 2.6 results in a charge distribution over all detecting electrodes. The capacitance between two electrodes,  $i$  and  $j$ ,

$$C_{ij} = \frac{Q}{V} \quad (2.8)$$

is determined by the total charge  $Q$  distributed over the detecting electrode divided by the potential difference between the source electrode and this detecting electrode. The solution of the piecewise analytic solution to Equation 2.6, is unique [Kohn and Vogelius, 1985].

If the permittivity distribution  $\epsilon(x,y)$  is fixed, the electric field  $-\nabla\phi(x,y)$  changes linearly with the potentials applied to the boundaries. However, generally the flow distribution  $\epsilon(x,y)$  is irregular and therefore there is no general analytical solution to Equation 2.6. Thus a numerical method has to be used.

### 2.3.2 Inverse problem

The section above showed how the capacitance values are related to a given permittivity distribution  $\epsilon(x,y)$ . In the industrial applications of tomographic techniques, the measured data are used to reconstruct the flow parameters. Thus, the measured capacitances are used in to solve the inverse problem, i.e. determine the distribution  $\epsilon(x,y)$  within the cross-section from a limited number of measurements.

The relation between the measured capacitance of an electrode pair and the permittivity

distribution  $\epsilon(x, y)$  is given by:

$$C_{ij} = \frac{\epsilon_0 \cdot \int \epsilon_r \nabla \phi \cdot \mathbf{n} \, dl_j}{V_{ij}} \quad (2.9)$$

Here,  $V_{ij}$  is the potential difference between electrode  $i$ , the source electrode, and electrode  $j$ , the detecting electrode.  $l_j$  is the line of electrode  $j$  in the 2-D model. The charge on electrode  $j$  is determined by the electric flux density  $\mathbf{D}$  through detecting electrode  $j$ , defined as:

$$\mathbf{D} = \epsilon \frac{\partial \phi}{\partial n} \mathbf{n} \quad (2.10)$$

Here  $\mathbf{n}$  is the outward pointing normal vector. The relationship between the electric flux density,  $\mathbf{D}$ , and the charge  $Q_j$  on detecting electrode  $j$  is given by:

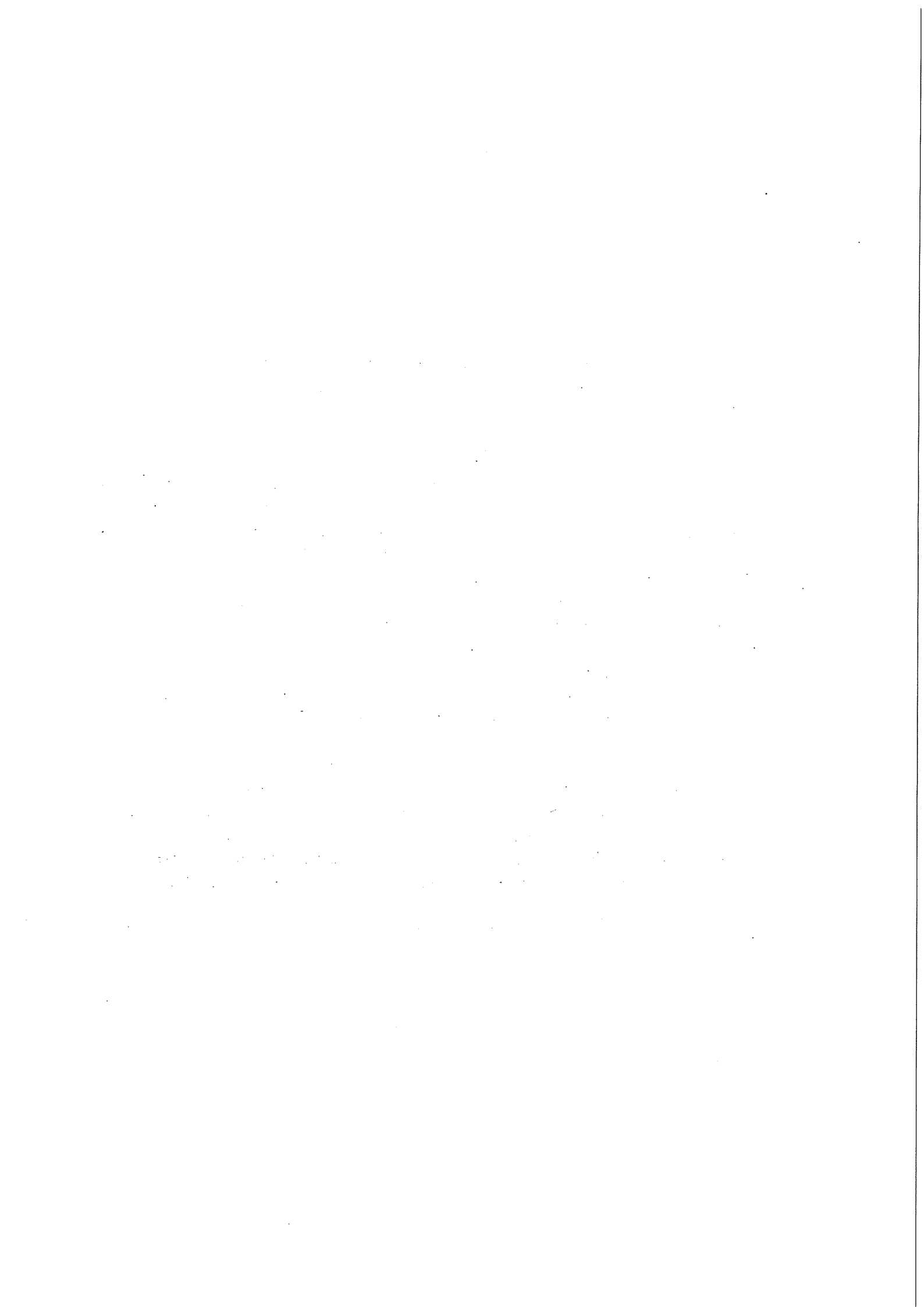
$$Q_j = \oint_{l_j} \epsilon \frac{\partial \phi}{\partial n} \cdot \mathbf{n} \, dl_j \quad (2.11)$$

where  $dl_j$  is the closed line over the outer surface of electrode  $j$ . Hence, the integral in the numerator of Equation 2.9 is in fact the total charge distributed on detecting electrode  $j$ . The *inverse ECT problem* is in fact a parameter estimation problem, in which the model parameters have to be determined for a given set of input and output parameters.

The electric flux lines, expressed by the electric field vector  $\epsilon(x, y) \nabla \phi(x, y)$ , are related to the object  $\epsilon(x, y)$  to be reconstructed. This is distinctly different from other tomography techniques, such as X-ray tomography. In the latter technique the exact position, where the data are taken, is known, and therefore the data are directly related to some position in the object to be measured.

For electrostatic fields the electric flux lines will deflect when they encounter an interface of different permittivities. This introduces the so-called 'soft field effect', which inherently introduces problems in the reconstructions, since the electric flux lines change when the permittivity distribution changes. This explains the poor image resolution of the electrical capacitance tomography compared to the X-ray tomography [Williams and Beck, 1995]. Up till now the *linear back projection* (LBP) algorithm is the most commonly used algorithm to solve the capacitance inverse problem [Xie et al., 1992]. This algorithm uses a larger number of unknowns, i.e. image pixels, than the number of capacitance measurements. This makes the system highly under-determined (see section 3.3.2). 'A *priori*' knowledge can be used to alleviate the problem and decrease the degree of under-determinacy. The LBP is merely a linear approach to the non-linear reconstruction problem and does not correct for the soft field effect, resulting in rather qualitative than quantitative algorithm.

At the Delft University of Technology (DUT), new reconstruction algorithms were developed, based on *least squares* methods (chapter 4). These algorithms has been tested for their robustness, i.e. what is the influence of noise towards the reconstruction (chapter 6), and have been used to reconstruct real data (chapter 7).



# Chapter 3

## Simulations

### 3.1 Introduction

This chapter presents the problem of calculating capacitances for a given  $\epsilon(x, y)$  of a circular pipe, the so-called forward problem. The solution to the forward problem is defined as the process of predicting measurement data for a given system model. With a *Finite Element Method (FEM)* software package, the capacitances between all electrode pairs of the sensor can be calculated for a given permittivity distribution  $\epsilon(x, y)$  in the cross-section of the pipe (see Figure 3.1). The data, calculated by the forward model, are used to perform a *Principal components analysis (PCA)* (this Chapter) and, secondly, to test the inverse algorithms for the electrical capacitance tomography problem (Chapter 7 and Chapter 6).

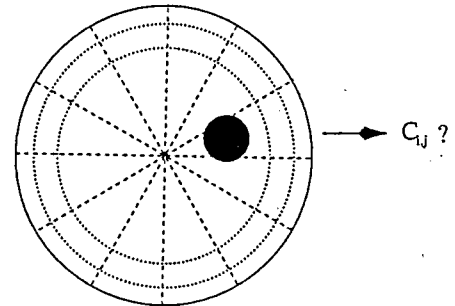


Figure 3.1: How to calculate the capacitance values for a given distribution  $\epsilon(x, y)$

### 3.2 Implementation of the ECT problem in SEPRAN

#### 3.2.1 The forward problem

The ECT problem can be subdivided into two integrated problems. The so-called *forward problem* and the *inverse problem* (See section 2.3). In the forward problem the capacitance values for a given permittivity distribution,  $\epsilon(x, y)$ , are calculated. If the permittivity distribution,  $\epsilon$ , is a constant with respect to space the PDE 2.6 reduces to the Laplace equation and an analytical solution can be found. For simple rotational symmetric permittivity distributions it is also possible to find an analytical solution for Equation 2.6. Since the permittivity distribution in the ECT problem is not constant within the boundaries and is in general not symmetric, the forward problem is preferable to be solved numerically. It can be proved that for any permittivity distribution,  $\epsilon(x, y)$ , the forward problem has a unique solution. Nowadays, the finite-element method is the most widely used numerical method to solve partial differential equations, like Poisson's equation.

In general, the following three stages are involved in sensor modelling [Williams and Beck, 1995]:

1. The mathematical model of the sensor must be identified, and the governing equations and related boundary conditions determined.
2. The geometric model of the sensor must be established.
3. An efficient numerical method (discretisation scheme) must be chosen in order to realise a computer solution of the problem.

### 3.2.2 General mathematical formulation of the sensor model

In this paragraph, the two-dimensional *finite element* model of the ECT system is described. Figure 2.2 shows a 12 electrode capacitance sensor. For one complete tomogram, first the capacitances between electrode one and electrodes two to twelve are measured, giving eleven measurements. Electrode one is set to be the source electrode and electrodes two to twelve are set to be the detecting electrodes, which are at virtual earth potential. Subsequently, electrode two is set to be the source electrode and electrodes three to twelve are set to be the detecting electrodes, giving ten parallel measurements. Finally electrode eleven is set to be the source electrode and electrode twelve set to be the detecting electrode. The capacitance  $C_{ij}$  is equal to the capacitance  $C_{ji}$  [Grootveld, 1996], and therefore there is no need to measure the capacitance  $C_{ji}$ .

So for one complete tomogram, a total of 66 measurements are produced. In general, the number of measurements,  $M$ , for an  $N$ -electrode system is given by:

$$M = \frac{N(N-1)}{2} \quad (3.1)$$

In section 2.3 the governing equation for the electrical capacitance tomography system was derived. Using the assumption that the field is 2-dimensional and no free charges present this resulted in *Gauß's law*

$$\nabla \cdot (\epsilon(x,y)\nabla\phi(x,y)) = 0 \quad (3.2)$$

This equation has an analytical solution if the permittivity distribution is constant throughout the entire cross-section or if the permittivity distribution is rotational symmetric.

Therefore, the domain must be made discrete. Applying then the governing equations to the discrete domain, the discrete numerical solution can be calculated. The following section will briefly describe the steps towards the *Finite element method* model for the ECT forward problem.

### 3.2.3 Pipe geometry

The *3-dimensional* sensor in Figure 2.2 has to be modelled in a *2-dimensional* geometry. Figure 3.2 shows the definition of the geometry of the *2-dimensional* sensor model. The domain is subdivided into three *element groups*, the spacing between the outer shield and

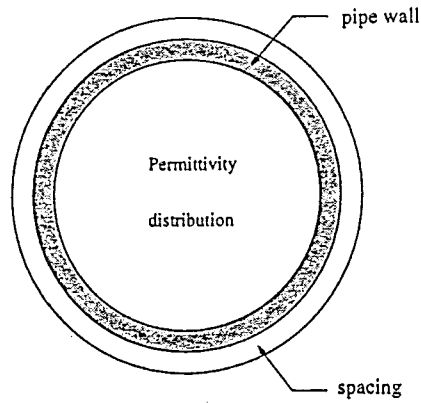


Figure 3.2: 2-dimensional geometry of the electrical capacitance tomography sensor.

the pipe wall, the pipe wall itself, and the inner section of the sensor where the (unknown) permittivity distribution is located. The electrodes now, can be defined as parts of the interface between the pipe wall and the air-spacing. As mentioned earlier, the geometry has to be defined in a FEM package (in this case the package SEPRAN [Segal, 1993] is used). Because of the rotational symmetry of the sensor, the sensor can be subdivided into  $N$  identical pie-shaped segments, where  $N$  is the number of electrodes. The discrete pie-geometry is then created by defining the curves as shown in Figure 3.3. First the different nodes of one pie segment are defined. Next the lines and curves are drawn to define one total pie shaped segment. Finally this pie shaped segment is rotated over  $\frac{2\pi}{N}$  till one complete cross-section has been established. The mesh is then obtained using the

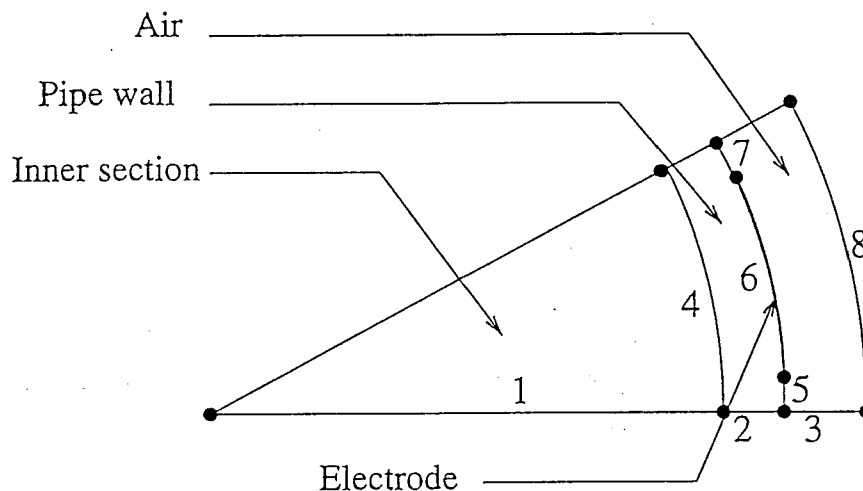


Figure 3.3: Pie shaped segment of the sensor geometry. Rotation of this segment results in the total sensor geometry. The numbers in the figure refer to the curve numbers.

SEPRAN mesh generator sepmesh. Appendix D contains an example of the mesh-input file used in the 16 electrode sensor simulations. Here the cross section is divided into a large large number of triangular elements. In these triangular elements the permittivity is assumed to be constant. In Table 3.1 the number of nodes and number of elements are given. Since there are very large gradients between the source electrode and its neighbouring detecting electrodes, see Figure 3.4, the mesh has to be refined in these regions to get more accurate results.

Table 3.1: Geometry parameters of the sensors used for the noise measurements

	Nodes and elements	
	nodes	elements
original mesh	3157	6132
1 <sup>st</sup> iteration	3682	7173
2 <sup>nd</sup> iteration	5341	10480
3 <sup>th</sup> iteration	8086	15954

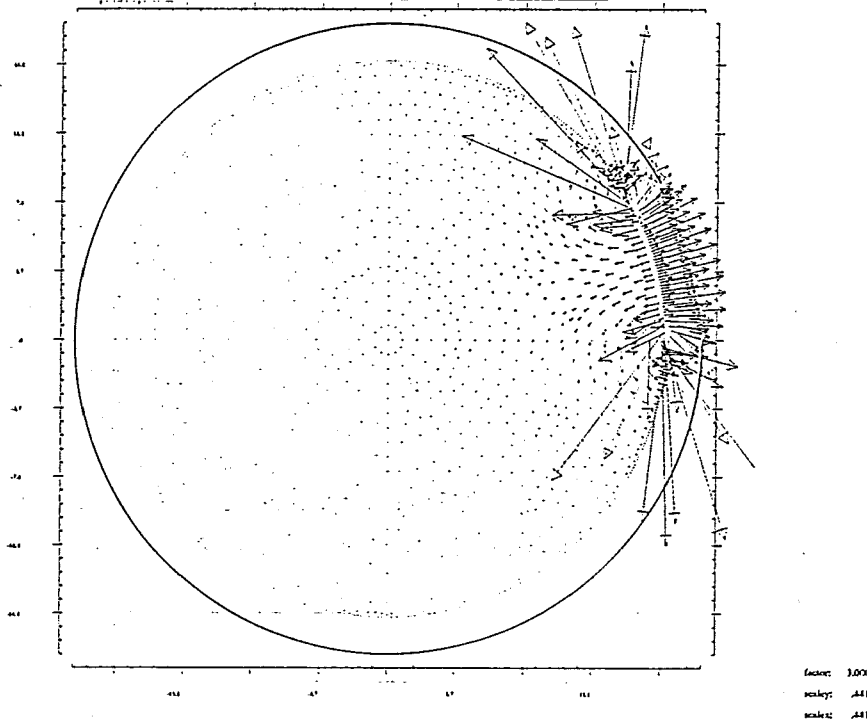


Figure 3.4: Plot of the potential gradient calculated by SEPRAN. To get accurate estimates of the capacitances of neighbouring electrodes, the mesh has to be refined there where the potential gradient is large.

The routine MESHADAPT has iteratively adapted the size distribution of the finite elements to the vector field of the potential gradient, yielding very small elements where the gradients are large (see Table 3.1).

### 3.2.4 Boundary values

The geometry is made of identical pie-shaped segments. One pie shaped segment consists of eleven curves, which are shown in Figure 3.3. The *Dirichlet boundary conditions*, as explained in section 2.3 apply on curves 6 and 8, the 'electrode' curve and the 'outer shield' curve.

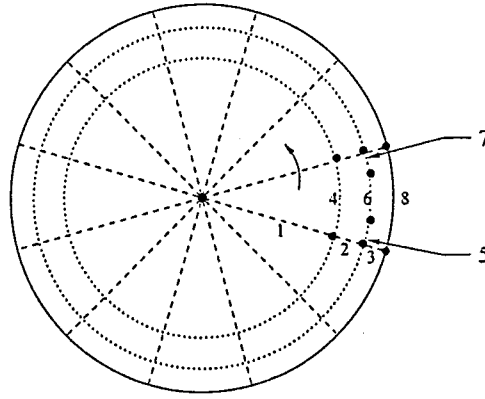


Figure 3.5: The pipe geometry of the 2-dimensional capacitance sensor, when the pie-shaped segment is rotated  $N$  times over  $\frac{2\pi}{N}$ .

### 3.2.5 Discrete numerical solution of the forward problem using SEPRAN

In the simulations using the FEM package SEPRAN, one electrode, the source electrode represented by curve 6 in Figure 3.5, is set to 1 Volt. Then Equation 2.6 is solved numerically with a dielectric distribution as input. SEPRAN calculates first the potential in every nodal point of the generated mesh for this given permittivity distribution. Secondly the gradient of the potential is calculated by means of finite differences between the nodal points. To calculate the capacitance value, SEPRAN integrates over the 'electrode' curves of all detecting electrodes separately returning the total amount of charge on every electrode as output.

Then the capacitance value of the electrodes follows from:

$$C_{ij} = \frac{Q_j}{V_{ij}} = \frac{\epsilon_0 \cdot \int \epsilon \nabla \phi \cdot \mathbf{n} \, dl_j}{V_{ij}} \quad (3.3)$$

Here  $V_{ij}$  is the potential difference between electrode  $i$ , the source electrode, and electrode  $j$ , the detecting electrode,  $Q_j$  the total charge distributed on detecting electrode  $j$ , and  $l_j$  the line of detecting electrode  $j$  in the 2-dimensional sensor model. SEPRAN returns only the amount of charge on detecting electrode  $j$ . Multiplying this value with the  $\epsilon_0$  and the axial electrode length,  $l_{ax}$ , and dividing it by the potential difference,  $V_{ij}$ , gives the capacitance value for a sensor with axial electrode length  $l_{ax}$ . Note that in this model the 3-D effect, see section 2.2, is neglected.

Figure 3.6 illustrates this line integration along both sides of the detecting electrode. The small arrows represent the electric field lines, approximated by finite differences in the *finite element model*. In SEPRAN this potential gradient at a position next to the electrode is multiplied with the permittivity value found at that position. The sum of these values on both sides of the electrode results in an estimate of the total electric flux which arrives on the detecting electrode. From this total flux the total charge on the detecting electrode can be calculated using Equation 2.11.

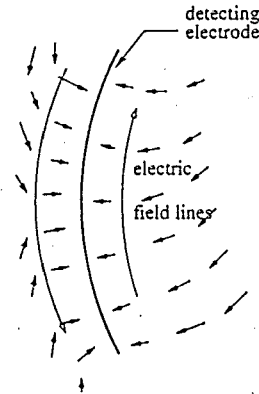


Figure 3.6: The line integration over the 'detecting' electrode, resulting in the total charge found on the detecting electrode

### 3.3 Principal components analysis

#### 3.3.1 Introduction

Within the problem of reconstructing an image of the permittivity distribution, i.e. solving the inverse problem, we have to divide the cross-section of the pipe into an appropriate number of picture elements, the reconstruction pixels. In these reconstruction pixels the assumption is made that the permittivity is constant. The number of reconstruction pixels should depend on the amount of information available per image, one tomogram.

#### 3.3.2 Over- and under-determinacy

If there are too few pixels defined in the cross-section, the problem is said to be *over-determined*. In this case the variations in the data can not be explained by the limited number of model-parameters. This means that the amount of information which is offered by the capacitance measurements, is not completely used to reconstruct the permittivity distribution. So we have to define more pixels in the cross-section.

If, on the other hand, we define too many pixels in the cross-section, permittivity changes in neighbouring pixels will show nearly no variations in the capacitance data. This will make the problem singular, which means that there is no unique solution anymore. This is the case of *under-determinacy*. Under-determined problems typically have more unknowns than data, although it is possible to have problems that are to some degree under-determined even when the problem has more data than unknowns. This can be the case when the data kernel has a very poor structure. This is the case when there is a large set of data points, which only refer to one over determined sub-area of the domain. The rest of the domain is, thus, undetermined, resulting in a poor structure of the data kernel.

The ECT problem is, like most inverse problems that arise in practice, not completely over-determined nor completely under-determined. This is referred to as *mixed-determined* problems. To define the right number of pixels, a reconstruction pixel arrangement has to be found which results in an optimal situation between over- and under-determinacy.

#### 3.3.3 Singular value decomposition

A possible way to search for this optimum is a *principal components analysis* (PCA) [Jackson, 1991]. Note that this is, however, only an approximation towards the problem of over- and under-determinacy. This technique investigates the degree of correlation in the data. If two data-points are not correlated, they are independent and therefore two model parameters can be defined. If, on the contrary, they are correlated, there is a dependency between the data-points. This dependency between the data-points will reduce the actual amount of information available. The PCA shows the number of uncorrelated variables to which the data can be reduced.

The technique is based on the reduction of a  $p \times p$  symmetric, nonsingular matrix  $V$  to a diagonal matrix  $L$ . Premultiplying and post-multiplying this matrix  $V$  by an orthogonal matrix  $U$  yields:

$$\mathbf{U}^T \mathbf{V} \mathbf{U} = \begin{pmatrix} \mathbf{L} & 0 \\ 0 & 0 \end{pmatrix} \quad (3.4)$$

where  $\mathbf{L} = \text{diag}(\sigma_1, \sigma_2, \dots, \sigma_r)$ ,  $\sigma_1 \geq \sigma_2 \geq \dots \geq \sigma_r > 0$ , and  $\mathbf{U} = [\mathbf{u}_1 | \mathbf{u}_2 | \dots | \mathbf{u}_p]$ .

In fact this is a *singular value decomposition* (SVD) [Stewart, 1973]. With this decomposition one can define the rank of the matrix  $\mathbf{V}$ . The rank is in this case of less than full rank, because of the zeros in the diagonal matrix on the right-hand side of equation 3.4. In theory, it is no problem to define the rank of a matrix. Application of an algorithm, such as Gaussian elimination, to the matrix will show the rank of the final reduced form. In practice the situation is more complicated. A SVD might be a solution.

This decomposition is basically unique. Thus the numbers  $\sigma_1, \sigma_2, \dots, \sigma_r$  must be the nonzero eigenvalues of matrix  $\mathbf{V}$ , arranged in descending order. The columns of  $\mathbf{U}$  are the eigenvectors of  $\mathbf{V}$ .

What in fact happens is an axis transformation of the elements in matrix  $\mathbf{V}$  to an orthonormal basis. The elements of  $\mathbf{V}$  are then projected on these new axes, the *eigenvectors*  $\mathbf{u}_i$ . The *principal components analysis* relies on the reduction of the data covariance matrix. For a  $p$ -variable problem the covariance matrix  $\mathbf{S}$  is defined as,

$$\mathbf{S} = \begin{pmatrix} s_1^2 & s_{12} & \cdots & s_{1p} \\ s_{12} & s_2^2 & \cdots & s_{2p} \\ \vdots & \vdots & & \vdots \\ s_{1p} & s_{2p} & \cdots & s_p^2 \end{pmatrix} \quad (3.5)$$

where  $s_i^2$  is the variance of  $\mathbf{x}_i$ , the vector containing the measurements of the  $i$ th variable, and  $s_{ij}$  represents the covariance between the  $i$ th and  $j$ th variable. When the covariance between two variables is not equal to zero, it indicates there is some relationship between these two variables. The strength of the relationship is quantified by the correlation coefficient  $r_{ij} = \frac{s_{ij}}{s_i s_j}$ .

Applying the principal axis transformation to the data covariance matrix  $\mathbf{S}$  will transform the  $N$  correlated variables  $\mathbf{x}$  into  $N$  new uncorrelated variables  $\mathbf{z}$ . The coordinate axis of these new variables are described by the *eigenvectors*  $\mathbf{u}_i$ , which make up the matrix  $\mathbf{U}$  used in the transformation. The principal components have zero mean and variance  $\sigma_i$ , the  $i^{\text{th}}$  *eigenvalue* [Jackson, 1991].

To define the number of principal components, i.e. reducing the number of variables without losing significant information, a graphical technique, the SCREE test, is used. Plotting the eigenvalues  $\sigma_1, \sigma_2, \dots, \sigma_r$  of Equation 3.4 against their number yields a declining curve, which exhibits the variance explained by the principal components. When the data are uncorrelated, the information is merely equally distributed among the orthonormal directions and will show a curve with a slight declination. On the contrary, correlated data yield a curve which falls down rapidly to zero, because the number of principal components carrying information is considerably smaller than the number of variables. So, there is a cut off between important roots, which exhibit much variance, and non-important roots, which exhibit nearly no variance. The more the data are correlated, the smaller the number of principal components carrying information. In the diagram the curve will decline more rapidly towards zero. In Figure 3.7 two different PCA plots are shown for

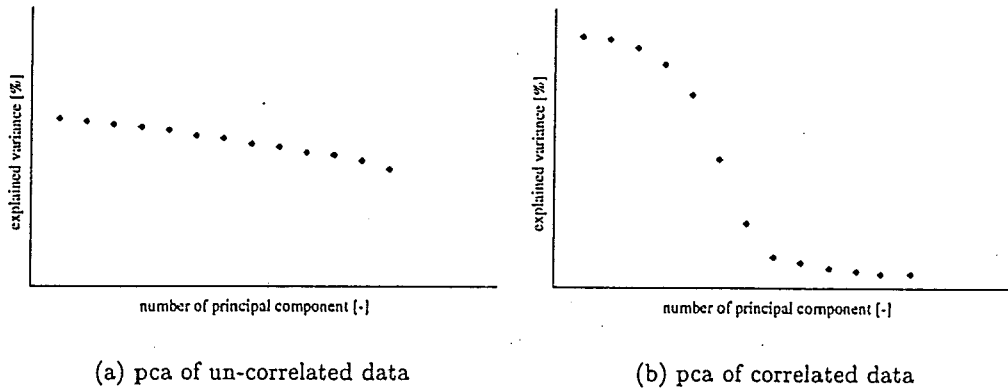


Figure 3.7: PCA plots of non correlated data (a) and correlated data (b)

two degrees of correlation; non or slight correlated data and correlated data.

### 3.3.4 SCREE test

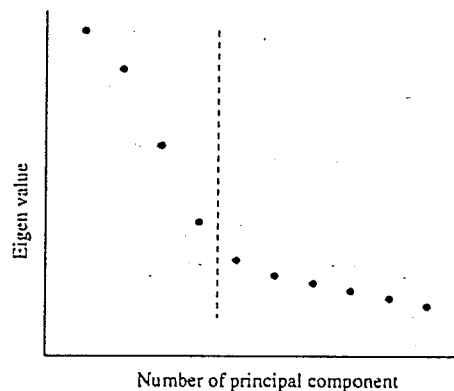


Figure 3.8: Example of the SCREE test, which is a graphical technique to define the number of retained PC's when performing a principal components analysis

To define now the number of reconstruction-pixels, the number of *principal components* (PC) with a significant variance is retained. Determine more pixels than retained PC's will make the problem close to singular, since the eigenvalues become close to zero for the rejected PC's.

The SCREE test is a graphical technique to define the number of retained PC's. Figure 3.8 shows a typical plot of correlated PC's. Most of the PC plots show this behaviour. The PC's fall off till some point, often called the *elbow*. The SCREE test then divides all the PC's into two groups, shown by the dashed line in Figure 3.8. Subsequently all of the PC's in the first group, on the left-hand side of the dashed line, are retained plus one of the latter group on the left-hand side of the dashed line. In Figure 3.8 the number of retained PC's according to the SCREE-test is five. The SCREE test, thus, recommends to estimate no more than five model parameters, since estimating more than five PC's makes the inverse problem under-determined.

### 3.3.5 Pixel shape

When the number of reconstruction pixels is defined, another problem arises: what sort of pixels to use? The most common pixel shapes are:

- **Polar shaped pixels.** When an electrode sensor round a pipe is used, it is easy to use polar pixels, while the cross-section of the pipe can be divided into pie-shaped segments, each assigned to one electrode. These pie-shaped segments can be subdivided into more pixels by defining one or more concentric rings in the cross-section.
- **Square shaped pixels.** This is the commonly used type of pixel. This is why most graphical routines are developed for a grid of square pixels. *Xie et al.* placed a lattice, i.e. a square which was divided into  $32 \times 32$  equally sized square pixels, over the cross-section of the unknown permittivity. As a consequence that at the rim of the cross-section the pixels were only partially covered.

We decided on using polar pixels since these match the circular imaging domain better than square pixels.

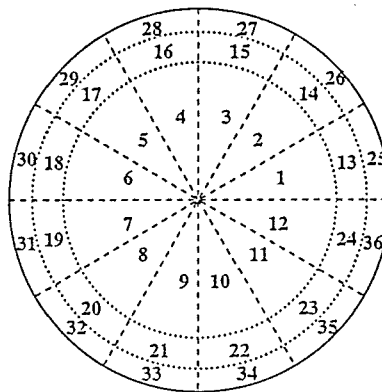


Figure 3.9: Polar pixel distribution in the cross-section of the capacitance sensor.

#### Radial size distribution of the pixels

F.T. Kühn [Kühn and van Halderen, 1997] showed that the sensitivity distribution varies over the cross-section, i.e. the sensitivity in the centre of the cross-section is significantly smaller than the sensitivity near the wall. This introduces underdeterminacy of the centre-pixels and overdeterminacy of the wall-pixels, since permittivity changes in pipe-centre pixels will only slightly influence the data in comparison with the near-wall pixels.

It was proposed to reduce the underdeterminacy of the centre-pixels by adapting the pixel surface area to the radial image resolution. Thus, making the centre-pixel larger in comparison with the near-wall pixels.

To adjust the radial size distribution of the polar pixels, Equation 3.6 was used.

$$j = 1 + \text{int}\left(p \cdot \left(\frac{r}{r_{\max}}\right)^n\right) \quad (3.6)$$

Where  $n$  is the pixel size exponent,  $r_{max}$  the inner pipe radius and  $p$  the number of rings, in this case there are evidently 3 rings. The formula assigns a cross-sectional point at radial position  $r$  in the forward mesh to the  $j^{th}$  ring of the inverse mesh.  $int()$  is the integer operation which returns the round-off figure of its argument.

The problem's mixed determinacy causes errors in the data vector to be amplified into the model parameters, i.e. the permittivity values to be calculated. The degree of this amplification is usually quantified by the *condition number* of the Hessian matrix, which contains the systems second derivatives (see also Section 4.3.3). This Hessian matrix can be approximated by multiplying the transpose of the Jacobian matrix with itself. A singular value decomposition of the Hessian matrix yields its eigen values, of which the decay is measured by the condition number, defined as the ratio of the highest eigen-value and the smallest eigen-value.

F.T. Kühn computed this condition number for the polar pixel arrangement shown in Figure 3.9 for the pixel size exponent,  $n$ , ranging from 1.6 to 4.2. In Figure 3.10 the condition number of the Hessian matrix is plotted as a function of the size exponent  $n$ . From this figure can be seen that the condition number decreases when the size exponent increases. As a compromise between the mixed determinacy and a too small near-wall

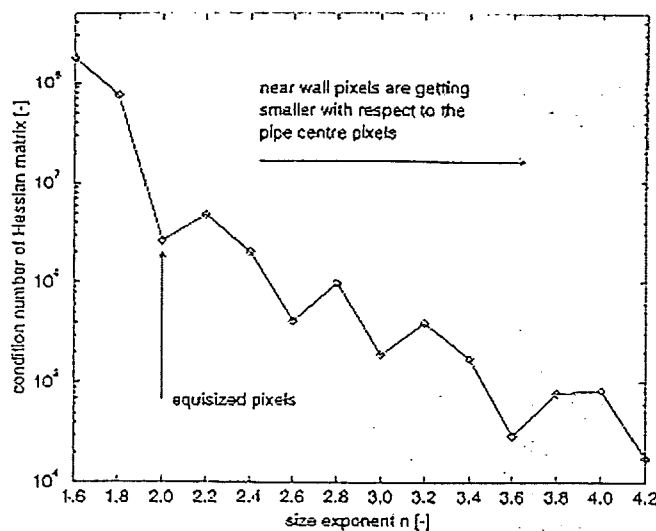


Figure 3.10: Condition number of the Hessian matrix as a function of the pixel size exponent  $n$ .

ring, a size exponent  $n = 3.4$  was chosen, resulting in the pixel distribution shown in Figure 3.9.

## 3.4 Simulations using SEPRAN

### 3.4.1 Simulation of the 12 electrode system

The first simulations were done by F.T. Kühn [Kühn, 1997] for the 12 electrode system. A principal components analysis had been applied to both the correlated data and the uncorrelated data. The covariance matrix was calculated from the forward solution of

10.000 randomly picked permittivity distributions.

The results were verified with a new simulation of 5.000 randomly picked permittivity distributions and are shown in Figure 3.11. In this simulation one electrode is set to be the source electrode. It becomes clear that uncorrelated data (setting all non-diagonal elements of the covariance matrix equal to zero) show indeed a typical straight line and the simulated, correlated data fall off to zero rapidly, indicating that the information is distributed the most among the first PC's.

First the capacitance values for the 5.000 randomly picked permittivity distributions are calculated. Then from these 5.000 sets of capacitance values the covariance matrix is calculated and the singular value decomposition is performed on this covariance matrix. Because the ratio between the capacitance value of adjacent electrodes and that of opposite electrodes is about 100, the covariance matrix is scaled as follows:

$$C_{i,scaled} = \frac{C_i - C_{empty}}{C_{full} - C_{empty}}; \quad (3.7)$$

Here  $C_i$  is the calculated capacitance,  $C_{empty}$  the capacitance value when the cross-section is filled with air, i.e. permittivity 1 and  $C_{full}$  the capacitance value when the cross-section is filled with material, i.e. permittivity 2. Thereafter the diagonal matrix, containing the eigenvalues of the data covariance matrix, is normalised

$$\sigma_{i,normalised} = \frac{\sigma_i}{\sum \sigma_i} \cdot 100\% \quad (3.8)$$

since then not the absolute variances are plotted but the relative variances, indicated by the term 'explained variances'.

If the SCREE test is applied on Figure 3.11, i.e. try to locate the elbow of the curve, the number of principal components is about 25 to 30. So about 25 to 30 PC's contain nearly all information. From equation 3.1 follows that there are a total of 66 electrode pair combinations for the 12 electrode system, however only about 30 PC's contain information. So defining more pixels than there are information carrying principal components, will make the problem underdetermined, and consequently singular. This is a very similar result in comparison with the results found by Kühn [Kühn, 1997].

### 3.4.2 Upgrading to an 16 electrode system

After these results, the question was raised whether more electrodes would result in more information, i.e. if using a 16 electrode system would lead to a gain of information, while the spatial resolution of the capacitance tomography system depends on the number of sensor electrodes mounted around the process being imaged [Huang et al., 1992]. However the size of each electrode is reduced as the number of electrodes is increased. So the sensitivity of the capacitance measurements will be reduced, since the standing capacitance values will be lower for smaller electrodes.

To investigate this, a new simulation is carried out for the same two phases, permittivity 1 for the lean phase and permittivity 2 for the dense phase. The simulations are adapted to a 16 electrode mesh. The covariance matrix is then calculated from forward solutions to 5.000 randomly picked permittivity distributions. For the 16 electrode system, the

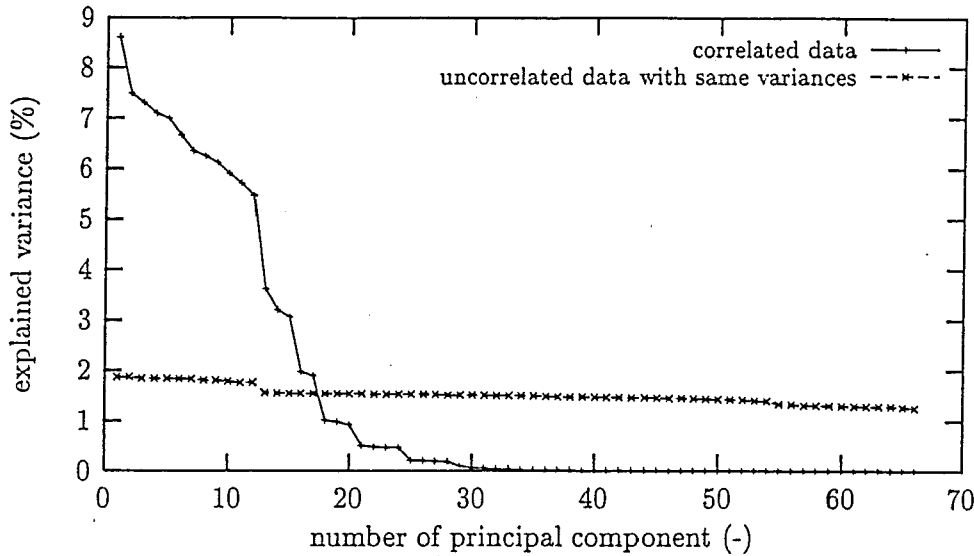


Figure 3.11: Principal components analysis of a 12 electrodes system with one source electrode.

number of different electrode combinations follows from 3.1, which results in 120 electrode combinations. Figure 3.12 shows the results of the PCA and the SCREE test for the 16 electrode configuration.

It is evident that an increase of the number of electrodes does result in more information containing principal components, but does not result in gain of information. When increasing the number of electrodes to 16 instead of 12, there are nearly twice as much data-points. However the increase in nonzero principal components is no more than ten. To understand these figures, it is useful to know what the *eigenvectors* look like. In Figures 3.13 and 3.14 the first four eigenvectors are displayed. These *eigenvectors* show the projection of the original coordinate axes on the new coordinate axes. On the x-axis the data number is plotted, on the y-axis the contribution of a data point to the eigenvector, which is under interrogation. From these figures can be seen that the first principal component (Figure 3.13a), above all, consists of diametrically opposing electrodes, and that there are almost no contributions from neighbouring electrodes. This means that the opposite electrodes have the largest relative explained variance and thus contain valuable information since these capacitance values vary most with the changes in the permittivity distribution.

Nevertheless, the signal of the opposite electrodes is very poor, because of the limits of the sensor electronics. The standing capacitance values for opposite electrodes are of the order of 8 fF ( $8 \cdot 10^{-15}$  Farad), which is near the limits of the electronics available today. Further, it has been demonstrated that the neighbouring detecting electrodes incorporate the strongest nonlinearities in the data (see Appendix C) and therefore are the most responsible for an iterative method not to converge when solving the *inverse problem* (See chapter 2.3).

This nonlinearity in the data is the result of the so called *soft field effect*: the electric flux lines in an electrostatic field will deflect, i.e. bend, when encountering an interface between different permittivities. This explains why image reconstruction algorithms described for

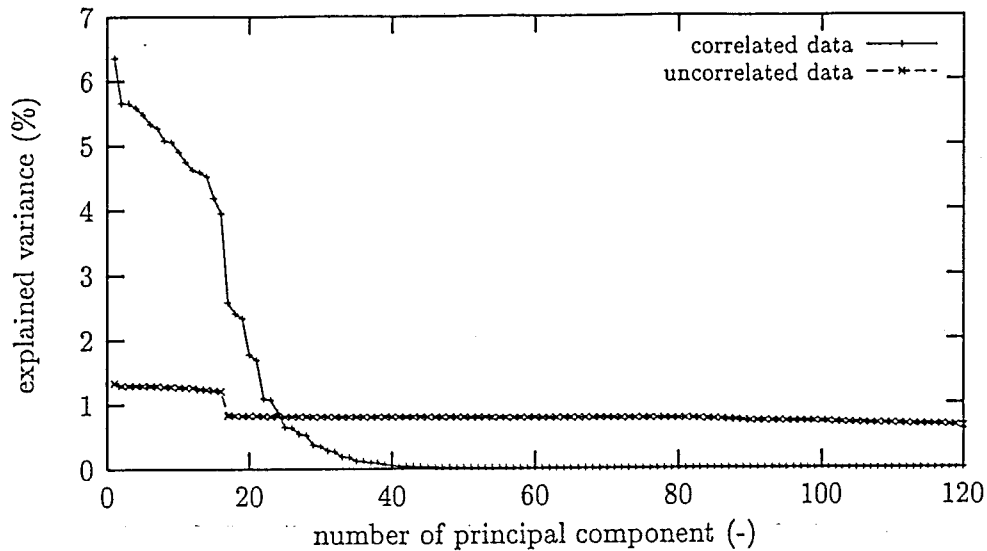
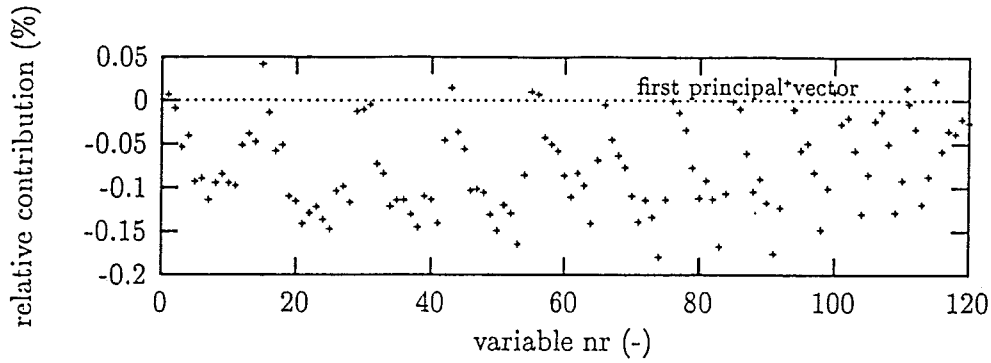


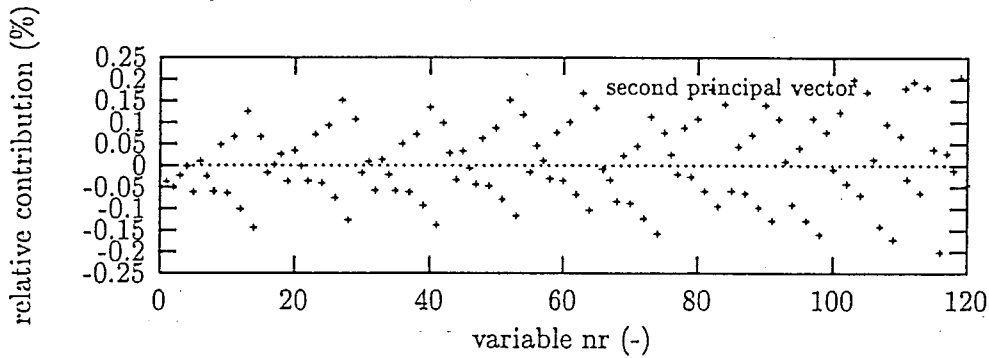
Figure 3.12: Principal Components Analysis of the 16 electrodes system with one source electrode.

straight-ray transmission tomography are not applicable in electrical capacitance tomography. When omitting the measurements between source and neighbouring electrodes the degree of nonlinearity will decrease, but will also decrease the information available for the reconstruction algorithm. In Figure 3.15 the different curves when omitting neighbour measurements and when omitting opposite measurements are shown. From this figure the differences in number of principal components carrying significant information can be seen, when omitting the measurements with strong nonlinearities and when omitting the data which are least nonlinear. Although the first *eigenvector* is dominated by contributions of the opposite electrode, the number of retained PC's decreases when omitting neighbour measurements, with respect to the case when opposite electrode measurements are omitted.

Plotting the simulation results of the 12 and 16 electrode sensor together in one figure, see fig 3.16, the differences can be seen better. From this figure it is clear that the curve of the 16 electrode system is a little more flat than the curve of the 12 electrode system, so in the 16 electrode system the information is more equally distributed among this first principal components. Interesting feature is that in the 12 electrode PCA there is a break between the 12<sup>th</sup> and 13<sup>th</sup> PC, while in the 16 electrode system this break is typically between the 16<sup>th</sup> and 17<sup>th</sup> PC. Integration of the area under these first PC's before the 'break' for the 12 electrode and 16 electrode system shows that the amount of information provided by these first PC's is almost the same for both systems. Only in the 16 electrode system the same amount of information is distributed among more PC's.



(a) First principal vector



(b) Second principal vector

Figure 3.13: First and second eigenvector of the 16 electrodes system.

### 3.4.3 Comparison of the sensitivity of the 12 electrode and 16 electrode system

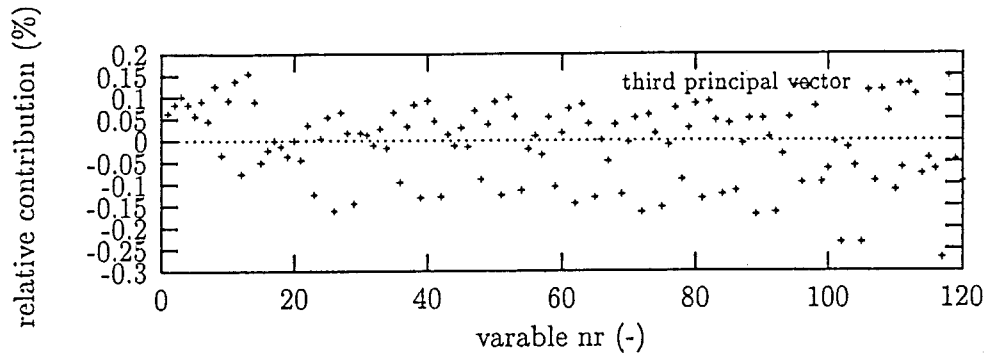
Main effort is to increase the sensitivity in the centre of the cross-section, since the problem is very ill-conditioned there (see Section 3.3.2). It must, thus, be investigated if an increased number of electrodes mounted around the pipe increases the sensitivity in the pipe-centre.

First the empty pipe capacitance values are calculated for both the 12 electrode system and the 16 electrode system. Then the capacitance values for the distribution in Figure 3.17 are calculated for both systems. This is in fact the reconstruction mesh shown in Figure 3.9, where pixel 1 is set to a permittivity value of 2 and all other pixels are set to a permittivity value of 1. Note that the circumferential length of the electrodes of the 16 electrode system is smaller. In the simulations this ratio is:

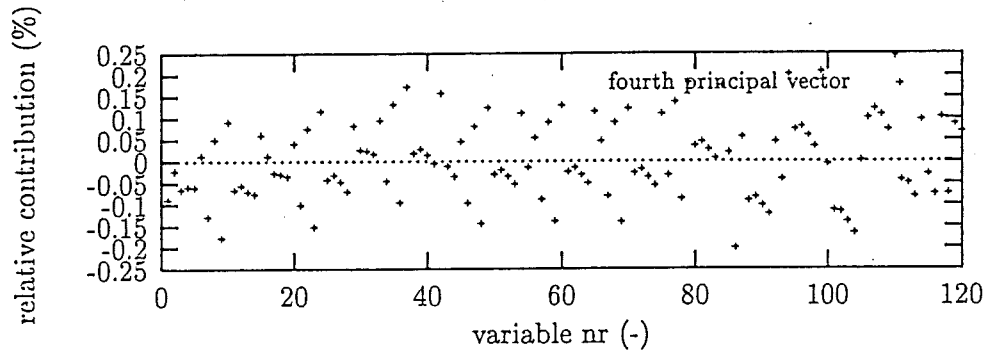
$$\frac{l_{j,12\text{electrodes}}}{l_{j,16\text{electrodes}}} = \frac{2\pi r \frac{26^\circ}{360^\circ}}{2\pi r \frac{18.5^\circ}{360^\circ}} \approx 1.4 \quad (3.9)$$

The opposite electrode combinations contain the most valuable information of the pipe-centre. Therefore, the changes in the capacitance values between opposite electrodes is inspected.

In the simulations the electrode in the pie segment, containing pixel 1, pixel 13, and



(a) Third principal vector



(b) Fourth principal vector

Figure 3.14: Third and fourth eigenvector of the 16 electrodes system.

pixel 25, is set to the source electrode and its opposite electrode is set to the detecting electrode. From the simulations the total charge on the opposite detecting electrodes of the 12 electrode and 16 electrode system can be calculated for the empty pipe and for the distribution displayed in Figure 3.17. The outcome are two values which refer to the capacitance changes on the opposite detecting electrode of the two systems. The ratio of these two calculated values is

$$\frac{C_{1,7(12\text{electrodes})}}{C_{1,9(16\text{electrodes})}} \approx 1.8 \quad (3.10)$$

This results, using Equation 3.9 for both the source electrode and the detecting one, in an increasing sensitivity of about 9% in the centre of the pipe. Note that the factor 1.8 only indicates that the measurements have to be a factor 1.8 more accurate. Since the capacitance measurements are already towards the limits of what can be measured with the electronics system, this is a hopeful outcome.

That the electric field lines prefer materials with a higher permittivity, could serve as an explanation for this effect. In the case of Figure 3.17 the electric field will be 'attracted' by the pixel with permittivity 2. Therefore the capacitance values of the electrodes next to the source electrode can decrease when an object is placed near the source electrode. In these simulations this is also the case. Remarkable is that in the 16 electrode system these adjacent electrodes capacitance values decrease much more than in the 12 electrode

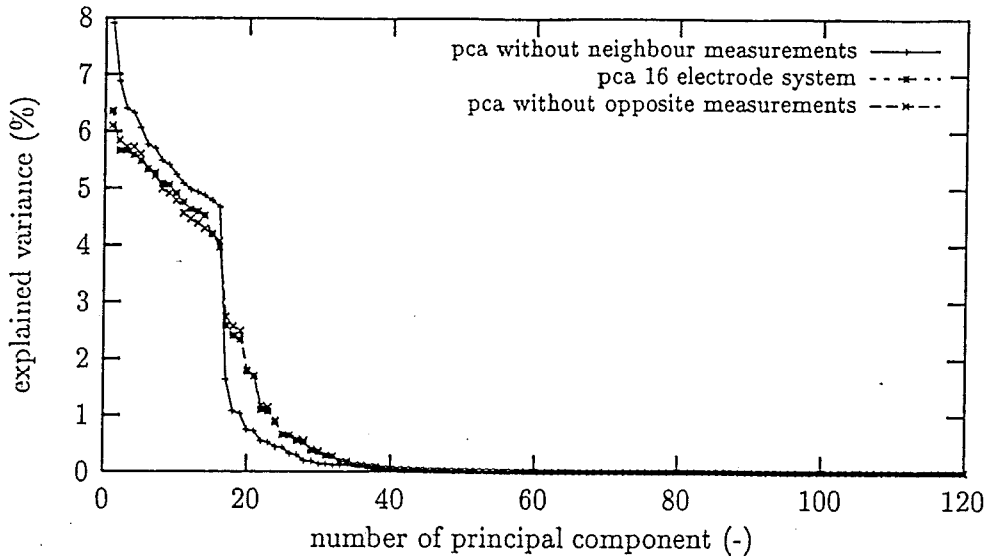


Figure 3.15: Principal components analysis of the 16 electrode system with one source electrode when omitting adjacent electrode measurements and when omitting opposite electrode measurements.

system. Here the non-linearity of the electric field becomes clear and it is shown that the adjacent electrodes are the most non-linear ones (see Appendix C).

#### 3.4.4 A new view on the 12 electrode system

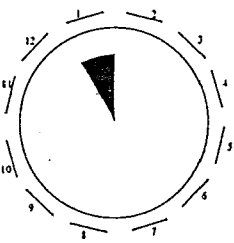


Figure 3.17: Permittivity distribution in the cross-section.

The results of the 16 electrode mesh do not yield a significant gain of principal components and yield a small increase of sensitivity in the pipe-centre, so an other sensor concept is proposed and investigated in this section. Since one of the biggest problem is the resolution in the centre of the pipe, there must be more electric field lines crossing the centre of the cross-section. More field lines must be 'pushed' through the centre of the pipe. New simulations were done to investigate the additional use of bigger source electrodes. Instead of setting one electrode to the source electrode, two electrodes are set to the source electrode.

This results in a larger source electrode, which could feed the electric field better. First electrode one and electrode two are coupled and electrodes three to twelve are set as detecting electrodes. Next electrode two and three are coupled and electrode one and electrodes three to twelve are set as detecting electrodes. Now there are no electrode pair combinations which can be omitted, like in the case of one source electrode. The capacitance between source electrode 1 coupled with electrode 2 and detecting electrode 3 is not the same as the capacitance between source electrode 2 coupled with electrode 3 and detecting electrode 1. So now there are twelve different source electrode couples together with ten different detecting electrodes per source electrode couple, resulting in 120 capacitance values. The main goal was trying to get more electric field lines to the opposite electrodes to raise the signal of the opposite electrodes and so raise the information of the

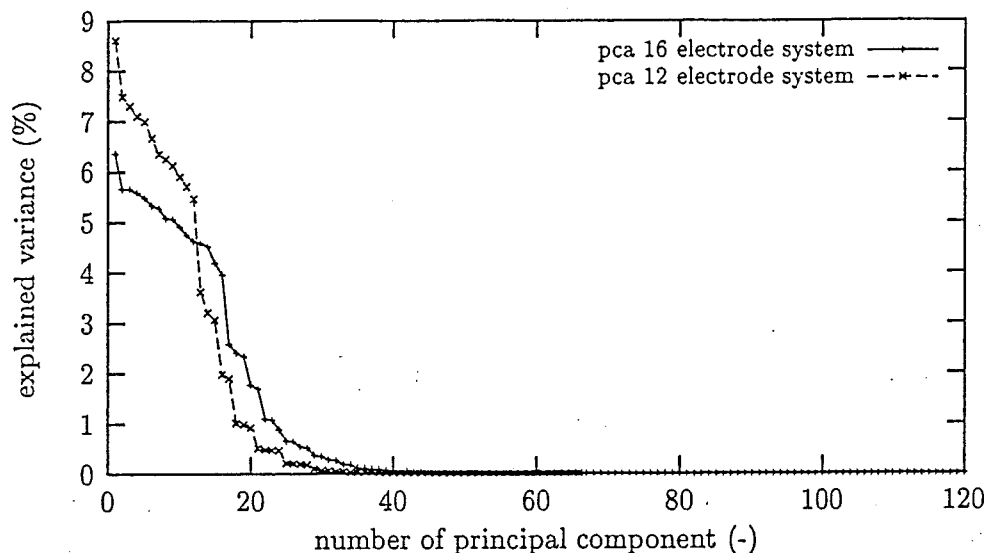


Figure 3.16: Principal components analysis of the 12 and 16 electrode system with one source electrode.

centre pixels.

In fig. 3.18 the results of the simulation are plotted. The coupled source electrode data, 12 in total, are added to the single source electrode data, 66 data points, resulting in 186 data-points.

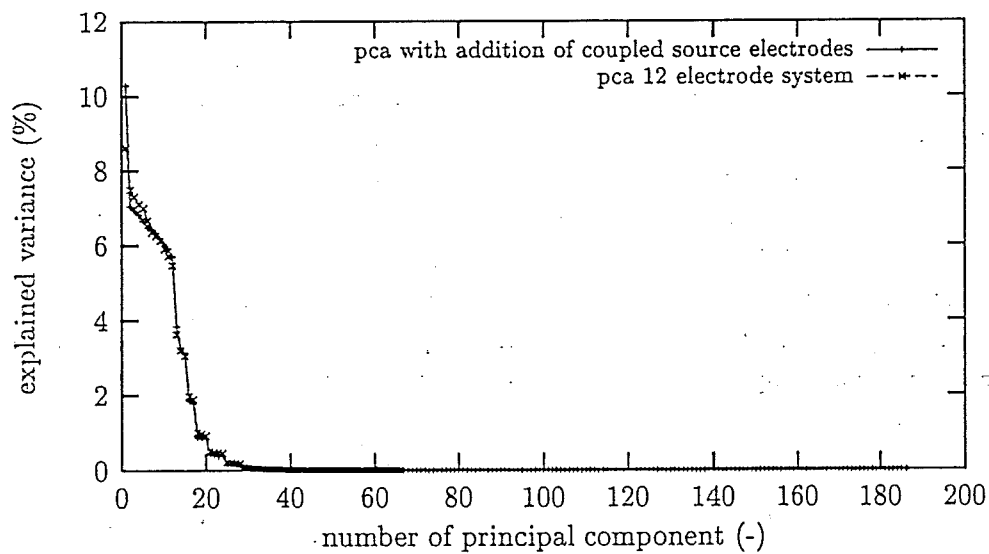


Figure 3.18: PCA of 12 electrodes system with coupled source electrodes.

## 3.5 Conclusions of the simulations

### 3.5.1 Comparison of 12-electrode system with 16-electrode system

The simulations presented in this chapter are done to investigate novel sensor concepts, which would yield a higher sensitivity in the pipe centre. A higher sensitivity in the pipe centre can improve the ill-conditioning of the inverse problem, since the inverse problem is highly under-determined (see section 3.3.2).

Looking at the PCA of the 12 electrode system and 16 electrode system, first can be noticed that the curve of the 16 electrode system is a little lower and more flat for the first PC's than the pca of the 12 electrode system. Using the scree test, the number of principal components containing significant information is about 40. With respect to the 12 electrode system, with between 25 and 30 principal components, there are four electrodes added, resulting in 120 independent measurements. So 54 more data-points can be obtained, using a 16 electrode system, which yield ten more principal components with significant information. This will give the opportunity to define more pixels in the reconstruction mesh than in the 12-electrode system. Note, that this is only a qualitative comparison. The goal is to improve the reconstruction in the centre of the cross-section, but there is not a significant improvement of the resolution in the middle of the pipe cross-section. There is an increase in the sensitivity of the pipe centre of 9%. Only a improvement near the wall of the pipe is expected, due to a larger spatial resolution at the wall, since there are more electrodes. This offers the possibility to define more near-wall pixels. However, if polar pixels are used, this will yield also more centre pixels, which results in a bigger case of under-determinacy in the centre of the pipe.

The curve of the 16 electrode system is flatter. In the 12 electrode system can be noticed that the first 12 principal components have the highest explained variance, while in the 16 electrode system this are the first 16 PC's. When the area under these first PC's is taken into account, the cause of the flatter curve for the 16-electrode system is found: the same amount of information is distributed among more PC's, resulting in a flatter curve.

From Figure 3.13 and 3.13 can be seen that the first principal component consist mainly of the measurements from detecting electrodes opposite to the source electrode. Note that the curve is scaled so in the figures the relative explained variance is plotted against the number of principal component. So these plots do not take into account the signal levels of each datum.

### 3.5.2 The 12 electrode system using coupled source electrodes

When looking at the PCA of the 12 electrode system with two-coupled source electrodes there is only one remark to make: There is no significant difference in the two curves and, thus, this sensor concept does not improve the amount of information available. This is evident, since the information provided by the coupled source electrodes are merely linear combinations of the information provided by the single source electrodes. Therefore the PCA's result in almost the same curve, as can be seen in Figure 3.18.

## Chapter 4

# Least squares based reconstruction algorithms

### 4.1 Introduction

In literature various algorithms for solving *inverse problems* are described. Up till now the image quality of the capacitance tomography reconstruction algorithms is rather poor. The most commonly used reconstruction algorithm for capacitance tomography is the *linear back projection*, which is merely a qualitative approach of the capacitance *inverse problem*. Therefore a more quantitative algorithm is desired.

At the Delft University of Technology (DUT) a new reconstruction algorithm was developed, based on *least squares* methods.

### 4.2 Mathematical model of the capacitance tomography system

#### 4.2.1 Discrete representation of the permittivity distribution

To use a reconstruction algorithm, first a mathematical formulation of the ECT problem must be formulated. Since the forward problem and the inverse problem are two integrated problems, they must be modelled on the same assumptions.

The forward problem is solved using a *Finite element method* software package and results in a discrete set of capacitances. The data obtained from one tomogram, i.e. one 'body scan' of the cross-section in figure 2.1, yields  $N$  data-points and can be written into a vector  $\mathbf{c}$ ,

$$\mathbf{c} = [c_1, c_2, \dots, c_N]^T \quad (4.1)$$

where  $c_1 \cdots c_N$  are the measured capacitances.

The inverse problem is the mapping between the measured capacitances and the model parameters  $\epsilon$ . Similar to the capacitances, the relative permittivity distribution can be

written as a vector  $\epsilon$ :

$$\epsilon = [\epsilon_1, \epsilon_2, \dots, \epsilon_M]^T \quad (4.2)$$

where  $\epsilon_i$  refers to the  $i^{\text{th}}$  permittivity value in a discrete permittivity map of  $M$  pixels [Menke, 1989].

#### 4.2.2 Direct reconstruction methods

A fast way to solve the inverse problem is with a direct method. Direct or linear methods can be used for linear problems or problems which can be approximated by a linear approach.

In section 2.3.2 the so-called *soft field effect* was introduced. Due to this *soft field effect* the inverse ECT problem is a nonlinear one. Since real-time flow-imaging, i.e. about 20 frames per second, is preferred with the electrical capacitance tomography system, a fast algorithm is needed.

Although the ECT problem is non-linear, direct methods have been developed to test whether these methods give acceptable results.

#### 4.2.3 Linearisation of the ECT problem

Now with the discrete permittivity map, the capacitance values can be coupled to the permittivity vector

$$c = f(\epsilon) + n_c \quad (4.3)$$

Here the capacitances,  $c$ , are coupled to the permittivity vector,  $\epsilon$ , by the function  $f(\epsilon)$ , which represents the deterministic forward model.  $n_c$  is an error term, containing the errors due to measurement errors.

If the error term,  $n_c$ , is neglected and the forward solution is linearised, Equation 4.3 can be rewritten to:

$$c = J \cdot \epsilon \quad (4.4)$$

where  $J$  is a  $N \times M$  matrix the meaning of which can be better understood by partitioning it in the following way:

$$J = [j_1 j_2 \dots j_N]^T \quad (4.5)$$

where  $j_n$  is a  $M \times 1$  vector related to the  $n^{\text{th}}$  capacitance value  $c_n$ .

$J$  is the Jacobian matrix whose entries are the first derivatives of any datum  $c_i$  with respect to any parameter  $\epsilon_j$ .

$$J_{ij} = \frac{\partial c_i}{\partial \epsilon_j} \quad (4.6)$$

Since it cannot be calculated analytically, it has to be approximated by finite differences.

$$J_{ij} \approx \frac{\Delta c_i}{\Delta \epsilon_j} \quad (4.7)$$

Since the permittivity distribution cannot be anticipated, this Jacobian matrix has to be calculated beforehand when using a direct, i.e. a non iterative, reconstruction method of an unknown flow distribution. Due to the non linearity of the problem, the position  $\epsilon$  where the Jacobian matrix is calculated influences the matrix components. The Jacobian matrix is namely calculated by setting one pixel at a high and a low permittivity value and then calculate the derivative of the capacitance values to the permittivity value of the pixel by finite differences. Since the capacitance values do not increase exactly linear, but show a small curve, and since a basic permittivity value for the whole cross-section has to be assumed (i.e. an average permittivity distribution over the cross-section), the Jacobian matrix changes when one of these values above (higher- and lower permittivity value  $\epsilon_{high}$  and  $\epsilon_{low}$ , and the average permittivity distribution  $\epsilon_{basis}$ ) is changed.

If the permittivity distribution can be anticipated, for example when there is already an estimate, the Jacobian should be calculated at this estimated parameter vector.

If then again this new estimated parameter vector is used to calculate the Jacobian matrix, the direct method can serve as the basis of an iterative algorithm. Note that this reduces the reconstruction speed enormous, since updating of the Jacobian matrix after every iteration is a very time consuming process.

## 4.3 Least squares based reconstruction methods

### 4.3.1 Euclidean norm

One direct method to solve the inverse problem is the method of *least squares*. This method tries to pick the model parameters so that the predicted data are as close as possible to the observed data.

In the ECT inverse problem, for each measured capacitance a prediction error, or misfit,  $e_i = c_i^{meas} - c_i^{pre}$  is defined. Here  $c_i^{meas}$  is the capacitance measured with the ECT system (See chapter 2),  $c_i^{pre}$  is the capacitance calculated from the forward solution (See chapter 3). The best fit is then the one with model parameters that lead to the smallest overall error  $E$ , defined as

$$E = \sum_{i=1}^N e_i^2 \quad (4.8)$$

The total error  $E$  is exactly the squared Euclidean length of the vector  $e$ , or  $E = e^T e$ .

This method, thus, estimates the solution by finding the model parameters that minimise its Euclidean distance from the observations [Menke, 1989].

The least squares based methods uses the  $L_2$  norm, i.e. the Euclidean length (See also section 6.2.1), to quantify length. One could also use a high-order norm, i.e. the sum of a higher power of the elements of vector  $e$ . This is in the ECT problem not preferred, since high-order norms weight the larger errors, such as outliers, preferentially. The Euclidean norm, on the contrary, gives more equal weight to errors of different size.

### 4.3.2 General linear least squares solution

The section above showed that the linear least squares method minimises the distance between the measured capacitances,  $c$  and the data predicted by the linear forward model,  $J \cdot \epsilon$ . This yields the following *objective function*  $\Phi$ :

$$\Phi = \|e\|_2 = e^T e = (c - J\epsilon)^T (c - J\epsilon) \quad (4.9)$$

The objective function must be minimised in order to minimise the distance between the measured data and the predicted data. This minimum can be found by setting the first derivative of  $\Phi$  in Equation 4.9 with respect to one of the model parameters,  $\epsilon_m$  equal to zero.

Rewriting Equation 4.9 in terms gives:

$$\Phi = \sum_i^N \left[ c_i - \sum_j^M J_{ij} \epsilon_j \right] \left[ c_i - \sum_k^M J_{ik} \epsilon_k \right] \quad (4.10)$$

Multiplying the two terms on the right-hand side and reversing the order of the summations leads to

$$\Phi = \sum_j^M \sum_k^M \epsilon_j \epsilon_k \sum_i^N J_{ij} J_{ik} - 2 \sum_j^M \epsilon_j \sum_i^N J_{ij} c_i + \sum_i^N c_i c_i \quad (4.11)$$

The derivatives  $\frac{\partial \Phi}{\partial \epsilon_p}$  have to be calculated now. Performing this differentiation term by term gives for the first term:

$$\frac{\partial}{\partial \epsilon_p} \left[ \sum_j^M \sum_k^M \epsilon_j \epsilon_k \sum_i^N J_{ij} J_{ik} \right] = \sum_j^M \sum_k^M [\delta_{jp} \epsilon_k + \epsilon_j \delta_{kp}] \sum_i^N J_{ij} J_{ik} = 2 \sum_k^M \epsilon_k \sum_i^N J_{ip} J_{ik} \quad (4.12)$$

The derivatives  $\frac{\partial \epsilon_i}{\partial \epsilon_j}$  can be replaced by the Kronecker delta  $\delta_{ij}$ . The second term gives:

$$-2 \frac{\partial}{\partial \epsilon_p} \left[ \sum_j^M \epsilon_j \sum_i^N J_{ij} c_i \right] = -2 \sum_j^M \delta_{jp} \sum_i^N J_{ij} c_i = -2 \sum_i^N J_{ip} c_i \quad (4.13)$$

Since the third term does not contain any  $\epsilon$ , it equals zero:

$$\frac{\partial}{\partial \epsilon_p} \left[ \sum_i^N c_i c_i \right] = 0 \quad (4.14)$$

Combining these three terms and demande for an extremum, thus equal it to zero, gives

$$\frac{\partial \Phi}{\partial \epsilon_p} = 0 = 2 \sum_k^M \epsilon_k \sum_i^N J_{ip} J_{ik} - 2 \sum_i^N J_{ip} c_i \quad (4.15)$$

Equation 4.15 results in  $M$  so-called normal equations. Every normal equation yields one parameter. Writing Equation 4.15 in matrix notation gives

$$\frac{\partial \Phi}{\partial \epsilon} = -2J^T (c - J\epsilon) = 0 \quad (4.16)$$

This is the square matrix equation for the unknown model parameters  $\epsilon$ . Assuming that  $[\mathbf{J}^T \mathbf{J}]^{-1}$  exists, we have the following solution:

$$\epsilon_{est} = [\mathbf{J}^T \mathbf{J}]^{-1} \mathbf{J}^T \mathbf{c} \quad (4.17)$$

which is the least squares solution to the inverse problem  $\mathbf{J} \cdot \epsilon = \mathbf{c}$  [Menke, 1989]. When the amount of information provided by the capacitance measurements is not enough to determine uniquely all the model parameters, the problem is said to be *under-determined* (see Section 3.3.2). From elementary linear algebra is known that under-determined problems occur when there are more unknowns than data. But under-determinacy can also occur due to a very poor structure of the data kernel. Solving a highly under-determined problem with least squares, one would find that the matrix  $[\mathbf{J}^T \mathbf{J}]^{-1}$  is singular or close to singular. In that case Equation 4.17 is not applicable anymore.

### 4.3.3 Linear least squares derivatives

Most inverse problem that arise in practise are neither completely over-determined nor completely under-determined. The former section already mentioned that the matrix  $[\mathbf{J}^T \mathbf{J}]^{-1}$  becomes close to singular when the inverse problem is highly under-determined. This under-determinacy can be measured with the condition number of the Hessian matrix (see Chapter 3).

Ideally, we would like to sort the unknown model parameters into two groups; the over-determined parameters and the under-determined parameters. This partitioning process can be accomplished through a *singular value decomposition* (SVD, see Chapter 3). Since this is a very time consuming process, an approximate process can be used when the problem is not too under-determined [Menke, 1989].

Also, one can use *a priori* knowledge to add more information and therefore making the inverse problem less under-determined.

### Damped least squares

Instead of minimising the objective function, Equation 4.9, a solution can be determined that minimises not only the  $\Phi$ , but also includes the solution length,  $\epsilon^T \epsilon$ .

$$\Phi = (\mathbf{c} - \mathbf{J}\epsilon)^T (\mathbf{c} - \mathbf{J}\epsilon) + \beta (\mathbf{R}\epsilon)^T (\mathbf{R}\epsilon) \quad (4.18)$$

where  $\mathbf{R}$  is a smoothing matrix [Kühn, 1997] and  $\beta$  a weighting factor, which determines the relative importance given to the prediction error and the solution length. Since matrix  $\mathbf{R}$  links the neighbouring parameters to one another and weighting factor  $\beta$  determines the importance of minimising the solution length, oscillations will be damped.

However, when the relative importance,  $\beta$ , given to the solution length is made large enough, the solution will not minimise the prediction error  $E$  and therefore will not be a very good estimate of the true model parameters. There is no simple method of determine that value of  $\beta$ , which leads to a compromise between minimising the prediction error  $E$  and the modified solution length  $(\mathbf{R}\epsilon)^T (\mathbf{R}\epsilon)$ . Clearly this value of  $\beta$ , has therefore to be determined by *trial and error*.

Minimising the *new* objective function, Equation 4.18, yields the following estimated parameters:

$$\epsilon_{est} = [J^T J + \beta R^T R]^{-1} J^T c \quad (4.19)$$

This method is also known as *Phillips-Twomey* damping [Kühn, 1997]. Note that matrix  $R$  contains information about the pixels to be linked, resulting in a smoothed solution. there are several ways to link the pixels for the reconstruction mesh, proposed in chapter 3. F.T. Kühn proposed two different smoothing matrices; linking only neighbours on the same ring, as in Figure 4.1a, and linking neighbours on the same ring as well as linking the pixels in radial direction, see Figure 4.1b.

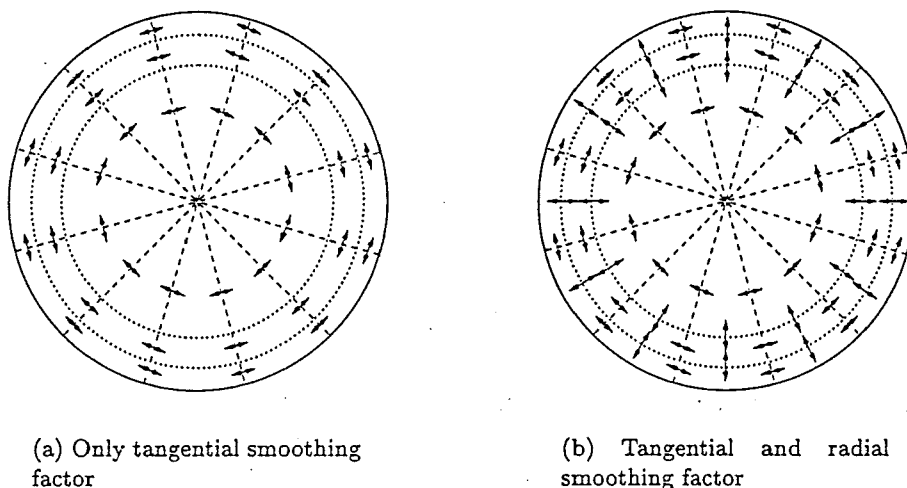


Figure 4.1: Two different smoothing ways when using the damped least squares solution

### Weighted least squares

Weighted measures of the prediction error can also be useful. If some observations are more accurate than others, one can define a matrix  $W_e$  which can be interpreted as a weighting factor that enters into the calculation of the length of the vector  $\epsilon$ . This matrix  $W_e$  gives the more accurate observations a higher weight and less accurate observations a lower weight. This can be implemented in the objective function by inserting this weighting matrix  $W_e$  as follows:

$$\Phi = e^T W_e e \quad (4.20)$$

Minimising this *weighted* objective function yields

$$\epsilon_{est} = [J^T W_e J]^{-1} J^T W_e c \quad (4.21)$$

If the observations are Gaussian distributed and the data covariance matrix (see chapter 3) is known from measurements or simulations, one can use the inverse of this data covariance matrix as weighting matrix. This is better known as the method of *maximum likelihood* [Priestley, 1981], where  $W_e = [cov(c)]^{-1}$ . Thus, the measurements are weighted by the reciprocal of their variances and covariances.

### Adding constraints to bound the solution space

In many cases the parameters to be estimated are expected to fall within some interval. In this case the solution space can be bounded by defining an interval with both a lower bound and an upper bound. Using these *constraints* one can force the solution to fall within this pre-defined interval. This type of *a priori* knowledge is referred to as adding *hard constraints*.

Although this section describes direct inversion methods, the *constraint least squares* method is merely an iterative algorithm, since it iteratively modifies the Jacobian matrix until the parameters fall within the bounded solution space. While modifying the Jacobian matrix the *Kuhn-Tucker* is used, giving the minimum solutions to the constraint problem [Menke, 1989].

In the electrical capacitance parameter estimation problem hard constraints can be implemented by introducing a lower bound and upper bound to the permittivity value to be found. Note that using constraint least squares also reduces, in general, oscillations in the solution vector,  $\epsilon_{est}$ .

#### 4.3.4 Hybrids of least squares derivatives

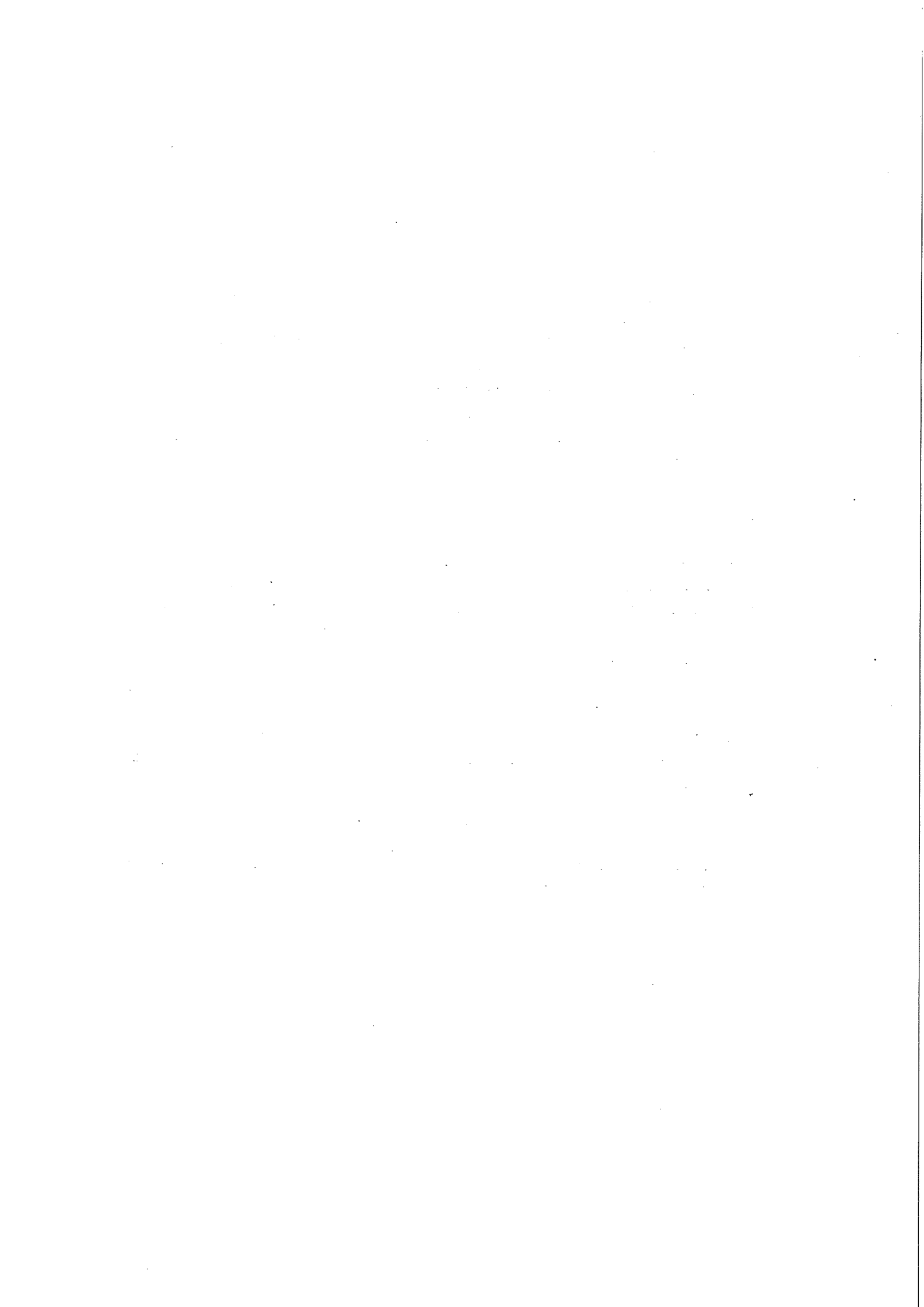
The former section showed some least squares derivatives, which can be used to solve the inverse problem. These proposed methods can also be combined to new inverse problems, resulting in a new objective function containing the properties of both separate methods. Combining the damped least squares method and the weighted least squares method yields a new objective function:

$$\Phi = (\mathbf{c} - \mathbf{J}\epsilon)^T \mathbf{W}_e (\mathbf{c} - \mathbf{J}\epsilon) + \beta (\mathbf{R}\epsilon)^T (\mathbf{R}\epsilon) \quad (4.22)$$

With this objective function a combination of minimising both the prediction error and the solution length,  $E + \beta\epsilon^T\epsilon$ , can be achieved. Once again  $\beta$  must be chosen by trial and error. The estimate of the solution is then

$$\epsilon_{est} = [\mathbf{J}^T \mathbf{W}_e \mathbf{J} + \beta (\mathbf{R}\epsilon)^T (\mathbf{R}\epsilon)]^{-1} \mathbf{J}^T \mathbf{W}_e \mathbf{c} \quad (4.23)$$

Hybrids of the constraint method can be achieved by simply applying hard constraints to the three proposed inversion methods.



## Chapter 5

# Noise in ECT sensor electronics

### 5.1 Introduction

The aim of this research project includes also to investigate the influence of noise on the reconstruction algorithms, proposed in chapter 4. This influence is investigated in two different ways:

1. Addition of simulated noise to exact data from simulations. This is described in chapter 6.
2. Reconstruction of real measurements, as described in chapter 7.

Therefore, the noise level of the electrical capacitance sensor has to be determined, so the noise can be modelled and subsequently added to the exact simulated data.

The Delft University of Technology (DUT) has two different types of sensor electronics: an electrical capacitance system bought from the *University of Manchester* (UMIST) and a new electronics system, which is being developed at the DUT. Both systems were used to perform the noise measurements, in order to compare the new developed electronics to the electronics provided by UMIST.

### 5.2 The UMIST system and the DUT system

#### 5.2.1 The UMIST system

The University of Manchester has designed sensor electronics for the electrical capacitance system, which is based on the *charge-transfer principle*. This electrical capacitance sensor has a data acquisition speed of 6600 measurements per second. It is designed for a 12 electrode capacitance sensor and can capture cross-sectional images of the contents of pipes and tanks at a rate up to 100 frames per second.

The system was delivered with image reconstruction software, based on the linear back projection. This software computes images in real time using a network of transputers operating in parallel and controlled by a personal computer.

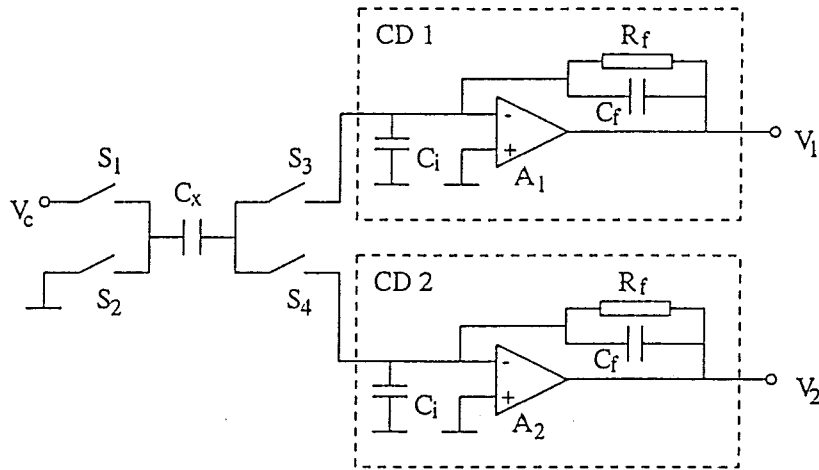


Figure 5.1: The charge transfer principle used in the electrical capacitance tomography system developed by UMIST.

### 5.2.2 The DUT system

The image resolution of ECT is significantly poorer than that of non-electrical tomography techniques. This is also due to the limited sensitivity of the *charge-transfer principle* used in the UMIST system. A better performance of ECT can be achieved by reducing the measurement noise. Also, increasing the number of electrodes and reducing the axial length of the measuring electrodes will increase the performance, but results in smaller capacitances to be detected. Therefore at the DUT a capacitance transducer is being developed which uses the unknown capacitance as an element of an active differentiator. This system is designed for a maximum data acquisition speed of 9000 frames per second for a 12 electrode system.

### 5.2.3 The two circuits

#### Charge transfer

Figure 5.1 shows the UMIST electronics circuitry based on the *charge-transfer* principle. The source electrode of the unknown capacitance is connected to a pair of CMOS switches, S1 and S2 and the detecting electrode is connected to the switches S3 and S4. In a typical operating cycle, the switches S1 and S3 are first closed and S2 and S4 are open. The unknown capacitance,  $C_x$ , is then charged to voltage  $V_c$ , and the charging current flows into the input of the current detector CD1 where it is converted into a negative voltage output. In the second half of the cycle, switches S2 and S4 are closed and S1 and S3 are left open. The capacitance  $C_x$  discharges then to earth potential, and causes a discharging current, which flows out of the current detector CD2, resulting in a positive voltage output. The successive current pulses in CD1 and CD2 produce two d.c. output voltages

$$V_1 = -fV_cR_fC_x + e_1 \quad (5.1)$$

$$V_2 = fV_cR_fC_x + e_2 \quad (5.2)$$

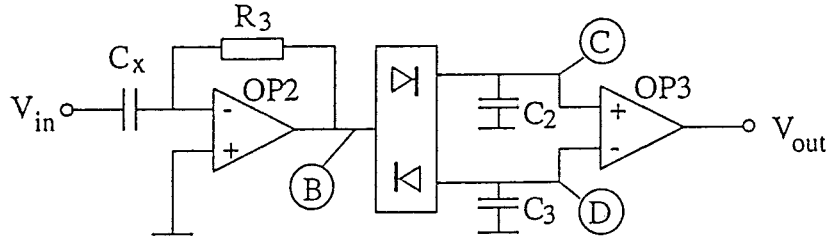


Figure 5.2: The capacitance to voltage transducer, developed at the DUT. The unknown capacitance  $C_x$  is used as an element in an active differentiator.

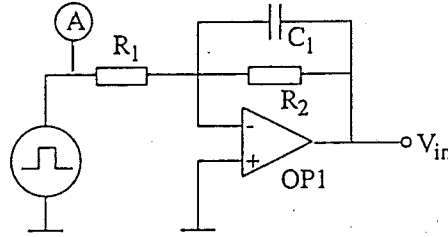


Figure 5.3: Circuit providing the input signal,  $V_{in}$ , to the measurement electrode  $C_x$ .

where  $f$  is the typical frequency of the *charge-discharge* cycle and  $e_1$  and  $e_2$  are output offset voltages, caused mainly by the charge injection effect of the CMOS switches. The differential output voltage,  $V_2 - V_1$  is taken as the output signal of the basic circuit. This has the advantage that the two offset voltages  $e_1$  and  $e_2$  tend to cancel each other, provided that the charge injection effects of both current detectors are similar [Huang et al., 1992].

### Active differentiator

Figure 5.2 shows the circuitry developed at the DUT. Here the unknown capacitance,  $C_x$ , is an element in an active differentiator. A negative pulse with well-defined fall and rise time and a constant amplitude is applied to the active differentiator as input signal,  $V_{in}$ . The circuit in Figure 5.2 differentiates and amplifies this signal, yielding a positive peak and a negative one. Since the sum of their absolute values is independent of the baseline potential, a peak peak detector splits the two subsequent peaks at point B into two constant signals with amplitudes  $U_c$  at point C and  $U_D$  at point D. These two voltages are added by a differential amplifier to the output voltage  $V_{out}$ .

This output voltage  $V_{out}$  is directly related to the unknown capacitance,  $C_x$ , by the following equation:

$$C_X = \frac{V_{out}}{R_3 \cdot \frac{\Delta U_{in}}{\Delta T}} \quad (5.3)$$

Here  $\frac{\Delta U_{in}}{\Delta T}$  is the slope of the potential fall and rise of the input signal. Figure 5.3 shows the circuitry, which provides the input signal to the measurement electrode. The slope of the potential fall and rise is a function of electrode  $C_1$  and resistance  $R_1$  [Kühn and van Halderen, 1997].

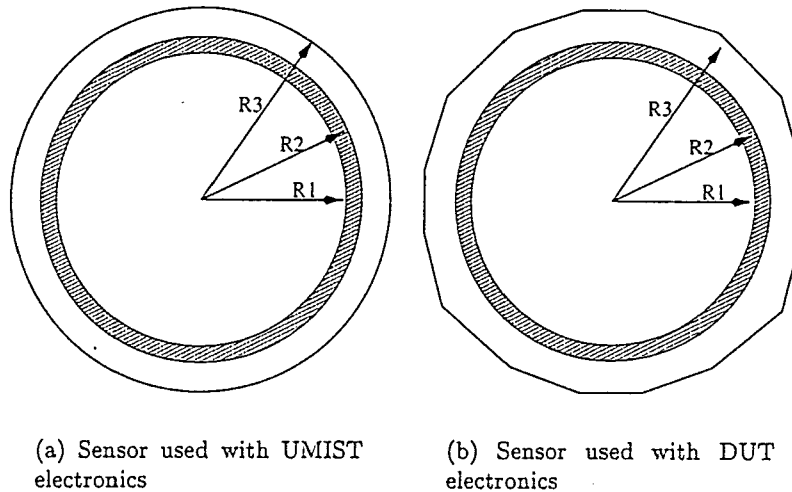


Figure 5.4: Cross-section of the two ECT sensors used for the noise measurements.

## 5.3 Noise measurements

### 5.3.1 Signal to noise ratio

Due to noise generated by the sensor electronics of the tomography systems, the measurement outcome always fluctuates randomly in time, even when the distribution inside the cross-section is constant. This noise can be quantified by the *signal to noise ratio* defined as

$$SNR = \frac{\bar{c}}{\sqrt{\frac{\sum_i (c_i - \bar{c})^2}{N}}} \quad (5.4)$$

Here the formula in the denominator is the root-mean-square value of the signal.

### 5.3.2 Experimental system

The systems are tested in different sensors, since the DUT electronics is still under development and therefore is coupled to a fixed test sensor. Both the sensors are *METC-type* sensors (see Figure 2.2). A cross-section of the used test sensors is shown in Figure 5.4. The outer screen of the DUT sensor is not circular but for practical reasons angular. Also the pipe geometries are different, as shown in table 5.1. The diameter, however, is chosen to be of the same order, since then the 3-D effect is almost the same for both sensors. The pipe-wall of the sensors are made of perspex. The permittivity of perspex is 2.9. The spacing between  $R_2$  and  $R_3$  is filled with air (permittivity 1).

These differences in the sensor geometry will have no influence on the noise measurements, since only fluctuations in the signal are significant for the noise. The geometry parameters determine only the absolute capacitance value.

The electrodes in both sensors are manufactured by gluing rectangular pieces of self-adhesive  $76\mu\text{m}$  copper foil to the outer wall. Between the electrodes of the sensor used with the UMIST electronics there is a spacing of  $3\text{mm}$  in circumferential direction and

Table 5.1: Geometry parameters of the sensors used for the noise measurements

method	UMIST sensor vs DUT sensor	
	UMIST	DUT
R1(m)	$9.8 \cdot 10^{-2}$	$9.1 \cdot 10^{-2}$
R2(m)	$10.1 \cdot 10^{-2}$	$9.4 \cdot 10^{-2}$
R3(m)	$11.0 \cdot 10^{-2}$	$11.1 \cdot 10^{-2}$

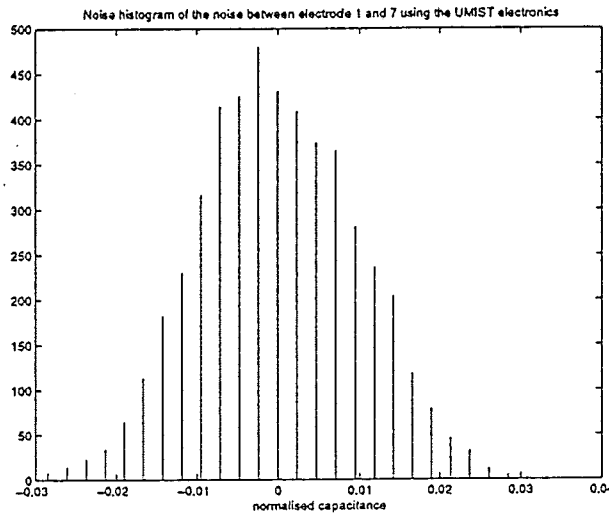


Figure 5.5: Histogram of the noise measured between electrode 1 and electrode 7 using the UMIST electronics.

between the electrodes of the sensor used with the DUT electronics a spacing of  $2mm$ . The axial length of the measuring electrodes,  $l_{ax}$ , is  $5cm$  for both sensors. Since the UMIST system only returns normalised capacitance values and not absolute capacitance values (see Section 7.2.4), absolute capacitance values for the UMIST electronics can be approximated using the capacitance values from simulations.

## 5.4 Results

### 5.4.1 UMIST electronics

The noise measurements are performed using 4900 tomograms from the UMIST electronics system. Since the smallest capacitance occurring in a capacitance sensor is the capacitance between opposite electrodes, the capacitance measurements between opposite electrodes are used to determine the *signal-to-noise* ratio. The noise behaviour was tested using the sensor shown in Figure 5.4a. Figure 5.5 shows the histogram of the noise measured between electrode pair combination 1 and 7. On the x-axis the normalised capacitance is plotted. Note, that the offset values, see Section 7.2.4, are not as accurate as expected. Therefore also the mean of the normalised capacitance is subtracted from the measured capacitances, resulting in a Gaussian-like histogram with zero mean. Since the standing

capacitance value between electrode 1 and 2 is about 100 times larger than the standing capacitance value between electrode 1 and 7, the UMIST electronics uses a calibration procedure to balance the standing offsets of the measurements and has a programmable gain amplifier to satisfy the different sensitivity requirements. With this calibration procedure, difficulties for the capacitance measuring circuit due to the limited dynamic range are overcome.

The relative standard deviation of the noise measured is 0.99%. Huang *et al* [Huang *et al.*, 1992] also tested their *charge-transfer* electronics, but used a 12 electrode capacitance sensor with an axial electrode length of 10 cm. The smallest capacitance value for this sensor is 15 fF and they found the standard deviation of the noise to be 0.08 fF, corresponding to a relative standard deviation of 0.53%.

A similar 12-electrode sensor with an axial electrode length of 5 cm is used in these experiments. Therefore the minimum capacitance value is half the value found by Huang. Equation 3.3 has to be multiplied with the axial electrode length to calculate the capacitance value, thus a reduction of the axial electrode length by a factor 2 will reduce the capacitance value by a factor 2.

Since the measurements with the UMIST electronics resulted in a relative standard deviation of 0.99%, it can be concluded that the standard deviation of the noise has a constant offset of about 0.08 fF and is independent of the capacitance to be measured.

#### 5.4.2 DUT electronics

The new differentiator electronics have been tested using the sensor in Figure 5.4b. The test-software allowed up to 500 tomograms per measurement session, so the results are based on 500 tomograms, which is significantly lower than the number of tomograms used for the UMIST electronics.

The maximum data capture rate is 9000 frames per second, which is significantly higher than the charge-transfer electronics. Figure 5.6 shows the histogram of the noise between electrode 1 and electrode 7. On the x-axis the discrete values of  $V_{out}$  from the ADC are plotted. The DUT capacitance measuring circuit has a fixed dynamic range, so a calibration procedure to learn the 66 zeros and required gains as with the charge-transfer electronics is not needed. This explains the limited number of discrete levels for  $V_{out}$ . Therefore, the histogram in Figure 5.6 is not as smooth as the histogram in Figure 5.5. However the relative standard deviation of the noise is 0.97%. Since the data acquisition speed is up to 9000 frames per second, the noise can be reduced by averaging multiple measurements.

Two ways of averaging are tested:

- Averaging multiple subsequent measurements. This reduces the data capture rate. Averaging two subsequent measurements, for example, results in a data capture rate of 4500 frames per second.
- Smooth the measurements by averaging a data point with previous data points and subsequent data-points (moving average). This will reduce high frequency fluctuations.

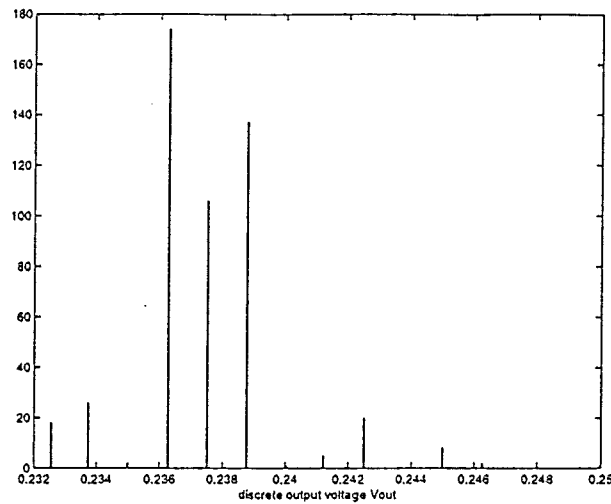


Figure 5.6: Histogram of the noise measured between electrode 1 and electrode 7 using the DUT electronics.

Table 5.2: Relative standard deviation of the noise when averaging over subsequent measurements.  $N$  represents the number of measurements in one segment.

N	Averaging over segments	
	Data capture rate ( $\frac{\text{frames}}{s}$ )	Relative standard deviation (% of minimum signal level)
1	9000	0.97
3	3000	0.62
5	1800	0.52
7	1285	0.44
9	1000	0.35

In Table 5.2 the results are shown when averaging subsequent measurements. All values have been found using steady-state measurements of the diametrically electrodes. As can be seen from this table the relative standard deviation is decreasing with  $\sqrt{N}$ , when  $N$  is the number of measurements averaged and, thus, is in agreement with the literature [van Soest, 1992].

Table 5.3 shows the results obtained when a measurement is linked with previous and subsequent measurements. When  $N$  equals 3, for example, measurement  $c_i(n)$  is smoothed with measurement  $c_i(n-1)$  and  $c_i(n+1)$  as follows:

$$\frac{c_i(n-1) + c_i(n) + c_i(n+1)}{3} \quad (5.5)$$

This smoothed data-series contains, thus, besides the segments of table 5.2 also all other possible segments constructed with  $N$  subsequent measurements. Therefore, the number of data points remains almost the same as the original number of data points, but fluctuations at high frequency are damped. Depending on the number of frames per second and the velocity of the object to be measured, i.e. the time that the object is in the measuring cross-section of the sensor, it has to be determined if this partitioning in segments does not result in too much loss of information.

Table 5.3: Relative standard deviation of the noise when smoothing using previous and subsequent measurements.  $N$  represents the number of measurement used for smoothing.

N	Relative standard deviation (% of minimum signal level)
1	0.97
3	0.60
5	0.50
7	0.43
9	0.38

### 5.4.3 DUT electronics versus UMIST electronics

Besides the high data acquisition speed of the DUT electronics in comparison with the *charge-transfer* electronics, there are more advantages of the differentiator electronics.

The differentiator electronics does not contain CMOS switches, which are the weakest elements of the *charge-transfer* electronics. They have an inner capacitance, which is large compared to the capacitances to be measured, making the electronics susceptible for external influences.

The *charge-transfer* electronics are connected to the capacitance sensor with coaxial cables. These cables have capacitances also. Small displacements of these coaxial cables influence the capacitance measurements. The measuring channels of the differentiator electronics are mounted closely to the sensor, so no coaxial cables are required.

## 5.5 Conclusions

In this chapter the noise of two different capacitance measuring circuits for electrical capacitance tomography is investigated. The active differentiator, developed at the Delft University of Technology, has been found to be superior to the *charge-transfer* electronics. The new system enables very high data capture rates in comparison with the *charge-transfer* based electronics. The noise level is nearly the same for both systems when operating at maximum data acquisition speed. However, due to the high data acquisition speed of the DUT-electronics, the noise level can be reduced by averaging subsequent measurements.

Furthermore, the new system avoids CMOS switches, which have an inner capacitance which is large compared to the capacitance to be measured and the system does not use coaxial cables to connect the sensor to the electronic circuit, avoiding influences on the capacitance measurements due to displacements of these cables.

## Chapter 6

# Robustness of the least squares inversion methods

### 6.1 Introduction

This chapter deals with the robustness of the least squares based inversion methods used for ECT application. These methods give satisfactory results for several simple test cases, when inverting perfect data from simulations of the test cases.

Real data are noisy. The sensitivity of the inversion algorithms to noise indicates the robustness of the algorithm. If an algorithm is not sensitive to the noise level of real data, it is said to be robust. The influence of the noise on the reconstructions has been investigated by using exact data simulated by the *finite element software package* SEPRAN (FEM) and then adding different levels of Gaussian noise to them. Looking at the errors in the model parameters estimated and at the goodness of the fit to the inverse model gives an indication of the robustness of the algorithms.

### 6.2 Definition of the $SS_{mod}$ and the $SS_{res}$

#### 6.2.1 General definition of a norm

To investigate the influence of noise on the reconstruction we need a measure of the error in the reconstruction introduced by the noise. This can be done by using a norm, which indicates the length of a vector. A simple example of a norm is the absolute value function, which measures the distance of a scalar from the origin. The absolute value  $|\epsilon|$  of a number  $\epsilon$  may be defined by the equation [Stewart, 1973]:

$$|\epsilon| = \sqrt{\epsilon^2} \quad (6.1)$$

In general, a vector norm on  $\mathbb{R}^n$  is a function  $\nu : \mathbb{R}^n \rightarrow \mathbb{R}$  that satisfies the following conditions:

1.  $\nu(0) = \nu(0 \cdot \epsilon) = 0\nu(\epsilon) = 0$

2.  $\nu(\epsilon) > 0$  (positive definite)
3.  $\nu(\alpha\epsilon) = |\alpha|\nu(\epsilon)$  (homogeneous)
4.  $\nu(\eta + \epsilon) \leq \nu(\eta) + \nu(\epsilon)$  (triangle inequality)

when investigating the difference between two vectors, one can look at the vector containing the differences between the individual elements of these two vectors. Two measures that meet these requirements are the so-called  $SS_{mod}$  and  $SS_{res}$ .

### 6.2.2 Definition of the $SS_{mod}$

The simplest norm in the inversion problem is the  $SS_{mod}$ , given by:

$$SS_{mod} = (\epsilon_{est} - \epsilon_{true})^T (\epsilon_{est} - \epsilon_{true}) \quad (6.2)$$

The  $SS_{mod}$  measures the difference between the presumed permittivity vector  $\epsilon_{true}$ , i.e. the inputs to the forward problem, and the estimated permittivity vector  $\epsilon_{est}$  found by solving the inverse problem (see Figure 6.1a).

If the data are simulated, both the presumed permittivity values and the estimated permittivity values are known, hence the  $SS_{mod}$  can be calculated.

In the ideal case, the  $SS_{mod}$  equals zero, which means there are no differences between the presumed permittivity values and the permittivity values estimated. When real measurements are to be reconstructed, the permittivity values inside the cross-section and, consequently, the  $SS_{mod}$  are unknown.

### 6.2.3 Definition of the $SS_{res}$

When the presumed permittivity values or the true permittivity values are not known beforehand, the  $SS_{res}$  can still be used. In formula, this measure is given by:

$$SS_{res} = (c - c_0 - J(\epsilon_{est} - \epsilon_0))^T (c - c_0 - J(\epsilon_{est} - \epsilon_0)) \quad (6.3)$$

in which  $c_0$  is the vector containing the capacitance values when the cross-section is empty, i.e. filled with air,  $\epsilon_0$  contains the empty pipe permittivity values,  $c$  contains the measured capacitance values,  $J$  is the Jacobian matrix, and  $\epsilon_{est}$  contains the estimated permittivity values. The vectors  $\epsilon_0$  and  $c_0$  are only used for normalisation and do not have any influence on the  $SS_{res}$ .

The  $SS_{res}$  gives an indication of the goodness of the fit. It measures the distance between the data points and the data calculated by the forward model using  $\epsilon_{est}$  (see Figure 6.1b).

### 6.2.4 Is there a relation between the $SS_{mod}$ and $SS_{res}$ ?

Figure 6.1 illustrates the difference between the  $SS_{mod}$  and the  $SS_{res}$ . In Figure 6.1a the  $SS_{mod}$  is displayed. On the x-axis the 36 reconstruction pixels, are plotted, on the

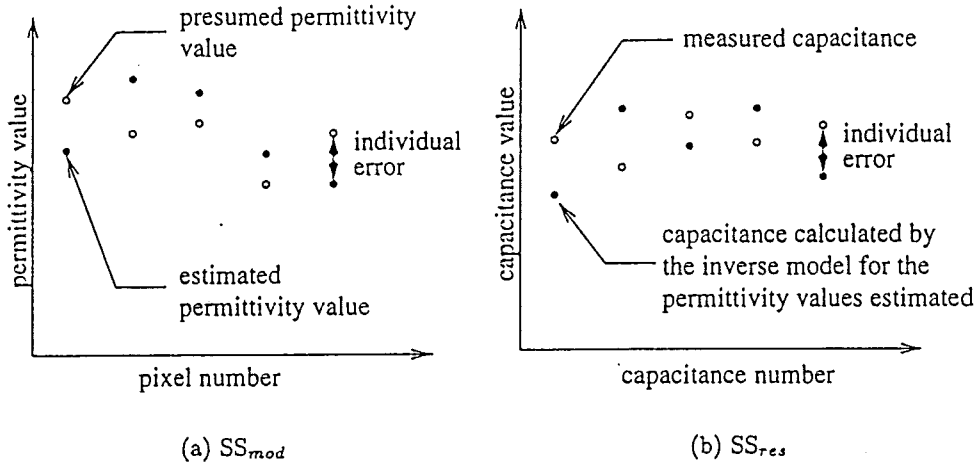


Figure 6.1: General interpretation of the  $SS_{mod}$  (a) and the  $SS_{res}$  (b).

y-axis the permittivity values of these parameters are plotted. The black dots represent the presumed permittivity values, the open dots the permittivity values estimated, when using an inverse algorithm. The  $SS_{mod}$  is the sum of the squared individual distances.

In Figure 6.1b the datum numbers, i.e. the 66 capacitance measurements, are plotted on the x-axis, and on the y-axis the capacitance values. The black dots represent the capacitance values measured (or the capacitance values calculated directly from SEPRAN). The open dots represent the capacitance values calculated for the permittivity values estimated using a least squares based inversion method. The  $SS_{res}$  is the sum of the squared individual distances.

Thus, the  $SS_{mod}$  serves to quantify the quality of an inverse model, so the error made on the parameter side. The  $SS_{res}$ , on the other hand, measures the misfit of the model, which is the error made on the data side. Therefore these two measures, in general, do not have a relation.

Though, when the estimated permittivity distribution does not change by the added noise, the value of  $SS_{mod}$  does not change. The capacitances calculated from the forward solution do not change, either. The  $SS_{res}$  depends in this case only on the absolute noise level added. When the permittivity values estimated start to change, the  $SS_{res}$  will generally increase more rapidly. Since then not only the noise added, but also the permittivity values estimated change the  $SS_{res}$ .

On the contrary, when  $SS_{mod}$  does not change and  $SS_{res}$  does not change much, it does not indicate that the estimated parameter vector  $\epsilon_{est}$  is not changed, either.

By inspection of the estimated permittivity vectors for different noise levels, it can be investigated if the estimated parameter vectors  $\epsilon_{est}$  are identical up to a certain noise level. And if so, it can be concluded that, if the model used for reconstruction is accurate enough, the  $SS_{res}$  will give an indication of the quality of the reconstruction.

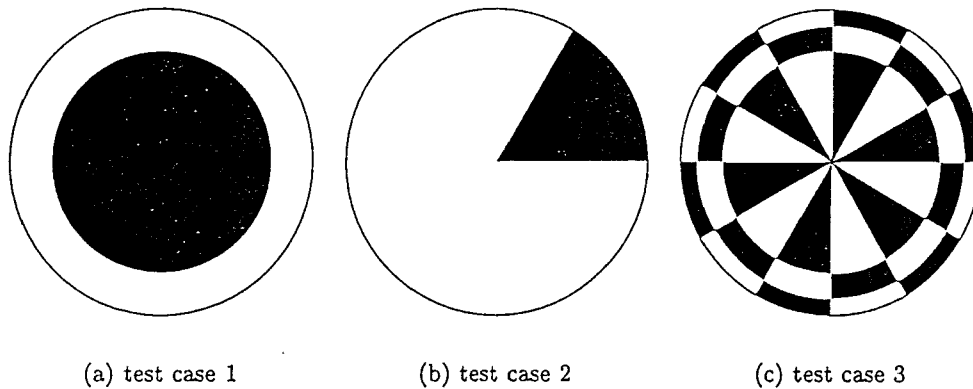


Figure 6.2: plots of the presumed phantom distributions: (a) the core flow (a), The pie-shaped segment (b), and the 'dart-board' like distribution (c). Black refers to a permittivity value of 2, white refers to a permittivity value of 1.

### 6.3 Definition of the test cases

To quantify the influence of the noise on the  $SS_{mod}$  and the  $SS_{res}$ , the forward problem is solved for presumed permittivity distributions  $\epsilon_{true}$ . This is done using the FEM software package SEPRAN, which calculates the 66 capacitances occurring in a 12-electrodes sensor.

Reconstructing the permittivity values from these data will give an indication of the errors introduced by linearisation and discretisation, i.e. only mathematical errors. Adding noise to the exactly calculated capacitances allows to investigate the influence of noise on the reconstruction. In this way real data can be mimicked.

The three permittivity distributions shown in Figure 6.2 are used in this simulation. The first represents a core flow, which is a rotational symmetric test case. Test case two is a pie-shaped segment, so there's no rotational symmetry anymore, only mirror symmetry. The last test case looks like a dart board. First the permittivity values are reconstructed from the exactly calculated capacitances, i.e. the capacitances resulting from the forward problem without noise added.

### 6.4 Reconstructions without adding noise

Table 6.1 shows the values of  $SS_{mod}$  and  $SS_{res}$ , using different least squares based inversion methods. The  $SS_{mod}$ , in general, decreases when adding 'a priori' knowledge. This is evident, since adding more information to find the solution, in general leads to a better solution.

On the contrary, adding more 'a priori' knowledge increases the  $SS_{res}$ , meaning the model does describe the data points less accurate. This is evident, since changing the estimated permittivity values towards the true permittivity values, in general, increases the distance between the capacitances measured and the capacitances estimated using the model. The unrestricted solution searches for the absolute minimum in  $SS_{res}$ . Hence, it is likely that

Table 6.1:  $SS_{mod}$  and  $SS_{res}$  of the different least squares based solutions of the three phantom distributions.

method	SS <sub>mod</sub> vs SS <sub>res</sub>					
	SS <sub>mod</sub> case <sub>1</sub>	SS <sub>res</sub> case <sub>1</sub> ( $\frac{F^2}{m^2} \cdot 10^{-25}$ )	SS <sub>mod</sub> case <sub>2</sub>	SS <sub>res</sub> case <sub>2</sub> ( $\frac{F^2}{m^2} \cdot 10^{-25}$ )	SS <sub>mod</sub> case <sub>3</sub>	SS <sub>res</sub> case <sub>3</sub> ( $\frac{F^2}{m^2} \cdot 10^{-25}$ )
linear ls	$5.6 \cdot 10^{-1}$	0.01	$2.7 \cdot 10^{+3}$	0.70	$1.9 \cdot 10^{+1}$	0.01
damped ls	$1.8 \cdot 10^{-1}$	0.10	$7.2 \cdot 10^{-1}$	2.05	9.0	0.20
weighted ls	$6.7 \cdot 10^{-1}$	232.10	3.6	800.14	$8.3 \cdot 10^{-1}$	124.60
constrained ls	0	0.13	$1.5 \cdot 10^{-1}$	12.48	$1.8 \cdot 10^{+1}$	0.04

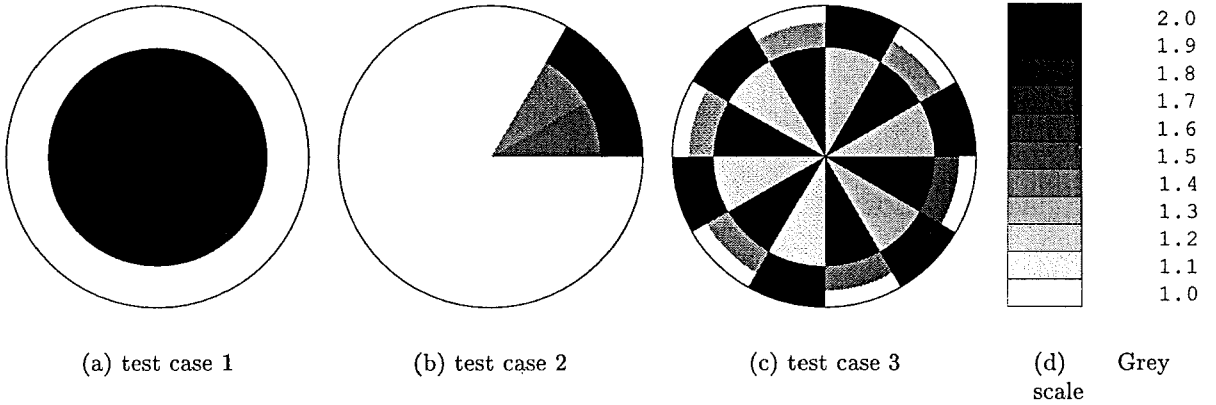


Figure 6.3: Reconstructions of the phantom distributions when no noise is added, using the constrained least squares solution.

in the restricted case a different minimum for  $SS_{res}$  is found.

Note that the dimension  $\frac{F^2}{m^2}$  for the  $SS_{res}$  is due to scaling the capacitance value with respect to the axial electrode length.

Figure 6.3 shows the reconstructions of the test cases using the constrained least squares method. Only reconstructions of the constrained least squares method are displayed since these solutions are physically correct, i.e. the solutions are bounded to the highest permittivity value and the lowest permittivity value used in the experiment.

The reconstructions of the three test cases have different accuracies. The core flow, for example, is reconstructed perfectly by the constrained least squares solution, while the pie-shaped segment has some errors, when reconstructed by the constrained least squares solution. The dart-board like distribution is not reconstructed well, but can be reconstructed much better using the weighted least squares method, displayed in Figure 6.4.

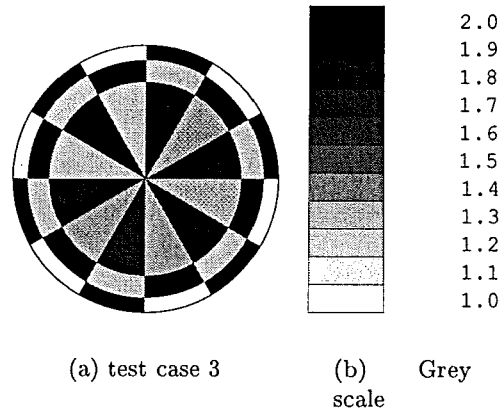


Figure 6.4: Reconstruction of phantom distribution 3 when no noise is added, using the weighted least squares solution.

## 6.5 Results achieved when adding simulated noise

### 6.5.1 Adding noise to the exact calculated capacitances

As mentioned in the sections above, Gaussian noise has been added to the exact capacitances, obtained from the forward solution, and reconstruction of the permittivity values is performed again. To determine the noise level, real measurements have been performed using the DUT-electronics. These electronics have been tested in order to investigate the signal to noise ratio for a comparison with the UMIST electronics. The noise level was of the same order as the Umist electronics. The standard deviation of the minimum signal level amounts to 0.08 fF, which is about 1% of the minimum signal level occurring in a 12-electrodes sensor (5 cm axial electrode length). This minimum signal level is found between opposite electrodes. The noise is Gaussian distributed and the absolute noise level is independent of the capacitance measured.

A Gaussian distribution with a standard deviation equal to that of the noise from the real measurements is used as noise model. This results in a new set of capacitance values, which in fact are the exact capacitances plus a noise value, extracted from the Gaussian noise distribution. Reconstruction of this new set of capacitances yields new estimated permittivity values. This new set of permittivity values can be compared with the permittivity values reconstructed when no noise was added, by inspection of the  $SS_{mod}$  and the  $SS_{res}$ .

To investigate the influence of the noise for different noise levels, the added noise is increased logarithmically. These different noise levels have been added to the simulated data, and the effect on the **linear least squares** solution and the **constrained least squares** solution has been investigated using the three test cases shown in Figure 6.2.

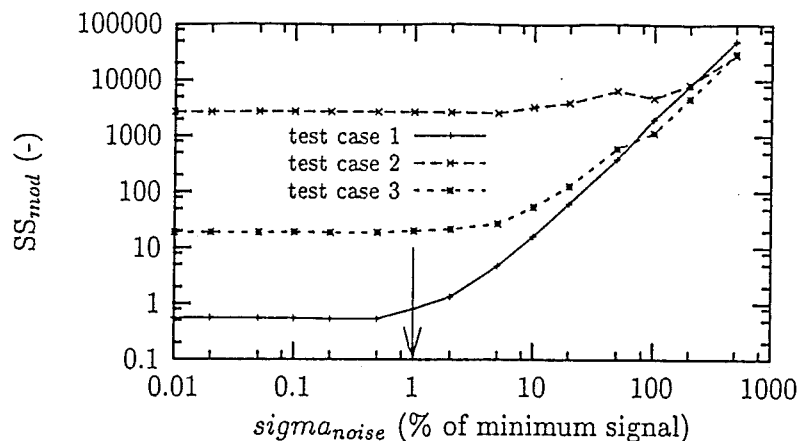
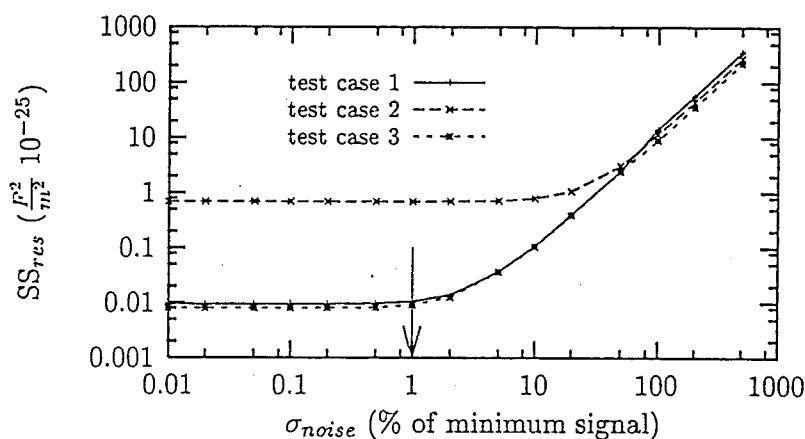
(a) SS<sub>mod</sub> linear ls(b) SS<sub>res</sub> linear ls

Figure 6.5:  $SS_{mod}$  (a) and  $SS_{res}$  (b) as a function of the noise level for the linear least squares solution.

### 6.5.2 Influence of noise on the linear least squares solution

Figure 6.5 shows two plots of the results obtained when adding noise to the calculated capacitances. It displays the effect of adding noise when using the linear least squares solution. Figure 6.5(a) displays the  $SS_{mod}$  as a function of noise level. Both the x-axis and y-axis are logarithmic, the x-axis containing the added noise level in terms of % of the smallest signal, the y-axis containing the calculated  $SS_{mod}$  on a logarithmic scale. For low noise levels the  $SS_{mod}$  is almost constant. At some critical noise level the  $SS_{mod}$  starts to increase rapidly. This indicates that the distance between the permittivity values estimated and the presumed permittivity values grows rapidly.

The three test cases have different sensitivities to noise, since the critical point, where the curve starts to increase, is at different noise levels for the three test cases.

The arrow indicates the noise level measured in the DUT-electronics. Only test case 1 has an increasing  $SS_{mod}$  within the noise level found by the experiments. But test case 1 has also the lowest  $SS_{mod}$ , which indicates that the core-flow has the best reconstruction in comparison with the other two test cases. This is trivial, since this test-case contains a large degree of symmetry.

From Figure 6.5b, we can conclude that the  $SS_{res}$  and the  $SS_{mod}$  behave similarly. For low noise levels the  $SS_{res}$  is constant, until some critical point when the  $SS_{res}$  starts to increase rapidly.

From Figures 6.5a and 6.5b we can conclude that more accurate measurements do not improve the  $SS_{mod}$  and the  $SS_{res}$  found significantly when using the linear least squares method, although a small improvement is possible. Whether this constant  $SS_{mod}$  and  $SS_{res}$  mean that the estimated permittivity vectors are the same has to be investigated yet.

### 6.5.3 Influence of noise on the constrained least squares solution

In Figure 6.6a and Figure 6.6b the  $SS_{mod}$  and  $SS_{res}$  of the constrained least squares solution are shown. First look at the differences of the value of  $SS_{mod}$  value when using the linear least squares solution (Figure 6.5a) and when using the constrained least squares solution (Figure 6.6a). The  $SS_{mod}$  for the three test cases is much lower in the case when 'a priori' knowledge is used. The  $SS_{mod}$  of test case 1 equals zero up to a noise level of 10%, which is 10 times the noise level of the UMIST and DUT electronics.

For the three test cases  $SS_{mod}$  is constant up to a noise level, higher than the noise level found in the experiments. From this we can conclude that the noise level does not have any significant influence on the reconstruction, which shows the robustness of the algorithm. Test case 3 is not well reconstructed as can be seen from the high  $SS_{mod}$  at very low noise levels. The  $SS_{mod}$  equals a value of 19, as can be read in Figure 6.6a and table 6.1. This means the sum of squared errors is very high compared to the values found in the two other test cases. Since the permittivity values estimated cannot exceed a permittivity of 2 and cannot be lower than a permittivity of 1 when using the constrained least squares method, it can be concluded that the estimated model parameters differ very much from the presumed parameters. But nevertheless the value of the  $SS_{mod}$  is not changed that much with increased noise level, so the algorithm is still consistent and finds the same solution when simulated noise is added.

In Figure 6.6b the  $SS_{res}$  is displayed. Comparing this figure with the  $SS_{mod}$ , the same trend can be seen again. First the  $SS_{res}$  is constant until some point where the  $SS_{res}$  increases rapidly. From this Figure it can be concluded that the noise level does not have any significant influence on the reconstruction up to 10 times the noise level found in the experiments, indicating the algorithm to be very robust.

On the other hand we can conclude from this simulation that the small variations in the data cannot be explained in the reconstruction pixels. Data fluctuations up to 5% of the lowest signal level can not be seen in the reconstruction. Once again the ill-conditioning of the problem arises. Small objects in the sensor will cause very small capacitance changes, especially when the objects are located in the centre of the sensor. These small variations

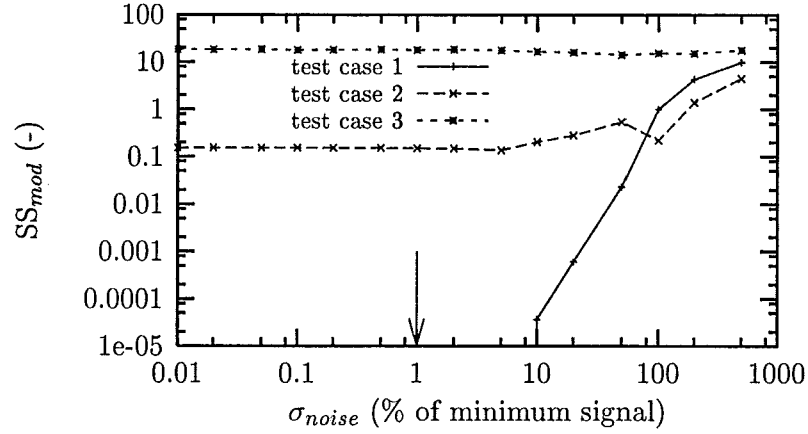
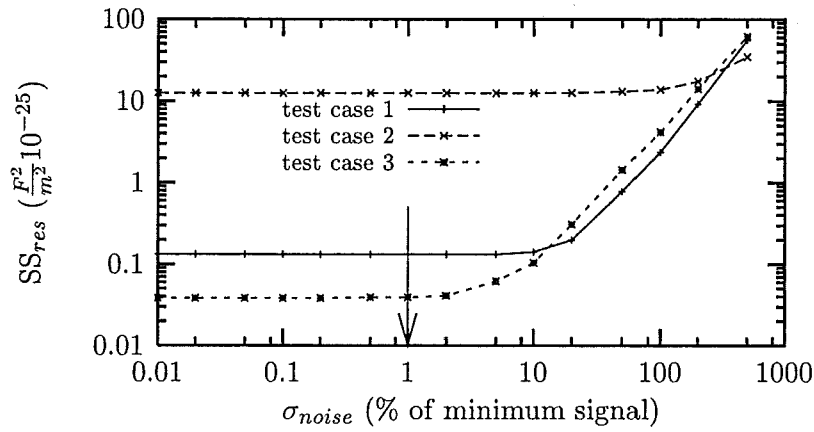
(a)  $SS_{mod}$  constrained ls(b)  $SS_{res}$  constrained ls

Figure 6.6:  $SS_{mod}$  (a) and  $SS_{res}$  (b) as a function of the noise level for the constrained least squares solution

will not change the permittivity distribution calculated and therefore these objects are not recovered in the reconstructions. It is, thus, important that the correlation between the data points is taken into account (See also chapter 8).

## 6.6 Discussion of $SS_{mod}$ and $SS_{res}$

In section 6.2.4 was stated that there is, in general, no relation between  $SS_{mod}$  and  $SS_{res}$ , since they measure two different errors. But when equation 6.3 is used without  $\epsilon_0$  and  $\mathbf{c}_0$ , equation 6.3 changes to:

$$SS_{res} = (\mathbf{c} - \mathbf{J} \cdot \boldsymbol{\epsilon}_{est})^T (\mathbf{c} - \mathbf{J} \cdot \boldsymbol{\epsilon}_{est}) \quad (6.4)$$

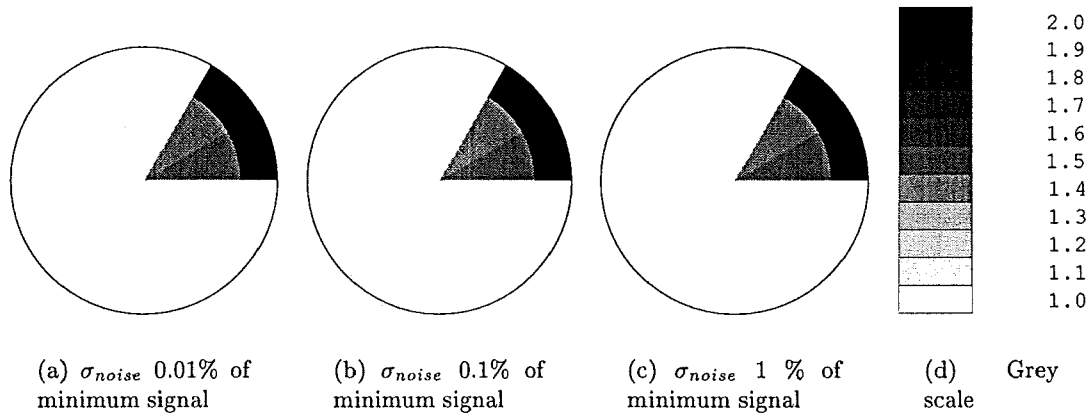


Figure 6.7: Reconstructions of test case 2, adding different noise levels in % of the minimum signal, using the constrained least squares solution.

When the estimated permittivity distribution does not change due to the added noise, the value of  $SS_{mod}$ , see equation 6.3, does not change. The capacitances calculated from the forward solution,  $\mathbf{J} \cdot \boldsymbol{\epsilon}_{est}$ , do not change either. The  $SS_{res}$  depends in this case only on the absolute noise level added. When the permittivity values estimated start to change, the  $SS_{res}$  will generally increase more rapidly. Since, then not only the noise added, but also the permittivity values estimated change the  $SS_{res}$ .

On the contrary, when  $SS_{mod}$  does not change and  $SS_{res}$  does not change much, it does not indicate that the estimated parameter vector  $\boldsymbol{\epsilon}_{est}$  is not changed, as well.

By inspection of the estimated permittivity vectors for different noise levels, it can be seen whether the estimated parameter vectors  $\boldsymbol{\epsilon}_{est}$  are identical. And if so, it can be concluded that, if the model used for reconstruction is accurate enough, the  $SS_{res}$  could give an indication of the quality of the reconstruction. Figure 6.7 shows the reconstruction of test case 2 using the constrained least squares method. Only three reconstructions for three different added noise levels are displayed here. The reconstructions for all added noise levels can be found in Appendix A. At first sight, the reconstructions do not differ from each other. Only the permittivity values of pixel one and pixel two change when increasing the added noise level from  $\sigma_{noise}=0.1\%$  to  $\sigma_{noise}=1\%$  of the minimum signal. Figure 6.8 illustrates the changes in the permittivity values of pixel one and pixel two (see Figure 3.9). From Figure 6.8 can be concluded that the estimated permittivity vector  $\boldsymbol{\epsilon}_{est}$  does not significantly change for  $\sigma_{noise} < 10\%$ .

## 6.7 Conclusions

This chapter demonstrates that noise influences the reconstructions. Increasing the noise level will increase the errors in the parameters estimated. But it is demonstrated as well, that the noise level has to reach a certain value above which the influence on the parameters estimated becomes significant. With the linear least squares method this value is reached for a lower noise level than with the constrained least squares method. This

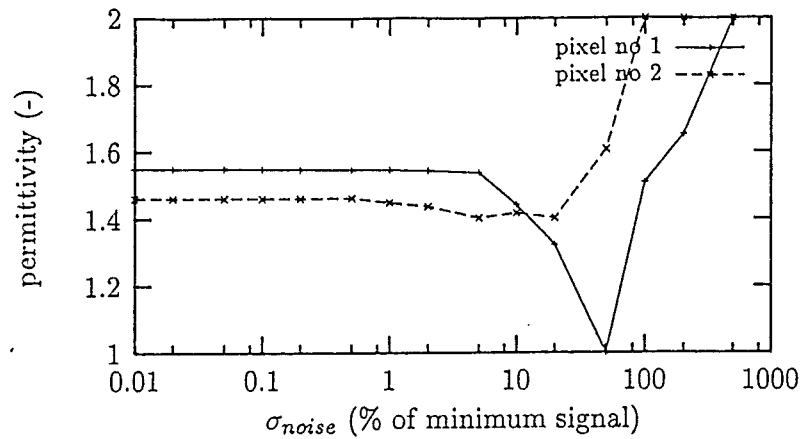
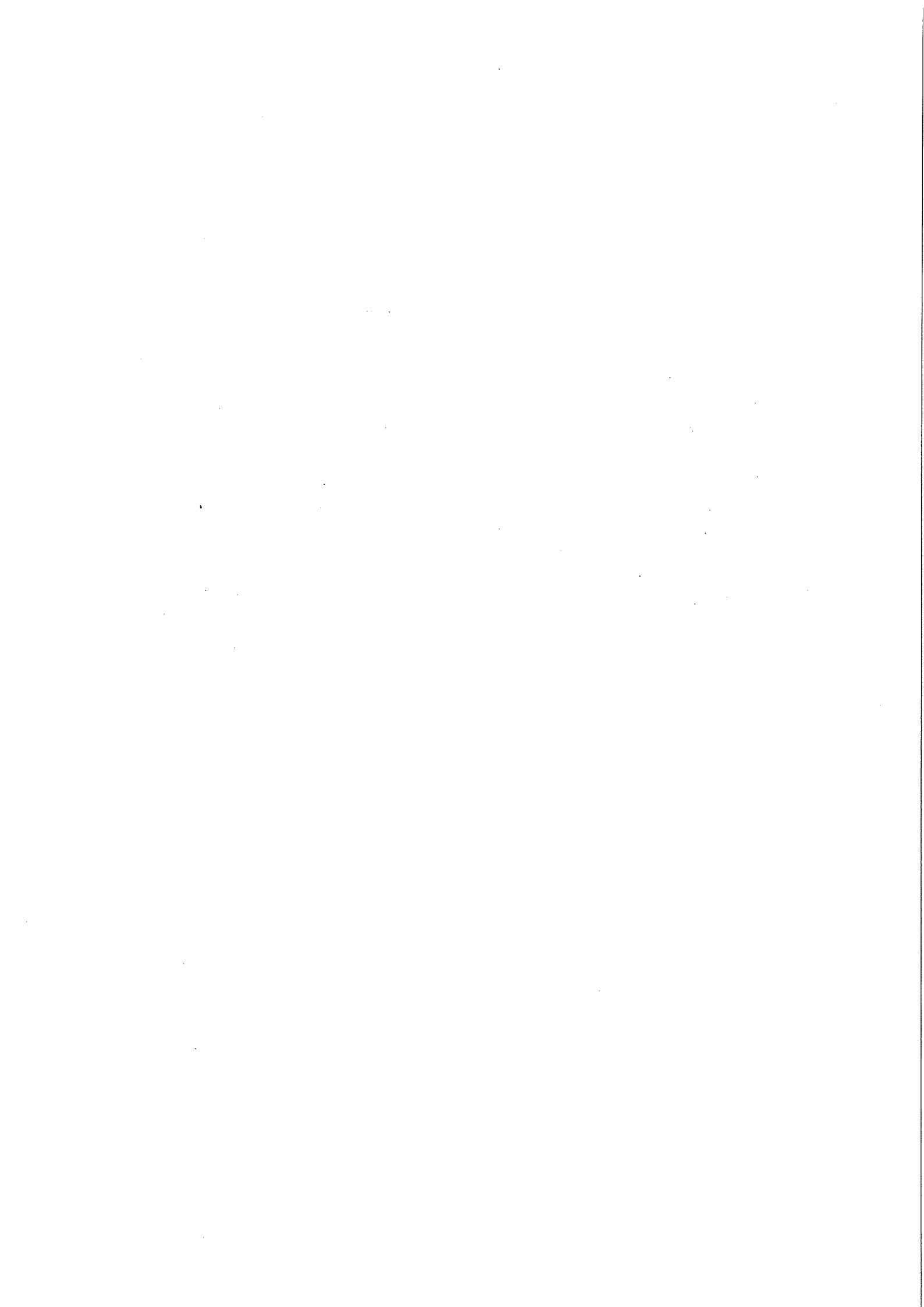


Figure 6.8: Example of the permittivity values of pixel 1 and pixel 2 as a function of the noise level for the constrained least squares solution of test case 2

indicates that the linear least squares solution is much more sensitive to small errors than the constrained least squares solution. Since the constrained least squares method finds the parameters within the physical correct interval, this is the physically acceptable solution. The algorithms are robust, as is concluded from the same values of  $SS_{mod}$  found when a noise level, up to ten times of the noise levels in experiments, is added. From these simulations we can conclude that the constrained least squares method is the most robust one.

The more constraints are added, the more robust the algorithm becomes. This is due to a reduction of its degrees of freedom.



## Chapter 7

# Reconstructions with least squares based methods

### 7.1 Introduction

This chapter deals with the results obtained, when real measurements are reconstructed using the *least squares based* algorithms, proposed in chapter 4. In chapter 6 the algorithms are tested for their robustness, i.e. what is the influence on the reconstruction (the solution) when a certain amount of noise is added to the exact data.

It was shown that the algorithms, especially the constrained least squares method, yielded the same solution for the three test cases (see Figure 6.2) when a noise level of 1% was added to the capacitance data as in the case when no noise was added to the capacitance data. However, when using real data, new problems arise.

### 7.2 Measurement system

Since the DUT electronics, which have been proven superior with respect to the *charge-transfer* electronics (see Chapter 5), are still in development, the capacitance measurements are performed using the UMIST-electronics. Figure 7.1 shows the three components of the measurement system.

The system consists of a *capacitance sensor* unit, a *data acquisition module* and a *personal computer* equipped with *custom communications and control* hardware. These components are described briefly in the next few subsections. For more information the reader is referred to the instruction manual of Process Tomography Ltd. [PTL, 1996].

#### 7.2.1 Capacitance sensor

The capacitance sensor unit is a custom module and can be manufactured for each individual application. The arrangement consists of a perspex pipe ( $\epsilon_r = 2$ ) surrounded by 12 equally-spaced screened electrodes. The electrodes are manufactured by gluing rectangular pieces of self-adhesive  $76\mu\text{m}$  copper foil to the outer wall. The electrodes are put on the

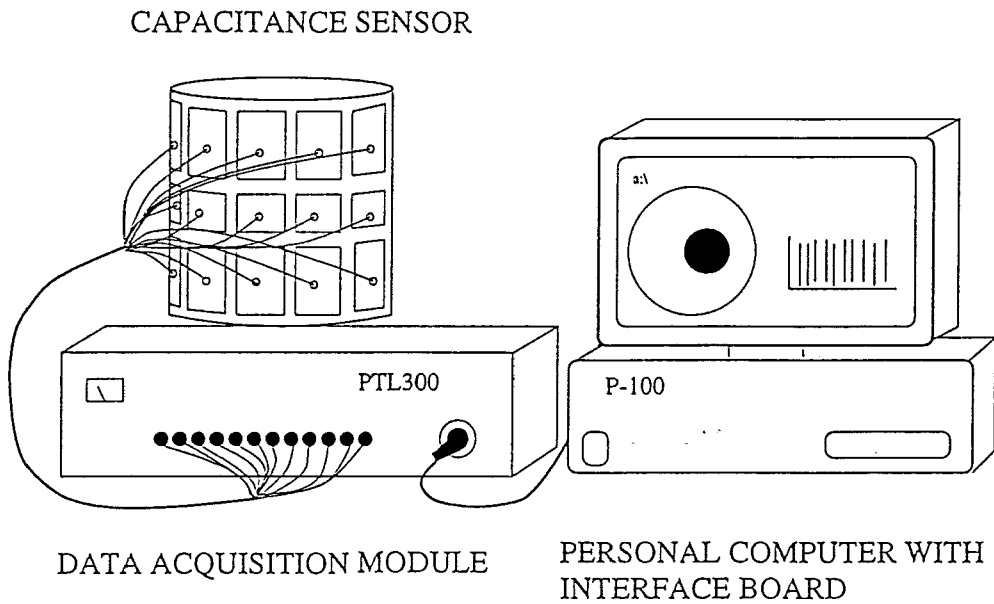


*Figure 7.1: Electrical capacitance tomography system used to perform capacitance measurements and test the inverse algorithms.*

*Table 7.1: Geometry parameters of the sensors used for the noise measurements*

sensor	the three sensors at the DUT		
	R1	R2	R3
sensor 1	$4.9 \cdot 10^{-2}$	$5.2 \cdot 10^{-2}$	$6.1 \cdot 10^{-2}$
sensor 2	$14.2 \cdot 10^{-2}$	$15.0 \cdot 10^{-2}$	$16.7 \cdot 10^{-2}$
sensor 3	$19.2 \cdot 10^{-2}$	$20.1 \cdot 10^{-2}$	$21.6 \cdot 10^{-2}$

outside of the pipe to avoid contamination of the sensor by the material inside the pipe. Under and above the measuring electrodes, axial guard electrodes are used to prevent the electric field from bending in axial direction (see also chapter 2).

At the Delft university of technology, three capacitance sensors have been manufactured. In Table 7.1 their geometries are given. The radii refer to the the geometry given in Figure 5.4a. The outer shield electrodes have been manufactured by bending four copper or brass plates, two for the upper half and two for the lower half of the sensor. They can be easily removed to check the connections of the electrodes to the coaxial leads.

To prevent static charge building up on the sensor electrodes, the sensor electrodes and the guard driven electrodes are connected to earth using discharge resistors of  $1 \text{ M}\Omega$ . This prevents damage to the CMOS input circuitry when the charged electrodes are connected to the data acquisition module.

### 7.2.2 Data acquisition module

The electrodes of the capacitance sensor are connected to the data acquisition module, the DAM200, by screened flexible coaxial leads. The technique used in the DAM200 unit is a development of the charge-transfer principle, operating at a switching frequency of 1.25 MHz.

The data acquisition module is connected to the host computer system by an un-screened twin twisted pair cable. All adjustments of the data acquisition module are made from within the system software. These include adjustments of the circuit gain for individual capacitance measurements (see section 5.4.1), and calibration of the system (see section 7.2.4).

### 7.2.3 Computer system and software

An IBM-compatible pentium 100 MHz personal computer, containing the communications hardware, controls the data acquisition module. Process Tomography Ltd. developed the PTL PCECT-software, which runs under the *windows 3.1 operating system*. The ECT system is controlled directly by the software. This software contains also an online reconstruction function, based on the *Linear back projection*. However it is also possible to collect only the measured capacitance data, giving the possibility to test the algorithms proposed in Chapter 4.

### 7.2.4 Calibration

Before capacitance measurements can be performed, the data acquisition module has to be calibrated. This is due to the limited dynamic range of the capacitance measuring circuit. This calibration involves carrying out a sequence of measurements to determine the capacitance values between each combination of electrodes  $i$  and  $j$ ,  $C_{ij}$ , for the cases the sensor is filled with the lower permittivity component or the sensor is filled with the higher permittivity component.

From the calibration data, the range of capacitance measurements for each electrode combination is known, and the capacitance measurements are normalised in a range from zero to unity for each inter-electrode capacitance measurement as follows:

$$C_{ij}^{norm} = \frac{C_{meas} - C_{\epsilon_1}}{C_{\epsilon_2} - C_{\epsilon_1}} \quad (7.1)$$

where  $\epsilon_1$  and  $\epsilon_2$  refer to the case when the pipe is totally filled with the lower and higher permittivity component respectively.

## 7.3 Measurements

### 7.3.1 The used permittivity components.

In the experiment air is chosen as the lower permittivity component. The relative permittivity of air,  $\epsilon_{air}$ , equals 1. The spacing between the outer shield and the pipe wall was

filled with air.

Polystyrene particles with a diameter of  $560\mu$  is chosen as the higher permittivity component. The relative permittivity of polystyrene,  $\epsilon_{pol}$ , equals 2.56.

Before the experiments, each sensor was calibrated to set the dynamic range of the capacitance measuring circuit. Thus, first the empty pipe capacitance data were measured and secondly the pipe was filled with the polystyrene particles resulting the full pipe capacitance data. So the PCECT system returns the normalised capacitance data (see Section 7.2.4).

### 7.3.2 The objects to be measured

To approach a 2-dimensional situation, i.e. to avoid the field lines to bend in axial direction, the object to be measured was given the same geometry in axial direction. Therefore, a rod was chosen as the object to be reconstructed.

This rod was manufactured by putting the polystyrene particles into a very thin circular case of polyethylene.

## 7.4 Reconstructions of real measurements

### 7.4.1 The 10 cm sensor

In the 10 cm sensor, experiments were performed using either one or two rods. The rods, diameter of 16 mm, were placed at well defined positions of the cross-section. First the normalised capacitances were measured and saved on the hard disk of the personal computer, connected to the system.

Secondly, the data were down loaded to a HP-Workstation and subsequently processed using the mathematical software package Matlab. Appendix B contains the scripts used for the calculations in Matlab and the c-program to convert the binary capacitance data from the UMIST-electronics into ASCII values.

### Reconstructions of one rod

One rod has been put at different radial position in the cross-section. The first position refers to the position when the rod touches the pipe-wall, exactly in the middle of an electrode. Subsequently the rod is moved to the pipe-centre along the line between two opposite electrodes, in steps of 1 cm.

In Figures 7.2 and 7.3 the phantoms and the corresponding reconstructions, using the constrained least squares method, are shown. The constrained least squares method was applied to the average of 1000 measured frames to reduce the influence of noise. From these figures can be observed that one object can be seen well in the reconstruction when it is positioned near the pipe-wall. When the object is moved toward the centre of the sensor, the reconstructions get poorer. This is also due to the chosen reconstruction mesh, containing large inner pixels and small near-wall pixels. When the object is close to the centre, the inner pixel is just partially covered, resulting in a lower permittivity value of

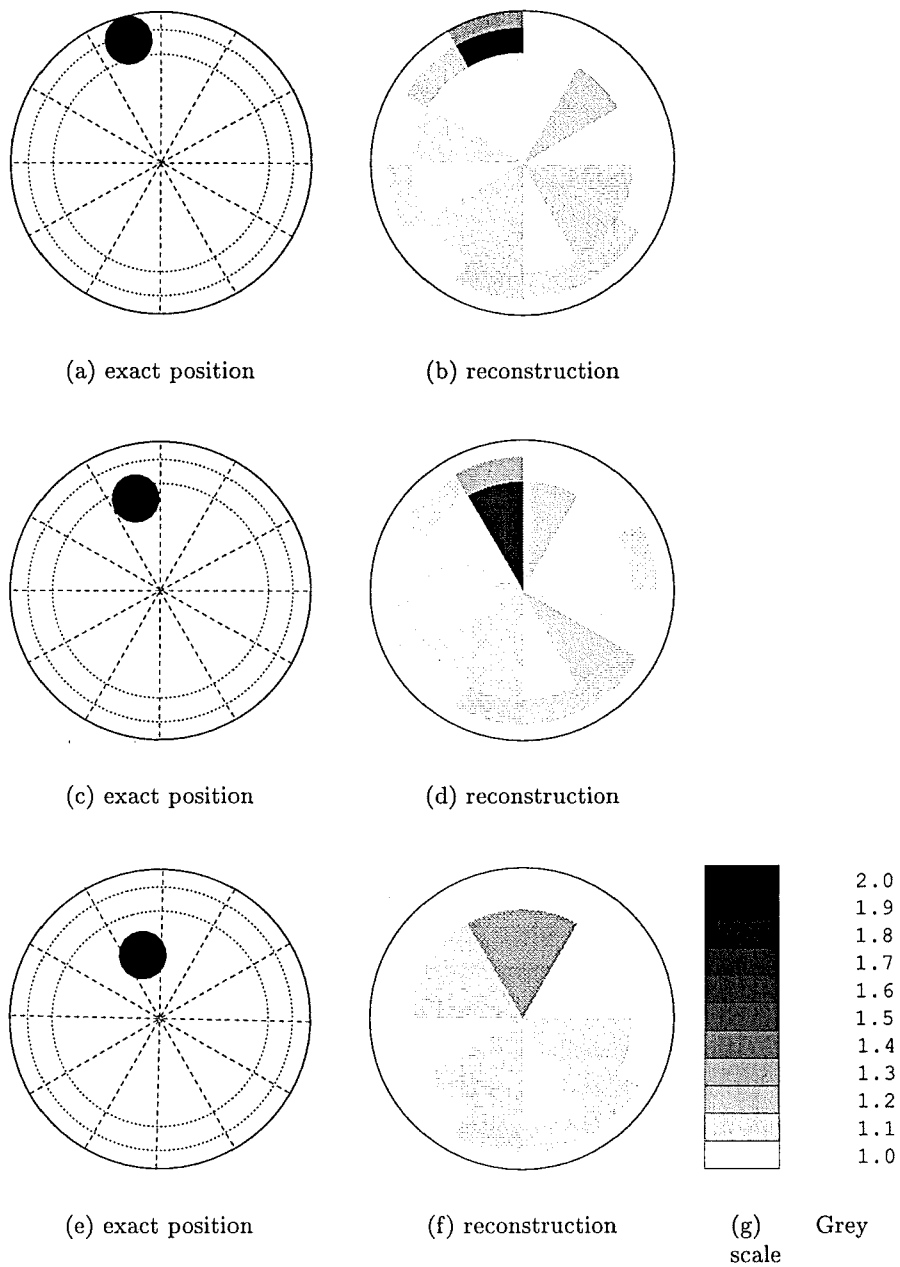


Figure 7.2: Plots of the position of a single rod in the 10 cm sensor. The exact positions are depicted in the left sub-figures (a), (c) and (e). The corresponding reconstructions using the constrained least squares method in sub-figures (b), (d) and (f)

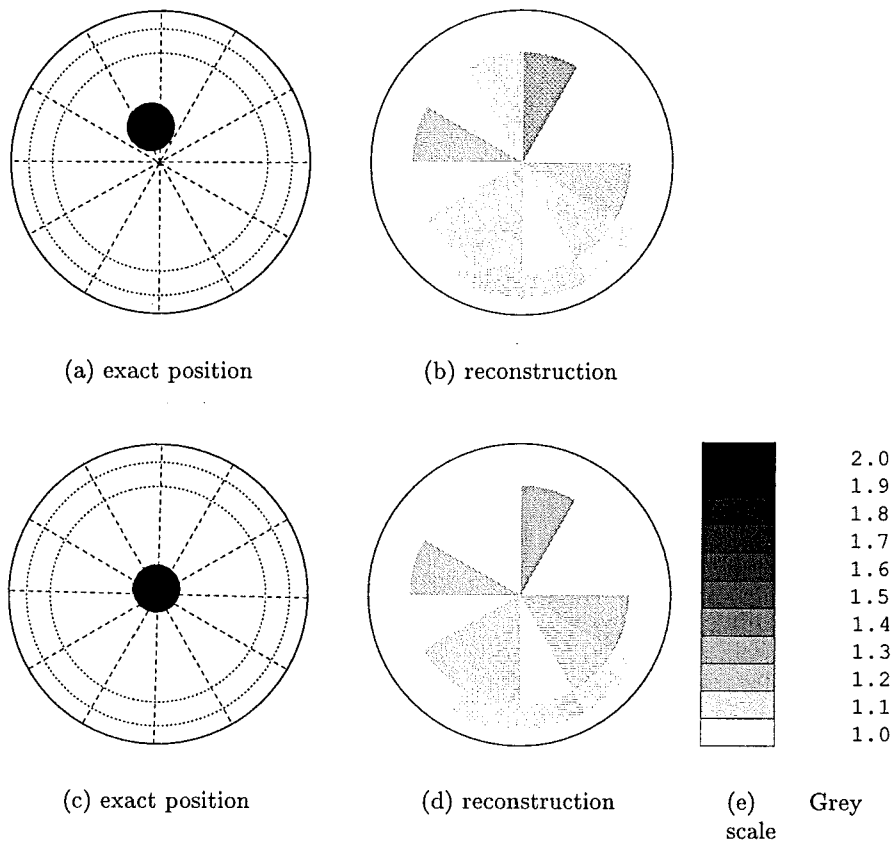


Figure 7.3: Plots of the position of a single rod in the 10 cm sensor. The exact positions are depicted in the left sub-figures (a) and (c). The corresponding reconstructions using the constrained least squares method in sub-figures (b) and (d).

the reconstruction pixel than the real permittivity value of the object.

When the object is placed in the centre, all inner pixels are partially covered. In this situation all inner pixels have to exhibit an increment of their permittivity value. From Figure 7.3d can be seen that the most inner pixels indeed have a higher permittivity value. Also, it can be observed that the inner pixels show a sort of oscillatory behaviour (also for all other reconstructions), i.e. 1 pixel high and its neighbouring pixel low. This is typical for the least squares based method, which show oscillatory behaviour in the solution due to small errors.

### Reconstructions of two rods

To check if the algorithm could distinguish two objects, also two rods are placed into the sensor, starting with one close an electrode and the other close the opposite one. These rods are subsequently moved from the pipe-wall to the centre of the sensor. In the first position both rods touch the pipe-wall, exactly in the centre of the electrodes. In the subsequent positions, the rods are moved to the centre of the pipe along the fictive line between the two rods, in steps of 1 cm.

Figure 7.4 shows the exact position of the rods and the corresponding reconstruction using the constrained least squares method. From Figure 7.4 can be concluded that two objects can be seen if they are close to the wall. When the rods are near the centre the image gets blurred, just like in the case when one rod is used.

Looking at Subfigure 7.3d and 7.4h the ill-conditioning of the inverse problem can be seen. The reconstructions look very similar, i.e. the reconstructions have almost the same pattern, only the intensity of the pixels in Figure 7.4h is a bit larger. When the presumed permittivity distribution is not known, it is very hard, even impossible, to determine if there are one or two rods in the cross-section.

Figure 7.5 shows the results obtained when one rod is at a fixed position and a second rod is moved along the wall towards the 'fixed' rod. The reconstructions of the first three positions, Figures 7.5b, d and f, show two different objects, referring to the two rods. In the last two positions, the reconstructions get worse. In those two reconstructions it is impossible to distinguish the two rods. In Figure 7.5(j) it is due to the reconstruction mesh that the two rods cannot be distinguished, since the pixels where the object is to be found are neighbours. If one assumes the objects to be circular, one could decide that both pixels contain an object. Note that when the rod is positioned so that the rod covers both neighbouring pixels half, the reconstruction will look almost the same. This effect can be seen in Figure 7.5(h), where one could decide, that originally there are three circular objects, which is evidently not the case looking at 7.5(g). However, these reconstructions show that the reconstructions of the rod near the wall are quite good. The position of the object is in most situations correct.

#### 7.4.2 The 40 cm sensor

In the third sensor, diameter 38.4 cm, a rod with a diameter of 64mm was used for the measurements and reconstructions. This rod-diameter was chosen to investigate how the sensor behaves when it is scaled up and therefore the diameter of this rod is exactly 4 times larger than the rod used in the 10 cm sensor. In position 1 the rod touches the sensor wall and in the subsequent positions the rod is moved towards the centre of the sensor in steps of 4 cm. In Figure 7.6 the positions of the phantom and the reconstructions using the constrained least squares method are shown. Comparing Figure 7.6 with the same positions of the 16 mm rod in the 10 cm sensor, Figure 7.2 and sub-figures 7.3a and 7.3b, it can be concluded that there is no significant difference in reconstruction accuracy for the 10 cm sensor and the 40 cm one. When the object is near the wall, the reconstruction is best, while closer to the centre the reconstruction gets worse, like in the 10 cm sensor. Just like in Figure 7.2, some pixels are given a too high permittivity. This is due to a mismatch between the model and the real system. The calibration of the real system appeared to be very inaccurate. Figure 7.7 shows the reconstruction of the empty pipe. In this case all the normalised capacitances have to be zero, but, as can be derived from the reconstruction, they are not equal to zero at all, indicating a strong deviation from the ideal calibration. Using this knowledge, the reconstructions of the rod in the 40 cm sensor

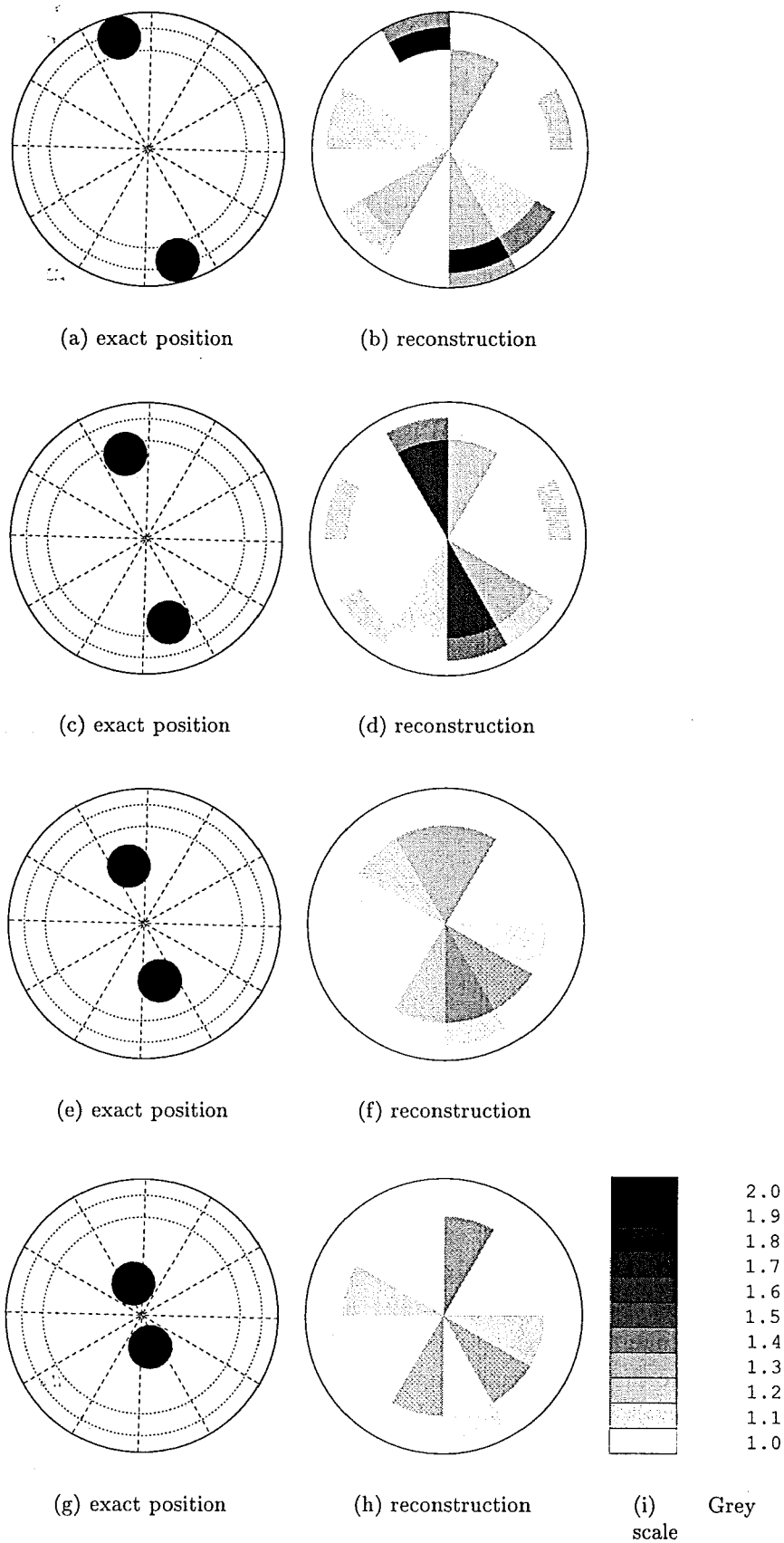


Figure 7.4: Plots of the positions of two phantoms in the 10 cm sensor. The exact positions are depicted in the left sub-figures (a), (c), (e) and (g), and their reconstructions using the constrained least squares method, (b), (d), (f) and (h).

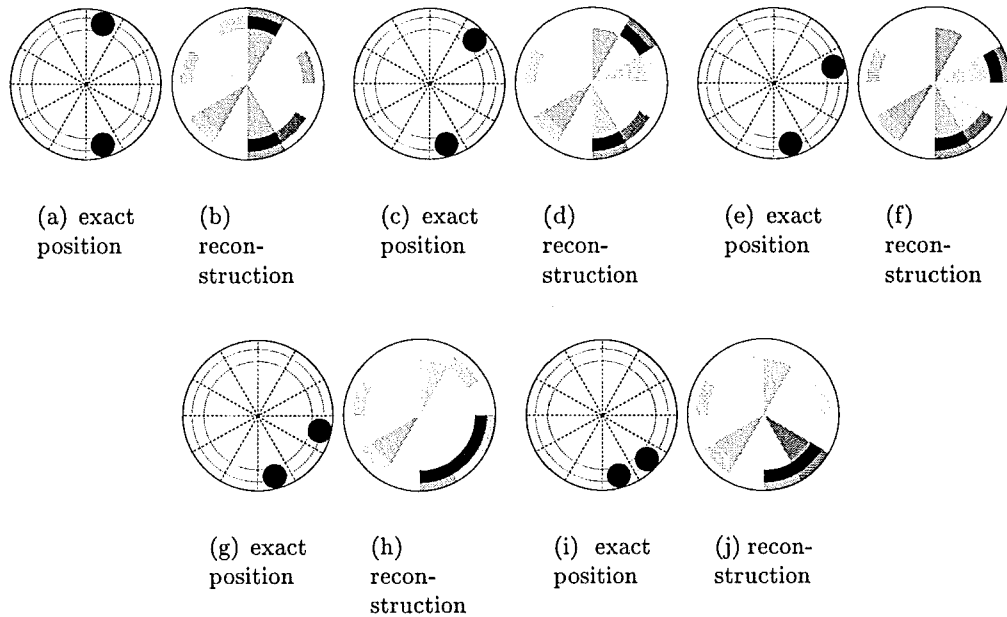


Figure 7.5: Plots of the positions of two phantoms in the 10 cm sensor. The exact positions are depicted in sub-figures (a), (c), (e), (g) and (i), and their reconstructions using the constrained least squares method, (b), (d), (f), (h) and (j).

were performed again. The empty pipe data were subtracted from the 'rod measurements', yielding a better reconstruction as can be seen from Figure 7.8. The small errors, i.e. the pixels with a too high permittivity, are reduced and therefore the reconstructions of the rod are much more accurate.

### 7.4.3 The 30 cm sensor

In the second sensor, diameter 28.4 cm, dynamic measurements were performed using a ping-pong ball, filled with the polystyrene particles. By moving the object up and down through the cross-section of the sensor, bubbles were simulated. The ping-pong ball has a diameter of 1.5 inch ( $\approx 3.81$  cm). Thus, the diameter of the 'bubble' is approximately  $\frac{1}{8}$  of the sensor diameter.

A rising bubble is simulated by pulling the ping-pong ball up through the cross-section of the 30 cm sensor. This was done for several distances of the bubble from the wall. In every measurement the bubble is pulled up perpendicular to the fictive line between the middle of electrode 12 and electrode 6 and the plane of the cross-section. The distance of the bubble from the wall is measured from the centre of the bubble to the sensor-wall. In Figure 7.9 the results are shown when the 'bubble' rises along the wall, i.e. the centre of the bubble is at 0.75 inch from the wall. On the x-axis the frame number is plotted, i.e. the discrete time. On the y-axis the normalised capacitance value is plotted.

Only the relevant values are displayed in the two plots, i.e. the electrode pair combinations with electrode 12. Figures 7.9a and 7.9b show a very clear peak between frame number 40 and 60, indicating that the bubble is passing through the cross-section. From the plot can

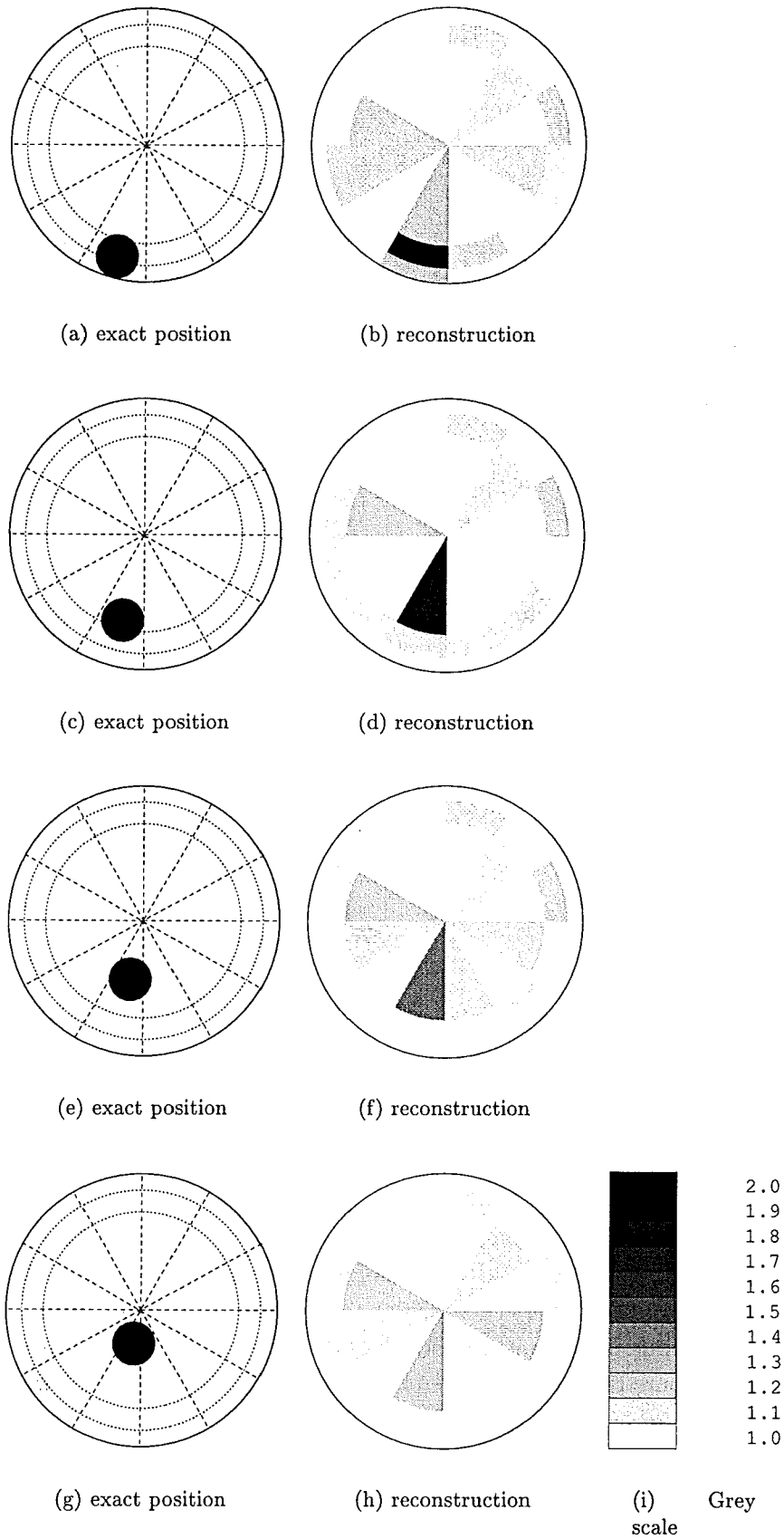
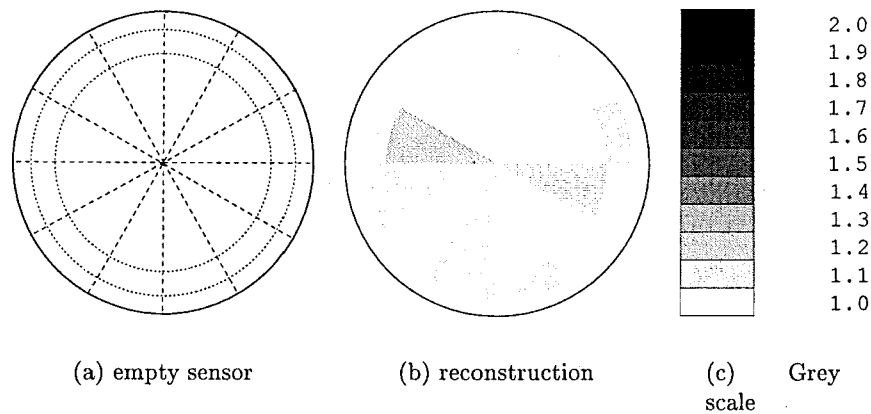


Figure 7.6: Plots of the positions of one phantom in the 40 cm sensor. The exact positions are depicted in the left sub-figures (a), (c), (e) and (g), and their reconstructions using the constrained least squares method, (b), (d), (f) and (h).



*Figure 7.7: Reconstruction of the empty pipe data. Since the calibration data are not that accurate, the reconstruction of the empty pipe data gives false estimates for some permittivity values, as can be seen from sub-figure (b).*

be concluded that a bubble of a diameter of  $\frac{1}{8}$  of the sensor diameter can be reconstructed when passing the cross-section of the sensor along its wall, since the relevant capacitance values change significantly when the bubble passes the cross-section.

Figure 7.12 shows the reconstruction just before the bubble reaches the 'measuring' section (frame 20), sub-figure (a), and the reconstruction when the bubble is in the 'measuring' cross-section (frame 52) for both the measured data, sub-figure (b), and the measured data minus the empty pipe data (frame 20), sub-figure (c).

It is clear that the significant changes in Figures 7.9a and 7.9b do not appear in the reconstructions. The changes of the normalised capacitances are not very large due to the small object compared to the pixel size and the 3D-effect (see section 2.2), which is larger due to the limited size of the object in axial direction. The Jacobian matrix is calculated for the pixel arrangement shown in Figure 3.9, and therefore small objects compared to the pixel size will have less effect on the parameter, i.e. the permittivity, to be estimated.

In Figures 7.10 and 7.11 the measurements of a rising 'bubble' are plotted for the case when the distance between the centre of the bubble and the wall (still electrode 12) is 5 cm and 10 cm respectively. Figures 7.12(f) and 7.12(i) show that the reconstruction of a bubble gets worse quickly when the bubble is closer to the centre of the sensor. The reconstruction of the bubble when the bubble is 10 cm from the wall is very bad and it will be very difficult to decide whether a bubble was detected or the fluctuation of the pixel was due to noise or an external stray field.

From these figures can, thus, be concluded that a single bubble of diameter 1.5 inch is detected in the 30 cm sensor, when it passes the cross-section near the wall, i.e. near one of the electrodes. When the bubble passes the cross-section of the 30 cm sensor at 10 cm from the wall (i.e. the electrodes) it is very hard to detect. In Figure 7.11 it can be derived from the correlation in the data that a bubble is passing, since all the capacitance values plotted show a little increment between frame 40 and 60. However, in the reconstruction these changes in the capacitance value have nearly no effect on the parameters, i.e. the permittivity values, to be estimated.

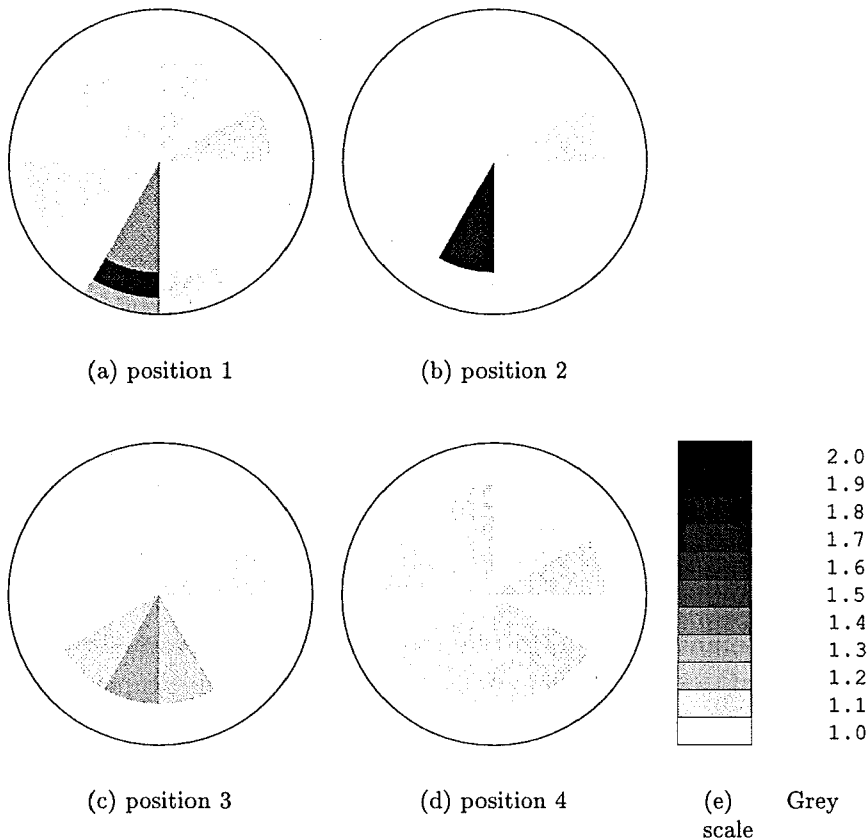


Figure 7.8: Reconstruction of the rod in the 40 cm, after subtraction of the empty pipe data. The positions refer to the

## 7.5 Reconstructions using different Jacobian matrices

From Section 4.2.3 and Appendix C it is known that the position where the Jacobian matrix is calculated matters. The Jacobian matrix is calculated by finite differences and since the slope of  $\frac{\partial C_i}{\partial \epsilon_j}$  decreases slightly when  $\epsilon$  increases, the Jacobian matrix changes when  $\Delta \epsilon_k$  is changed in the approximation  $\frac{\Delta C_i}{\Delta \epsilon_k}$ .

To investigate the effect of different Jacobian matrices, the reconstruction of the 64 mm rod when touching the wall in the 40 cm sensor was reconstructed using the constrained least squares method together with the three different Jacobian matrices. Figure 7.13 illustrates the calculation of different jacobians. In this figure the capacitance value of one electrode pair combination,  $c_i$ , is plotted against the permittivity value of one pixel,  $\epsilon_i$ , while all other pixels have a constant permittivity value,  $\epsilon_{basis}$ . From this figure, which is characteristic for the elements of the Jacobian matrix (see also Appendix C), can be seen the difference between the approximation of  $\frac{\partial C_i}{\partial \epsilon_j}$  by finite differences using different values of  $\Delta \epsilon_j$ .

In Figure 7.14 three plots are displayed when using different Jacobian matrices. The overall distribution for the three Jacobian matrices calculated, was equal to  $\epsilon_{basis} = 1.05$ . In the Jacobian matrix used for the reconstruction displayed in Figure 7.14a, the high permittivity value,  $\epsilon_{high}$ , equals 1.8 and the low permittivity value,  $\epsilon_{low}$ , equals 1, resulting

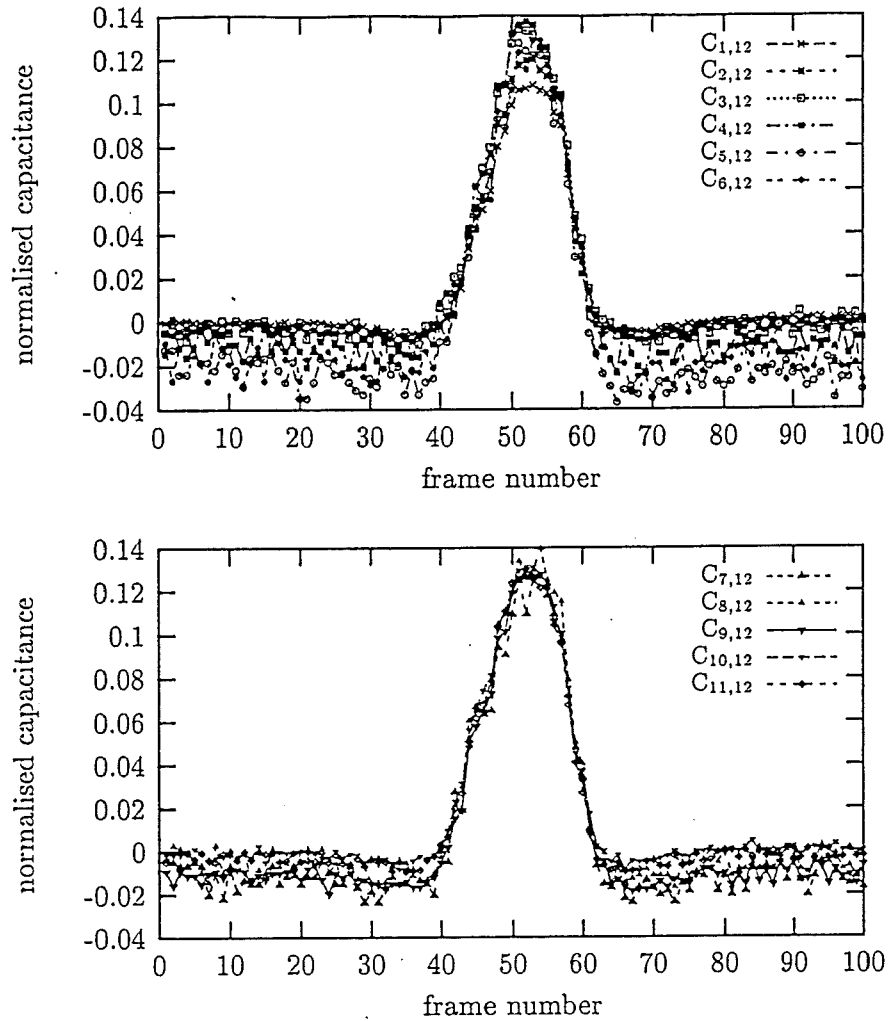


Figure 7.9: Plots of the capacitance values when a 'bubble' passes through the cross-section of the sensor. The bubble passes the middle of electrode 12 and rises along the wall.

in a  $\Delta\epsilon$  of 0.8. In Figures 7.14b and 7.14c  $\epsilon_{high}$  equals 2 and 2.2 respectively, and  $\epsilon_{low}$  equals 1 in both cases, resulting in a  $\Delta\epsilon$  of 1 and 1.2 respectively.

On the x-axis the pixel numbers, as declared in Figure 3.9, are plotted and on the y-axis the corresponding permittivity values of the pixels.

The effect of calculating the Jacobian matrix for a smaller  $\Delta\epsilon$  is that the elements of the Jacobian matrix increase and therefore changes in the capacitance data yield larger changes in the permittivity values. This effect is clearly shown in Figures 7.14(a) to (c). The peak of pixel number 21, decreases when  $\Delta\epsilon$  increases, indicating that  $\frac{\Delta C_{ij}}{\Delta \epsilon_k}$  decreases indeed when  $\Delta\epsilon$  increases. Note that the scale of the y-axis is different for the three plots. But also another effect is observed when looking at the three plots. The permittivity values of pixel number 9 and pixel number 33 increase. This is due to the constrained least squares routine in Matlab. This routine is an iterative algorithm, which adapts the Jacobian matrix after every iteration till the solution fits best in the constraints. When the highest peak is reduced, the constrained solution tries to raise the peak by adapting the Jacobian matrix, resulting in higher estimates for pixels 9 and 33 also.

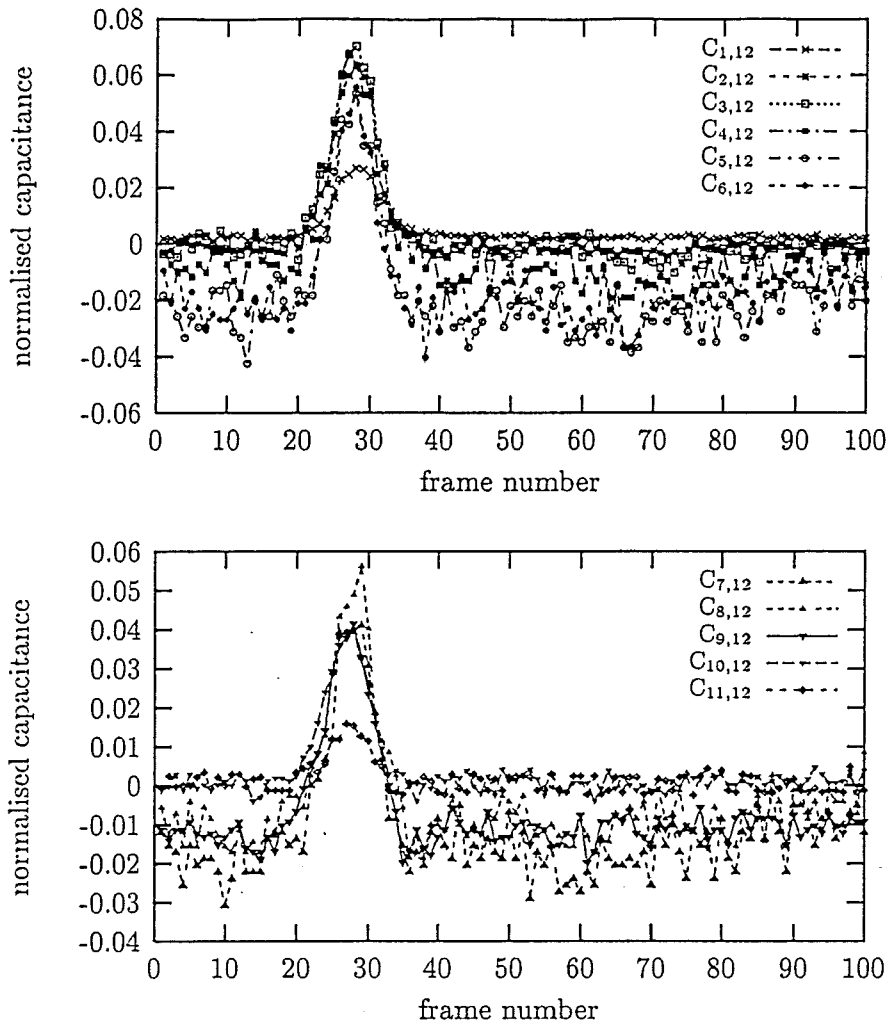


Figure 7.10: Plots of the capacitance values when a 'bubble' passes through the cross-section of the sensor. The centre of the bubble passes electrode 12 at 5 cm from the sensor wall.

## 7.6 Phillips-Towmey damping

To suppress the oscillations in the centre pixels of the reconstruction mesh, a small damping term was used to the constrained least squares solution. Linking the pixels to one another generally reduces the oscillations between neighbouring pixels. Therefore the constrained least squares solution was used together with a *Phillips-Towmey damping* to reconstruct the 64 mm rod at position 1 in the 40 cm sensor.

To link the pixels to one another the matrix  $R$  in Equation 4.19 has to be defined. This smoothing matrix  $R$  has to link the pixels in both tangential and radial direction. When using the pixel arrangement shown in Figure 3.9, matrix  $R$  is composed of  $3 \times 3$  main

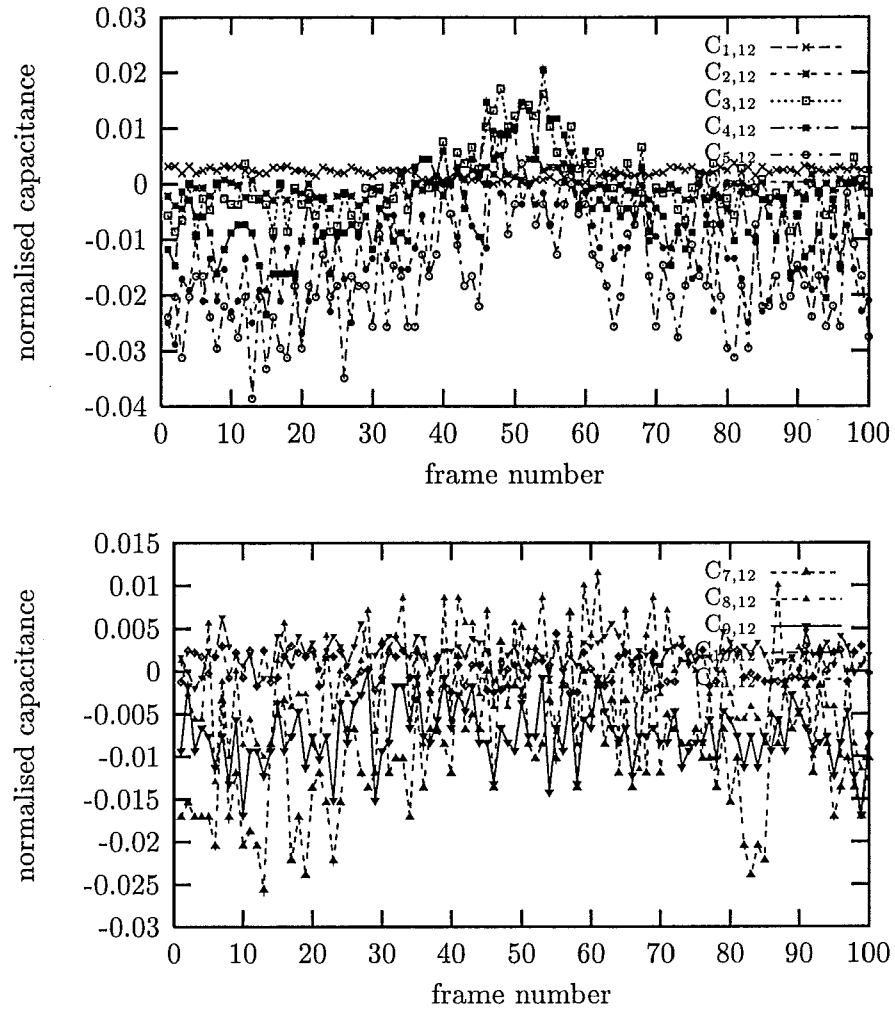


Figure 7.11: Plots of the capacitance values when a 'bubble' passes through the cross-section of the sensor. The centre of the bubble passes electrode 12 at 10cm from the sensor wall.

blocks:

$$\begin{vmatrix} A & 0 & 0 \\ C & B & C \\ 0 & 0 & A \end{vmatrix} \quad (7.2)$$

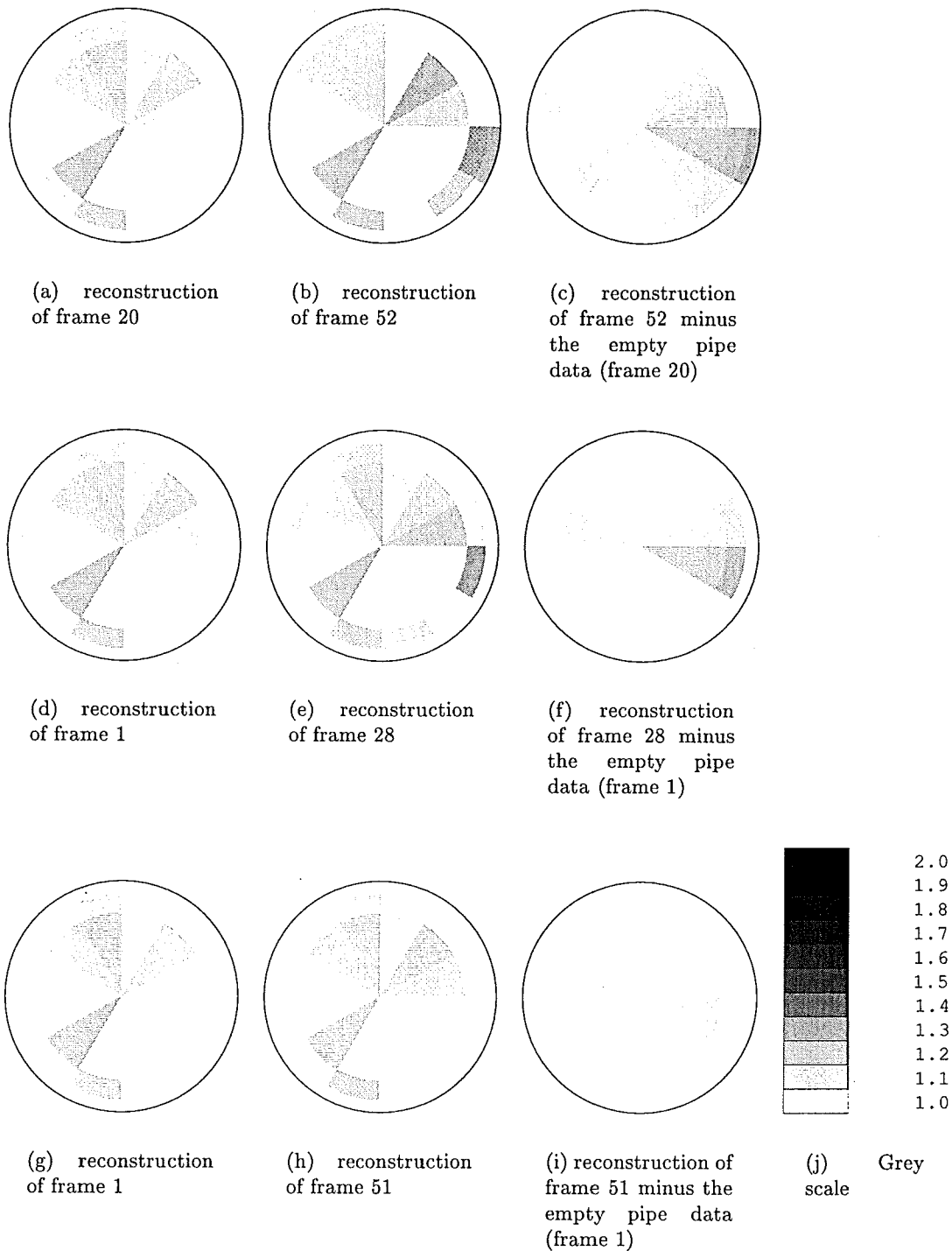


Figure 7.12: Reconstructions of a bubble rising near the wall: just before the bubble is in the 'measuring cross-section', (a), (d) and (g), when the bubble is in the 'measuring cross-section' (b), (c), (e), (f), (h) and (i). Figures (a), (b) and (c) refer to the situation when the bubble rises along the sensor wall, Figures (d), (e) and (f) to the situation when the centre of the bubble is at 5 cm from the sensor wall, and Figures (g), (h) and (i) to the situation when the centre of the bubble passes at 10 cm from the sensor wall.

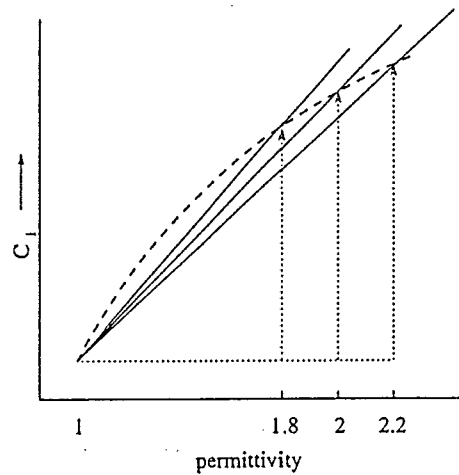


Figure 7.13: The Jacobian matrix is approximated by finite differences. In this figure the effect on the elements of the Jacobian matrix is illustrated when the derivative is calculated at different positions, i.e. for different values of  $\Delta\epsilon_j$ .

To link the pixels with its neighbours on the same ring, the blocks on the main diagonal have nonzero entries,  $C=0$ , and A and B are:

$$\begin{pmatrix} 2 & -1 & 0 & \cdots & 0 & 0 & -1 \\ -1 & 2 & -1 & \ddots & & \ddots & 0 \\ 0 & -1 & 2 & \ddots & \ddots & & 0 \\ \vdots & \ddots & \ddots & \ddots & \ddots & \ddots & \vdots \\ 0 & & \ddots & \ddots & 2 & -1 & 0 \\ 0 & \ddots & & \ddots & -1 & 2 & -1 \\ -1 & 0 & 0 & \cdots & 0 & -1 & 2 \end{pmatrix} \quad (7.3)$$

To link the pixels on the second ring to their radial neighbours on the inner and outer ring, the blocks B has to be modified as follows:

$$\begin{pmatrix} 4 & -1 & 0 & \cdots & 0 & 0 & -1 \\ -1 & 4 & -1 & \ddots & & \ddots & 0 \\ 0 & -1 & 4 & \ddots & \ddots & & 0 \\ \vdots & \ddots & \ddots & \ddots & \ddots & \ddots & \vdots \\ 0 & & \ddots & \ddots & 4 & -1 & 0 \\ 0 & \ddots & & \ddots & -1 & 4 & -1 \\ -1 & 0 & 0 & \cdots & 0 & -1 & 4 \end{pmatrix} \quad (7.4)$$

and block C is now a non-zero matrix and is filled as follows:

$$\begin{pmatrix} -1 & 0 & \cdots & 0 & -1 \\ 0 & -1 & \ddots & 0 & 0 \\ \vdots & & \ddots & & \vdots \\ 0 & 0 & & -1 & 0 \\ -1 & 0 & \cdots & 0 & -1 \end{pmatrix} \quad (7.5)$$

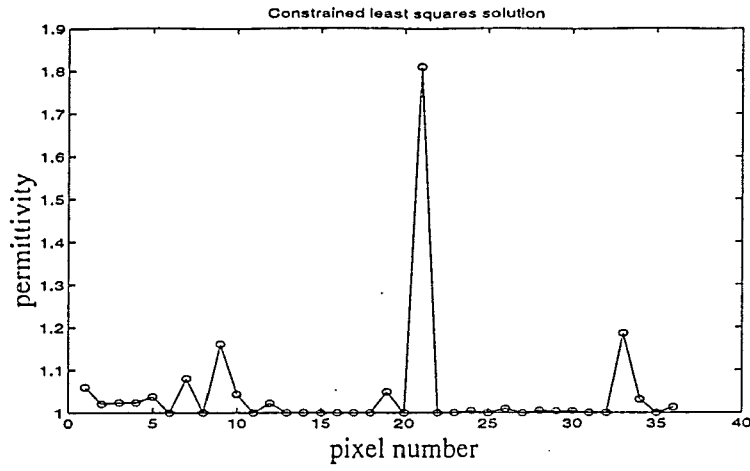
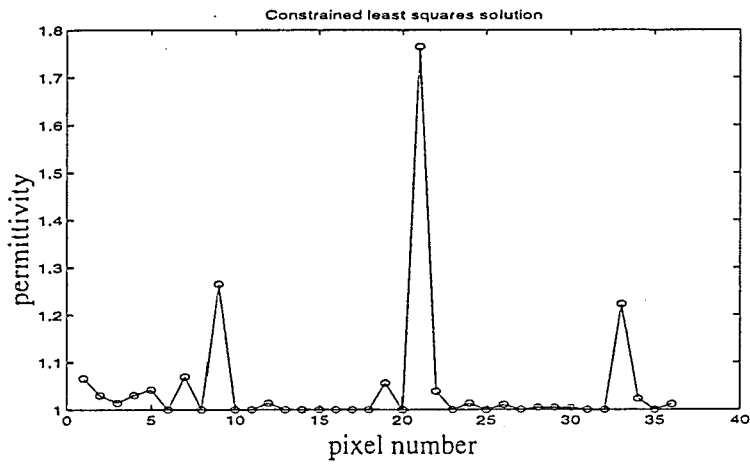
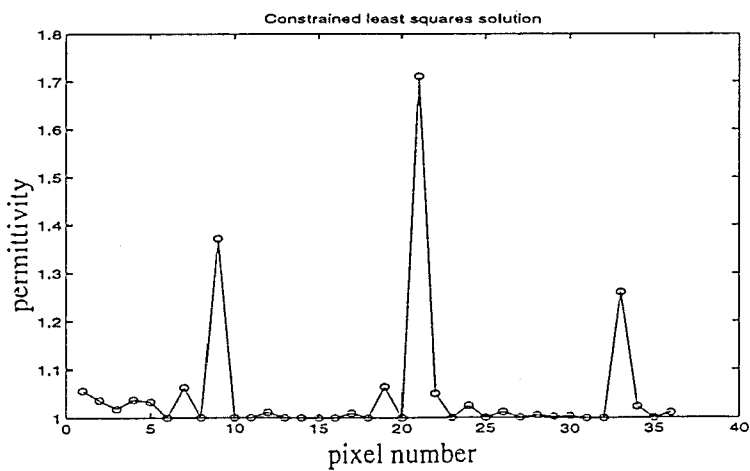
(a)  $\Delta\epsilon = 0.8$ (b)  $\Delta\epsilon = 1.0$ (c)  $\Delta\epsilon = 1.2$ 

Figure 7.14: Constrained least squares reconstructions of the 64 mm rod at position 1 in the 40 cm sensor using three different Jacobian matrices. Note that the scale of the y-axis of sub-figure (a) differs from the scale of the y-axis of sub-figures (b) and (c).

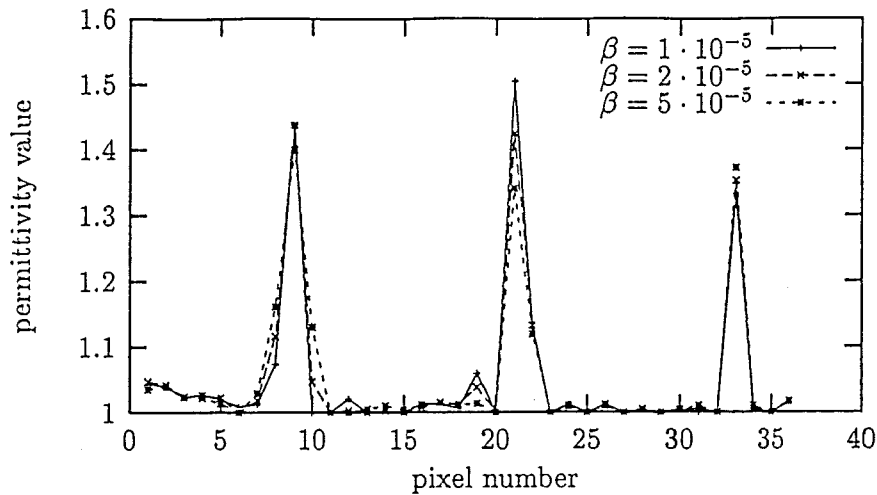


Figure 7.15: Reconstruction of a rod, diameter of 64 mm, in the 40 cm sensor, using the damped constrained least squares method. This damping is accomplished by linking the pixels to one another in radial and axial direction. The effort is to reduce the oscillatory behaviour of the centre pixels due to the underdeterminacy of those pixels.

Using this  $R$  matrix in Equation 4.19, the pixels are linked to each other as displayed in Figure 4.1b.

The degree of damping, i.e. linking, is governed by the factor  $\beta$  in Equation 4.19. A series of reconstructions was performed for a logarithmic increased value of  $\beta$ . In Figure 7.15 the reconstructions for three different values of beta are displayed. Only these reconstructions are plotted, since for these values the effect of linking is seen best. From Section 4.3.3 it is known that the value of  $\beta$  has to be found by trial and error and the best value for  $\beta$  will differ per image to be reconstructed. Figure 7.15 shows that an increasing value of  $\beta$  indeed damps the solution more and more. But this damping also reduces the permittivity value of pixel number 21, and increases the permittivity values of pixel numbers 9 and 33. Therefore a compromise between damping and goodness of the reconstruction has to be found. Since the damping of the oscillations of the inner pixels is very small in comparison with the effect of damping on the permittivity of pixel number 21, it is not recommended to use *Phillips Tournemy* damping for the reconstruction of this measurement, because valuable information is thrown away. Note that in several cases the use of *Phillips Tournemy* damping will indeed improve the reconstruction, but in general it is not recommended to use this damping term.

## 7.7 Noise in the three sensors

Section 7.4.2 shows that the reconstruction of a 16 mm rod in the 10 cm sensor and the reconstruction of a 64 mm rod in the 40 cm sensor yield comparable results. In Chapter 6 the influence of noise on the reconstruction has been tested. It has been shown that, when using the constrained least squares solution, the noise level found from the noise measurements (Chapter 5) has no influence on the reconstruction. When the system is 2-dimensional, no flux-lines bend in axial direction. This implies that when the sensor

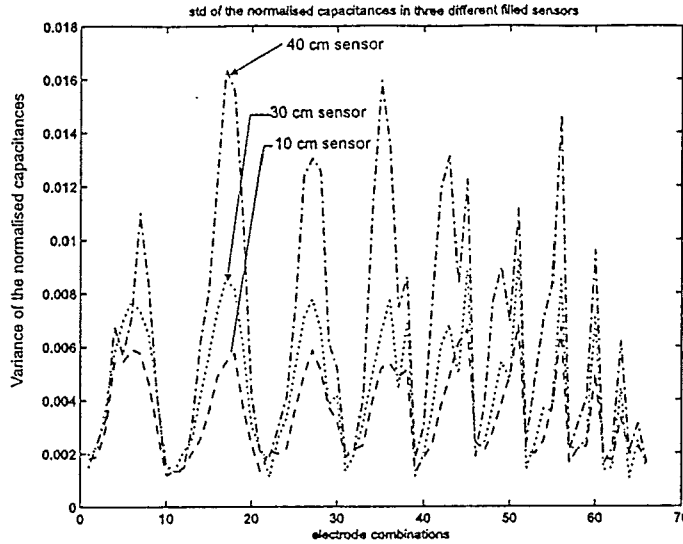


Figure 7.16: Relative standard deviation of the noise for the three sensors (10cm, 30cm and 40cm diameter, when the sensors are filled with polystyrene particles. The standard deviation was calculated from a static measurement of 1000 frames for every sensor.

is scaled up, the capacitance values will be the same. Figure 7.16 shows the standard deviation of the noise measured for the three different sensors when the sensors are filled with the higher permittivity component. In Chapter 6 was found that the absolute noise level is independent of the capacitance to be measured. In Figure 7.16 the noise levels, however, are different. Note that in this figure the relative noise level is plotted. This relative noise is defined as:

$$noise_{rel} = \frac{noise_{abs}}{C_{meas}} \quad (7.6)$$

Knowing that the absolute noise level is constant for the three sensors, the measured capacitance value has to decrease when the relative noise level increases. This is easily seen when rewriting Equation 7.6 as follows:

$$C_{meas} \cdot noise_{rel} = constant \quad (7.7)$$

From Figure 7.16 the 3-D effect, i.e. the bending of the electric field, can be observed. According to this figure the 3-D effect increases rapidly when increasing the sensor diameter. Note that bigger sensors are also more sensitive for extern influences, and therefore in Figure 7.16 also other influences may be the cause of the increased relative noise level.

## 7.8 Conclusions

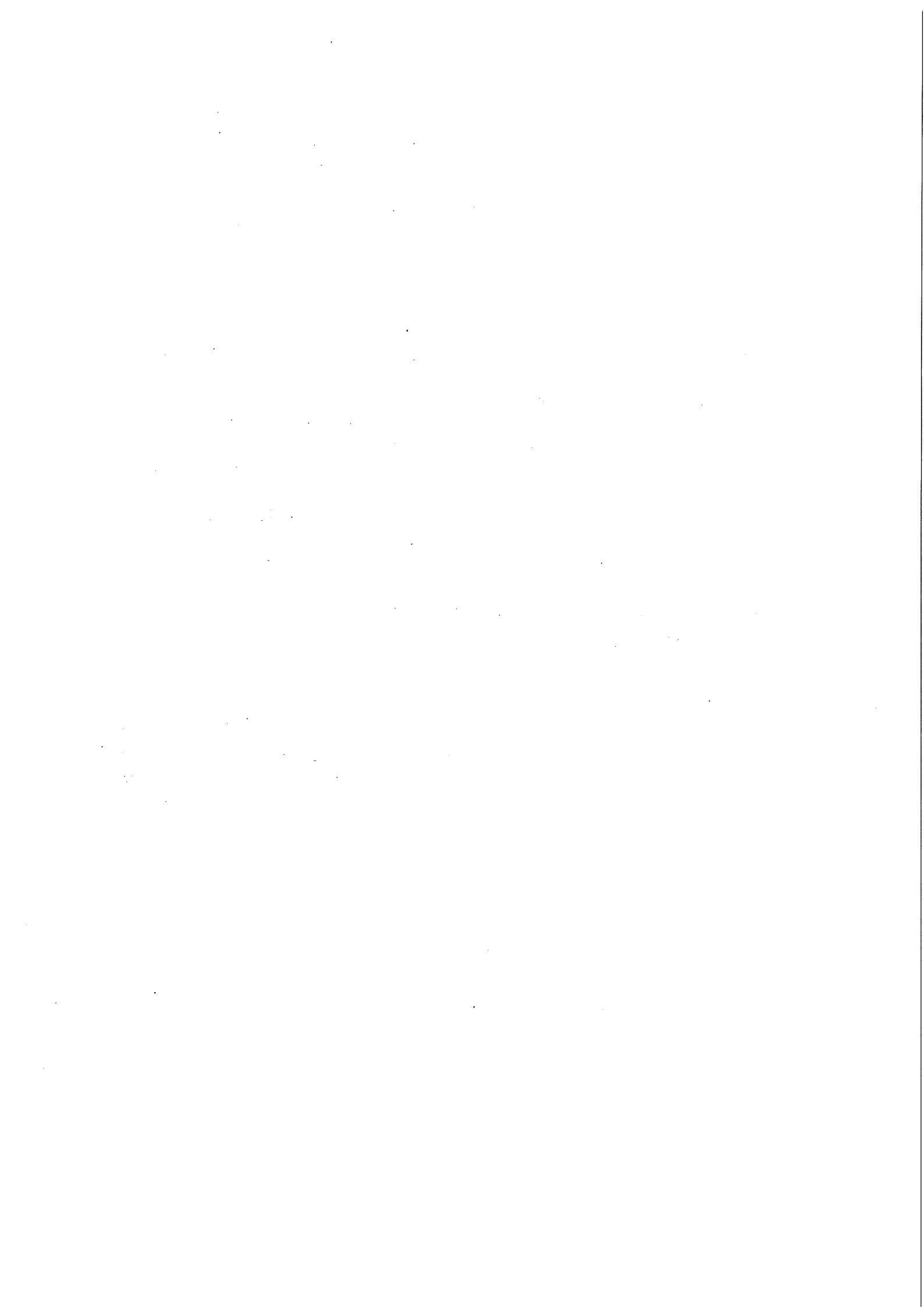
The inversion methods proposed in Chapter 4 have been tested. From reconstructions of simulated data was already concluded that the constrained least squares method yields, in general, the best results. Therefore, in this chapter only reconstructions using the constrained least squares and its hybrids have been tested. Note that the constrained least squares method is an iterative method and therefore is significantly slower than the other least squares based methods proposed in Chapter 4.

From the sections above can be concluded that reconstruction of real measurements is possible when using the constrained least squares method. The reconstruction have been proven best when the object is near the sensor wall. When the object is moved towards the centre of the sensor the reconstruction image becomes worse. This is in agreement with the results obtained in Chapter 3 and the results F.T. Kühn [Kühn, 1997] found: In the centre of the sensor the problem is under-determined and therefore the resolution in the centre of the sensor is very poor.

When using a rod, i.e. the 3D-error is suppressed, the reconstructions near the wall are very accurate and even two rods near the sensor wall can be distinguished. However, when the rods are close to the centre or when the rods are close to one another they cannot be seen separately. This is due to the pixel arrangement in the reconstruction mesh and due to mismatches between the model and the real system.

The results obtained using the 10 cm sensor and the 40 cm sensor, when the ratio between the rod and the sensor diameter was kept constant, have been found almost equivalent, although the relative noise level is higher for the 40 cm sensor due to more losses of electric flux in axial direction for bigger sensor diameters, when the axial electrode length is kept constant. This is in agreement with the results found in Chapter 6, where it was demonstrated that the measured noise level and even a 10 times higher noise level did not change the reconstruction when using the constrained least squares solution. Note that the calibration of the sensor by the PCECT-software is not very accurate either. This results in mismatches between the model and the system also. Subtraction of the empty pipe data measured from the measured data did indeed improve the reconstructions. Note that in real application this is not possible and therefore the calibration of the system has to be improved.

The bubble measurements in the 30 cm sensor showed that a rising bubble of roughly  $\frac{1}{8}$  of the sensor diameter can be reconstructed only when it is near the sensor wall. When the bubble is at 10 cm from the wall it cannot be reconstructed anymore. However, looking at the raw data from the measurement system, the bubble can be counted due to correlation in the data.



## Chapter 8

# Sensitivity of the capacitance sensor

### 8.1 Introduction

In the previous chapter, the reconstruction algorithms, proposed in Chapter 4, were tested on real data. It was shown that the least squares based reconstruction algorithms can be used as an inversion technique for the ECT problem. However, just like the linear back projection, the reconstruction gets rapidly worse, when the object is even at a small distance from the wall.

Figures 7.9 and 7.10 showed that a rising bubble could be seen in the reconstruction, when it passes the sensor near one of the electrodes. However, when a bubble of approximately 1.81 cm passes the cross-section at 10 cm from the inner sensor wall of the 30 cm sensor, the bubble is hardly seen in the reconstruction due to the very small changes in the capacitance values. From Figure 7.11 it can be seen that the bubble is indeed detected. Therefore the question arose: what is the smallest bubble that can be detected by the ECT system, especially in the centre of the sensor, since there the sensitivity is smallest.

### 8.2 Measurement setup

#### 8.2.1 Aim of the measurements

Instead of reconstruction of the measured data, in this measurements only the raw data from the *PTL data acquisition* in Figure 7.1 module have been investigated.

The aim of these measurements is to determine the smallest diameter of a 2-dimensional object at different radial position in the cross-section for the three sensors, specified in Table 7.1. Just like in the previous chapter, a 2-dimensional object is chosen for the measurements. This is done to reduce the 3-D effect in the sensors, which has been demonstrated to increase when the sensor diameter increases (see Figure 7.16).

Table 8.1: Diameters of the rods used to investigate the smallest object detectable in the capacitance sensor.

rod number	diameter (m)
rod 1	$0.9 \cdot 10^{-2}$
rod 2	$1.6 \cdot 10^{-2}$
rod 3	$2.0 \cdot 10^{-2}$
rod 4	$2.5 \cdot 10^{-2}$
rod 5	$3.3 \cdot 10^{-2}$

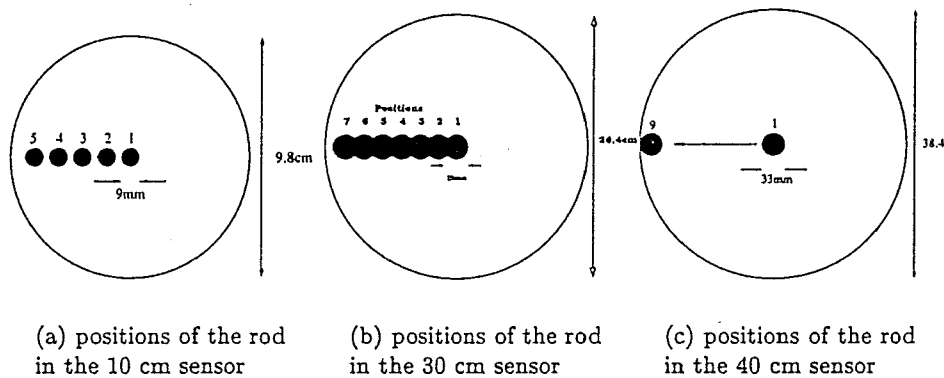


Figure 8.1: Plots of the radial positions of the different rods in the three sensors. Figure (a) the positions in the 10 cm sensor, Figure (b) the positions in the 30 cm sensor and the positions in the 40 cm sensor in Figure (c).

### 8.2.2 The phantoms

Five rods of different diameters were used, ranging from 9 mm to 33 mm. The rods were manufactured by putting polystyrene particles, diameter of  $560\mu$ , into a very thin circular case of polyethylene. In Table 8.1 the diameters of the rods are given.

## 8.3 Measurements

First the rod with smallest diameter was determined, that gave significant capacitance changes when it was moved inside the sensor, judged from the online histogram on personal computer in Figure 7.1. This rod diameter was used as the first rod to be measured.

The measurements are performed by doing static measurements of that rod at different radial positions. All measurements are averaged over 1000 frames, in order to reduce the influence of noise. Using averages over 1000 frames, small changes in the capacitance values can be detected more easily.

### 8.3.1 The 10 cm Sensor

In the 10 cm sensor the smallest rod with significant changes in the online histogram was rod number 1, the smallest rod with a diameter of 9 mm.

The rod was moved from the centre of the 10 cm sensor towards the wall, where electrode 1 is positioned, in steps of 1 cm. In 8.1a the five positions of the rod are shown. From Figure 8.2a can be concluded directly that the rod can be reconstructed when placed at position 5 and position 4, since the changes in the capacitance values are significantly higher than the relative standard deviation, plotted in Figure 8.2b. However, the normalised capacitance values for positions 1, 2 and 3 are almost the same, indicating that no distinction can be made between the 3 positions. Note that, however, there is a significant decrease of the curve for the data numbers 1 to 12, i.e. the capacitance values  $c_{1,2}$  to  $c_{1,12}$ , although the noise level is relatively high, as can be derived from Figure 8.2b.

To create a better look at the changes in the capacitance data the capacitances of the electrode pair combinations 1 and 2 to 1 and 12 are plotted in Figure 8.3. From this figure can be concluded immediately, that significant changes in capacitance value are only observed for the positions close to the sensor wall.

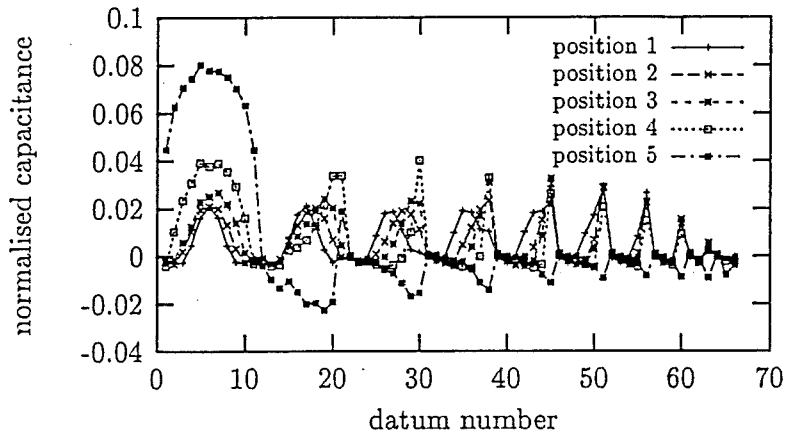
However, the 9 mm rod increased the opposite electrode capacitance 2 % with respect to the empty sensor, when it is placed at position 1, the centre of the 10 cm sensor. The standard deviation of the noise level is much lower, i.e. 0.006 from Figure 8.2b, hence the 9 mm rod is therefore estimated as the smallest detectable object.

### 8.3.2 The 30 cm Sensor

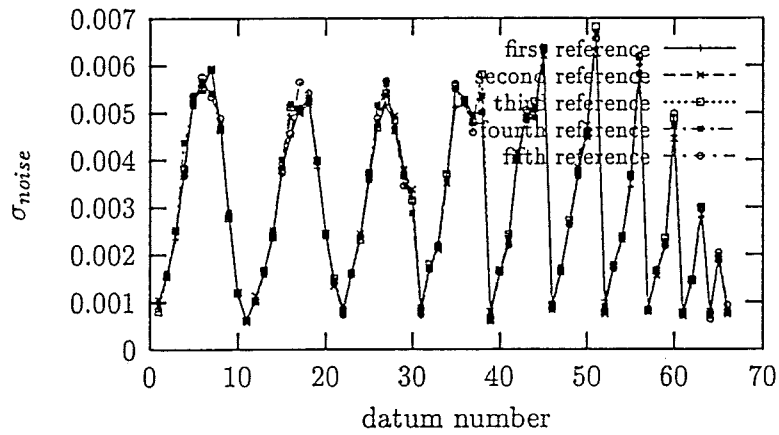
In the 30 cm sensor the rods were placed at 7 radial positions, each of them 2 cm apart from each other. In Figure 8.1b these 7 positions are shown. At position 1 the rod is positioned exactly in the centre of the sensor and in the subsequent position the rod is moved towards the wall of the sensor, where electrode 1 is positioned, in steps of 2 cm.

In the 30 cm sensor rod number 4 was found to be the smallest rod, which could be detected. In Figure 8.4 the measured capacitances are displayed, after averaging over the 1000 measured frames. Sub-figure (b) shows the standard deviation of the noise for the 7 positions. From these Figures can be observed that the rod increases the opposite electrode capacitance value 3% with respect to the empty sensor. Since the relative standard deviation of the noise,  $\sigma_{noise}$  equals about 1%, this rod can be referred to as the smallest object which can be detected in the 30 cm sensor.

In Figure 8.5 the capacitance values for the electrode pair combinations 1 and 2 to 1 and 12 are plotted. The same trend as in the 10 cm sensor can be observed: The capacitance values show almost no variation for the lower positions, i.e. when the rod is in the centre of the sensor and start changing only when the rod is near the sensor wall. This indicates that the rod is detected but the position is very difficult to define, since the subsequent positions lead to almost identical capacitance values. Here the under-determinacy of the centre of the sensor is observed again.



(a) measured capacitances



(b) standard deviation

Figure 8.2: Plots of the measured capacitances, average over 1000 frames, when a rod (diameter 9mm) is placed at different positions in the 10 cm sensor (a). The rod moves from the centre of the sensor (position 1) to the wall (position 5) with steps of 1 cm. The standard deviation of the capacitance data per position is plotted in subfigure (b).

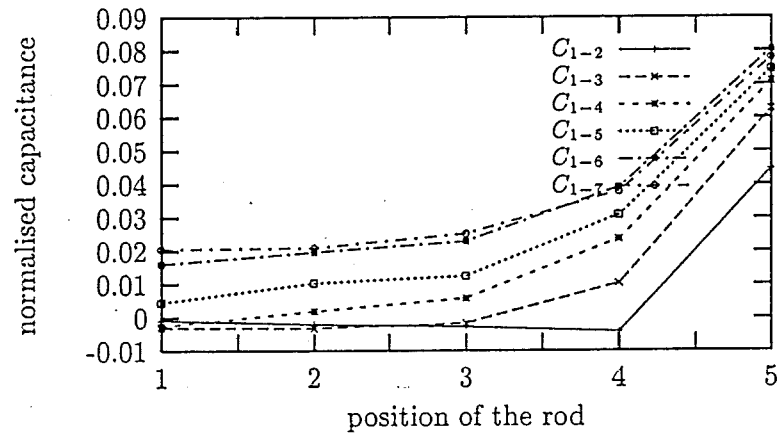
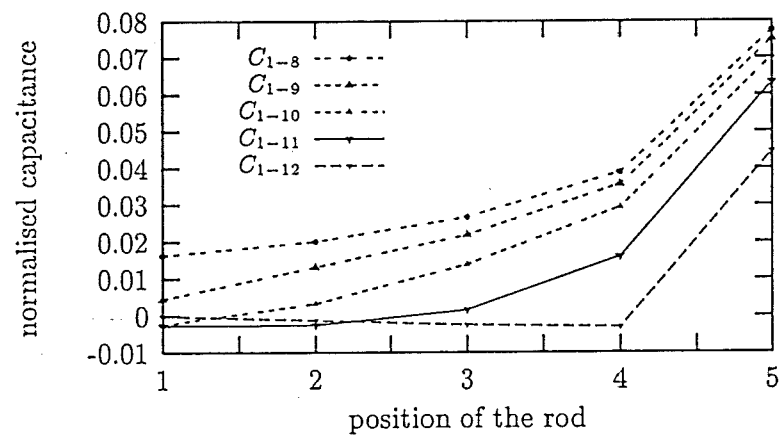
(a)  $c_{1-2}$  to  $c_{1-7}$ (b)  $c_{1-8}$  to  $c_{1-12}$ 

Figure 8.3: The measured capacitances vs the position of the rod (diameter 9mm) in the 10 cm sensor for the electrode combinations  $c_{1-2}$  to  $c_{1-12}$ .

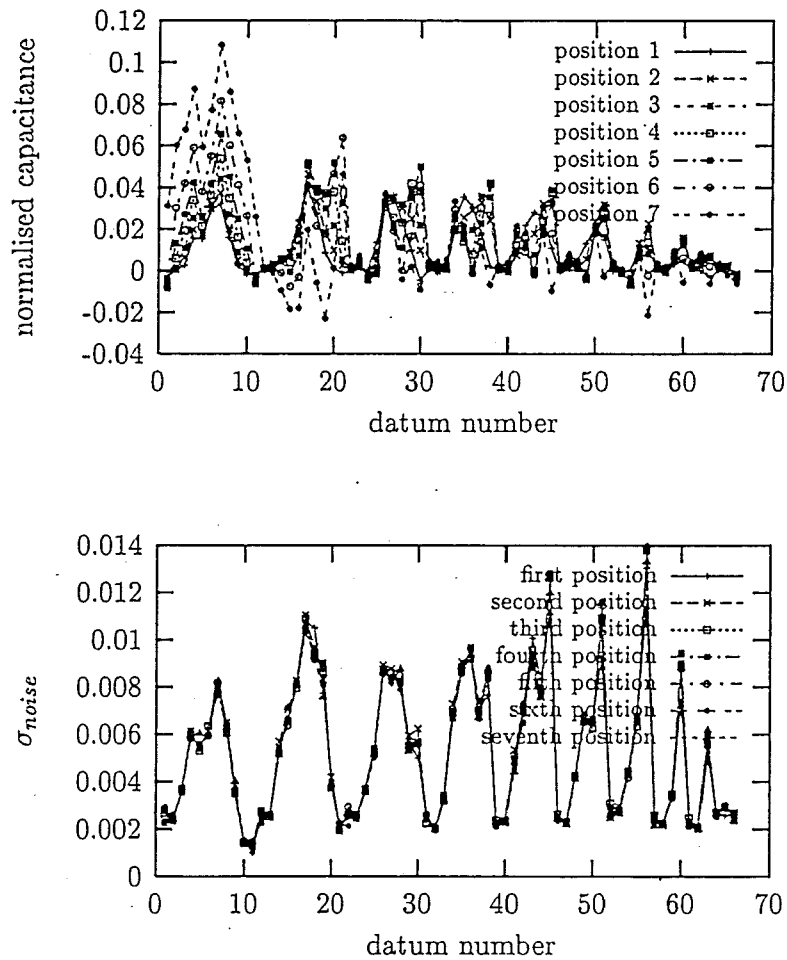


Figure 8.4: Plots of the measured capacitances, average over 1000 frames, when a rod (diameter 25mm) is placed at different radial positions in the 30 cm sensor (a). The rod moves from the centre of the sensor (position 1) to the wall (position 7) with steps of 2 cm. The standard deviation of the capacitance data per position is plotted in subfigure (b).

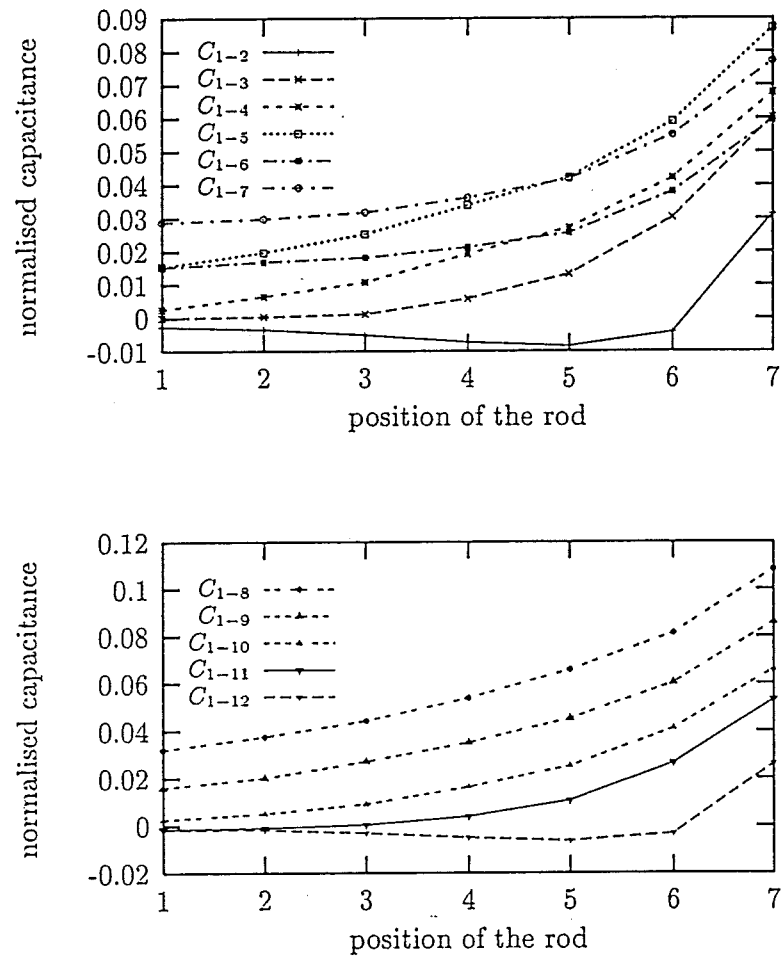


Figure 8.5: The measured capacitances vs the position of the rod (diameter 25mm) in the 30 cm sensor for the electrode combinations  $c_{1-2}$  to  $c_{1-12}$ .

Table 8.2: Diameters of the smallest rods detectable in the three capacitance sensors.

rod number	diameter (m)
10 cm sensor	$0.9 \cdot 10^{-2}$
30 cm sensor	$2.5 \cdot 10^{-2}$
40 cm sensor	$3.3 \cdot 10^{-2}$

## 8.4 The 40 cm sensor

In the 40 cm sensor the rods were placed at 9 different radial positions, which are displayed in Figure 8.1c. The first position refers to the situation when the rod is exactly in the centre of the 40 cm sensor. In the last position the rod is close to the wall near electrode 1.

For the 40 cm rod number 5 was found to be the smallest object which yielded significant changes in the capacitance data. In Figure 8.6 the capacitance data are plotted for the 9 positions of the rod. In 8.6b the relative standard deviation is plotted for the 9 positions. Just like in the 10 cm and 30 cm sensor the noise level stays the same for all positions of the rod, which is in agreement with the results found in Chapter 5.

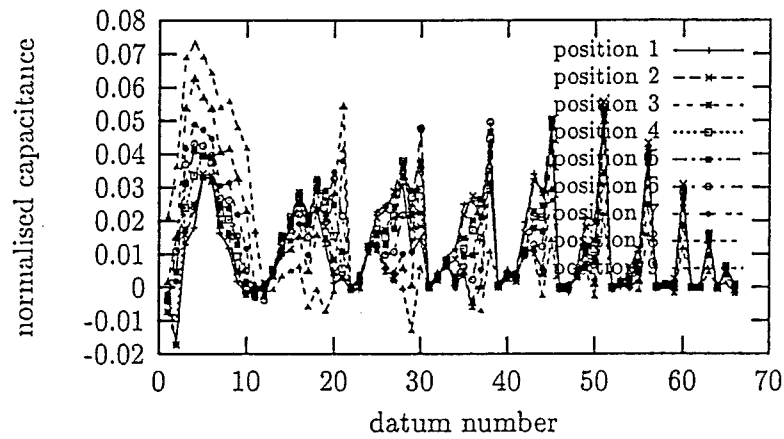
From Figure 8.6a can be seen that the rod, when placed in the centre of the sensor (position 1) yields an increment of the opposite capacitance of 3%, while the standard deviation of the noise equals about 1%.

In Figure 8.7 the capacitance values for the electrode pair combination 1 and 2 to 1 and 12 are plotted. Just like in the other sensors the rod is detected but the the positions of the rod at a small distance from the wall are almost identical, making it hard, or even impossible, to determine the exact position of the rod.

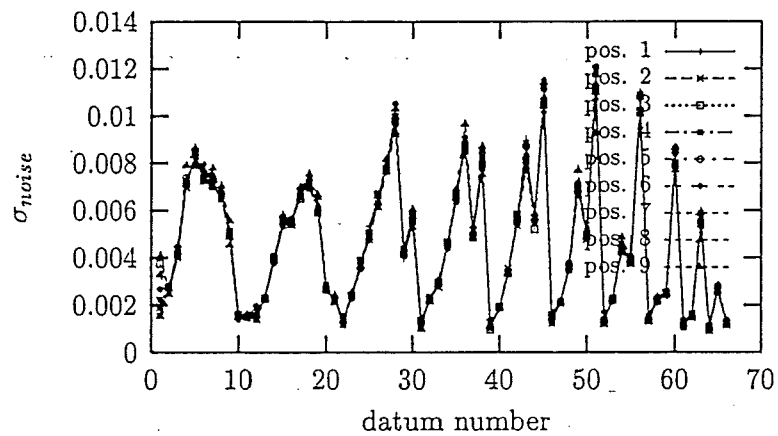
## 8.5 Conclusions

The sections above show that a small rod, as small as about  $\frac{1}{10}$  of the sensor diameter can be detected. Reconstruction, however, is very difficult or in most cases impossible, since the capacitance values are almost the same when the rod is placed in the centre of the sensor till only a few centimetres from the sensor wall. This makes the inverse problem singular, since different positions of the rod yield 'same' capacitance data. This circular centre region has a radius of about 0.6 of the sensor radius, i.e. 0.36 of the cross-sectional area.

The smallest rods to be detected by the UMIST system are given in Table 8.2. Note that a bubble is spherical and therefore has less influence on the capacitance values, due to the 3-D effect. It must be noticed that the noise levels found are significantly lower than the noise levels found in Chapter 7. This may be due to the fact that the noise measurements, displayed in Figure 7.16, were done when the sensor was filled with the polystyrene particles, which may induce an extra noise term due to possible charged particles.



(a) measured capacitances



(b) standard deviation

Figure 8.6: Plots of the measured capacitances, average over 1000 frames, when a rod (diameter 33mm) is placed at different positions in the 40 cm sensor (a). The rod moves from the centre of the sensor (position 1) to the wall (position 9) with steps of 2 cm. The standard deviation of the capacitance data per position is plotted in subfigure (b).

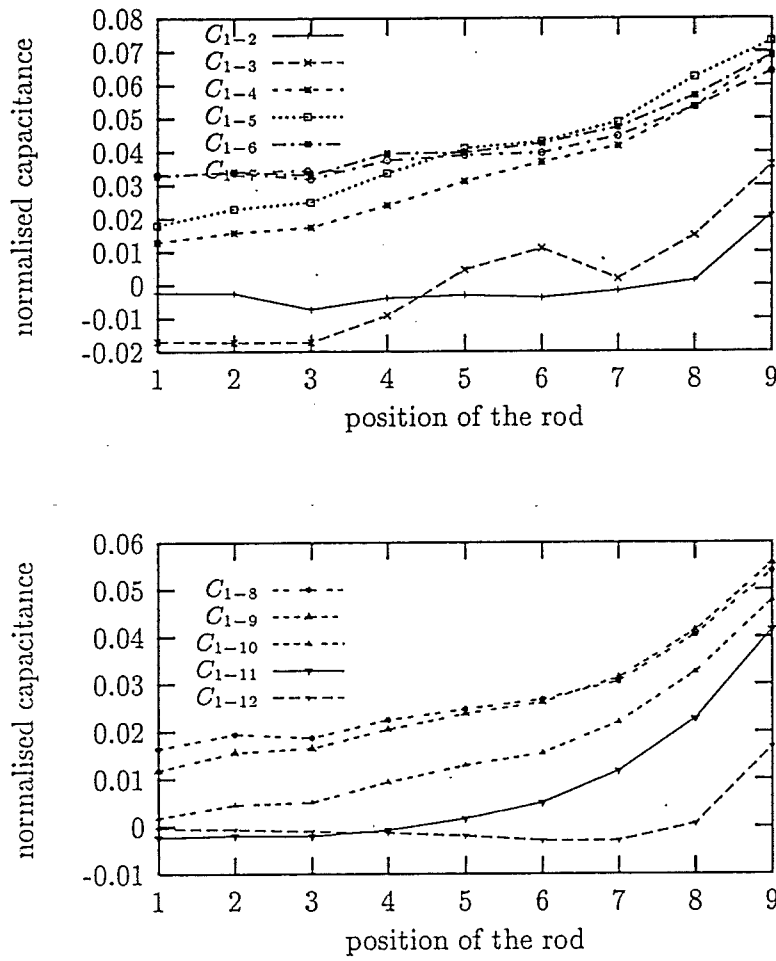


Figure 8.7: The measured capacitances vs the position of the rod (diameter 33mm) in the 40 cm sensor for the electrode combinations  $c_{1-2}$  to  $c_{1-12}$ .

# Chapter 9

## Conclusions and recommendations

*This section summarises the conclusions from the previous chapters and gives recommendations for further research*

### 9.1 Conclusions

#### 9.1.1 The simulations

##### Comparison of 12-electrode system with 16-electrode system

- The 16-electrode system provides 120 data-points and the 12-electrode system 66. However the number of principal components containing significant information is about 34 for the 16 electrode system, with respect to the 12 electrode system, which has about 28 principal components containing significant information. Thus, 54 more data-points yield about 6 more principal components carrying significant information.
- The 16 electrode system slightly improves the resolution in the middle of the pipe cross-section. There is an increase in the sensitivity of opposite electrodes measurements of about 9%. The 16 electrode system provides 8 opposite capacitance measurements instead of 6 ones by the 12 electrode system, which also could increase the sensitivity in the centre. However, only an improvement of the reconstruction is observed near the wall of the pipe, resulting in the possibility to define more near-wall pixels.

For the 12 electrode system can be noticed that the first 12 principal components have the highest explained variance, while for the 16 electrode system the first 16 electrodes show the highest variance. When the area under these first PC's for both systems is taken into account, it is clear that for the 16 electrode system almost the same amount of information is distributed among more PC's.

### The 12 electrode system using coupled source electrodes

- Using inter-connected source electrodes as additional source electrodes to obtain additional information is not recommended since this sensor concept does not improve the amount of information available. The capacitance measurements provided by the inter-connected source electrodes are merely linear combinations of the information provided by the single source electrodes.  
A 16-electrode system therefore contains also the information of a 8-electrode configuration.

#### 9.1.2 Noise measurements

- The active differentiator, developed at the Delft University of Technology, has been found superior to the charge-transfer electronics, since the new system enables very high data capture rates in comparison with the *charge-transfer* based electronics. The noise level is nearly the same for both systems when operating at maximum data acquisition speed.
- The standard deviation of the noise has a constant offset of about 0.08 fF and is independent of the capacitance to be measured.
- The accuracy of the active differentiator electronics can be reduced by averaging subsequent measurements, i.e. operating at a lower data acquisition speed. Operating at a data capture rate of 1000 frames per second, i.e. still ten times faster than the charge-transfer electronics, the relative standard deviation of the noise is reduced to 0.38 % of the minimum signal level.
- The new system avoids CMOS switches, which have an inner capacitance which is large compared to the capacitance to be measured and the system does not use coaxial cables to connect the sensor to the electronic circuit, avoiding influences on the capacitance measurements due to displacements of these cables.

#### 9.1.3 Addition of simulated noise

- Increasing the noise level will increase the errors in the parameters estimated. However, the noise level has to reach a certain value above which the influence on the parameters estimated becomes significant. With the linear least squares method this value is reached for a lower noise level than with the constrained least squares method. This indicates that the linear least squares solution is much more sensitive to small errors than the constrained least squares solution.
- Since the constrained least squares method finds the parameters within the physical correct interval and gives in general the best results, this is a physically acceptable solution.
- The more constraints are added, the more robust the algorithm becomes. This is due to a reduction of its degrees of freedom. Therefore, the simulations show that the constrained least squares method is the most robust one.

#### 9.1.4 Reconstructions

- The inversion methods proposed in Chapter 4 have been tested. From reconstructions of simulated data can be concluded that the constrained least squares method yields, in general, the best results. Note that the constrained least squares method is an iterative method and therefore is significantly slower than the other least squares based methods proposed in Chapter 4.
- The reconstructions have been proven best when the object is near the sensor wall. When the object is moved towards the centre of the sensor the reconstruction image becomes worse, since in the centre of the sensor the problem is under-determined and therefore the resolution in the centre of the sensor is very poor.
- When using a rod, so the 3D-error is suppressed, the reconstructions near the wall are very accurate and even two rods near the sensor wall can be distinguished. However, when the rods are close to the centre or when the rods are close to one another they cannot be seen separately.
- The results obtained using the 10 cm sensor and the 40 cm sensor, when the ratio between the rod and the sensor diameter was kept constant, have been found almost equivalent, although the relative noise level is higher for the 40 cm sensor due to an increasing 3-D effect for bigger sensor diameters. This is in agreement with the results found from the simulations, where it was demonstrated that the experimentally found noise level did not change the reconstruction when using the constrained least squares solution.
- The calibration of the sensor by the PC-ECT-software is not very accurate, due to problems with the electronics. These electronics contain programmable CMOS-switches to adapt the bandwidth of every channel. When the empty pipe data and full pipe data deviate from the real zeros and ones, this will result in mismatches between the model and the system.
- Since the calibration was not very accurate, also measurements were done of the empty pipe, i.e. when the pipe was filled with air only. Subtraction of the empty pipe data from the measured data improved the reconstructions. Note that in real application this is not possible and therefore the calibration of the system has to be improved.
- The bubble measurements in the 30 cm sensor showed that a rising bubble of roughly  $\frac{1}{8}$  of the sensor diameter can be only reconstructed when it is near the sensor wall. When the bubble is at a distance of  $\frac{1}{3}$  of the sensor diameter, i.e. 10cm, from the sensor wall it cannot be reconstructed anymore. However, looking at the raw data from the measurement system, the bubble can be counted due to correlation in the data.

### 9.1.5 Sensitivity of the capacitance system

- A small rod, as small as about  $\frac{1}{10}$  of the sensor diameter can be detected.
- Reconstruction of a rod placed in the centre of the sensor, however, is very difficult or in most cases impossible, since the capacitance values are almost the same for different positions in the centre of the sensor, up to only a few centimetres from the sensor wall, where the capacitances start to change rapidly. This makes the inverse problem singular, since different positions of the rod yield nearly the 'same' capacitance data.
- Note that a bubble is spherical and therefore has, due to the 3-D effect, less influence on the capacitance values and thus is harder to reconstruct.

## 9.2 Recommendations

- The calibration of the system, i.e. reference values of the empty and full sensor, has to be made more accurate, since in the centre of the pipe the capacitance value changes due to bubbles or other objects are very small. Small deviations of the reference values will therefore have large effects on the reconstructions.  
An other possibility is to omit the calibration and use a fixed dynamic range for the capacitance values. The electronics developed at the DUT use a fixed range also. A disadvantage of this fixed dynamic range is that one cannot use the measurements of neighbour electrodes, since these are a factor 100 larger than the opposite electrode measurements. However, the near wall area is over-determined already, so this does not result in much loss of information.
- In this research project, the capacitance measurements were directly (linear) coupled to the permittivity set. In Chapter 7 was shown that small bubbles are detected, but due to the very small changes in the capacitance values, very hard to reconstruct. Using the covariances between the different measurements, the reconstructions might be improved.
- To improve the sensitivity in the cross-section of the pipe, floating idle electrodes can be used. The potential gradient between these idle floating electrodes will be lower than in the old situation, yielding a higher sensitivity between the source electrode and the detecting one.
- The use of neural nets has been implemented for many problems with great success. For the ECT-inverse problem a neural net would be a good alternative, since the calculation speed and power of computers increases very rapidly. Simulations can be performed to test such a neural network. However, for practical applications the measurements have to be more accurate than the existing electronics for ECT. The simulations can be used to determine how accurate these new electronics have to be for existing ECT-system, and if this accuracy can be satisfied using the existing sensors.

Also a neural net has advantages with respect to the linear least squares based

method, since it can be trained easily using real measurements. The linear least squares methods used in this research, used a Jacobian matrix which was calculated with the FEM package SEPRAN, and therefore matches less accurate to the real measurements.



# Appendix A

# Appendix A

In Figures A.1 and A.2 the reconstructions for all noise levels added to test case 2.

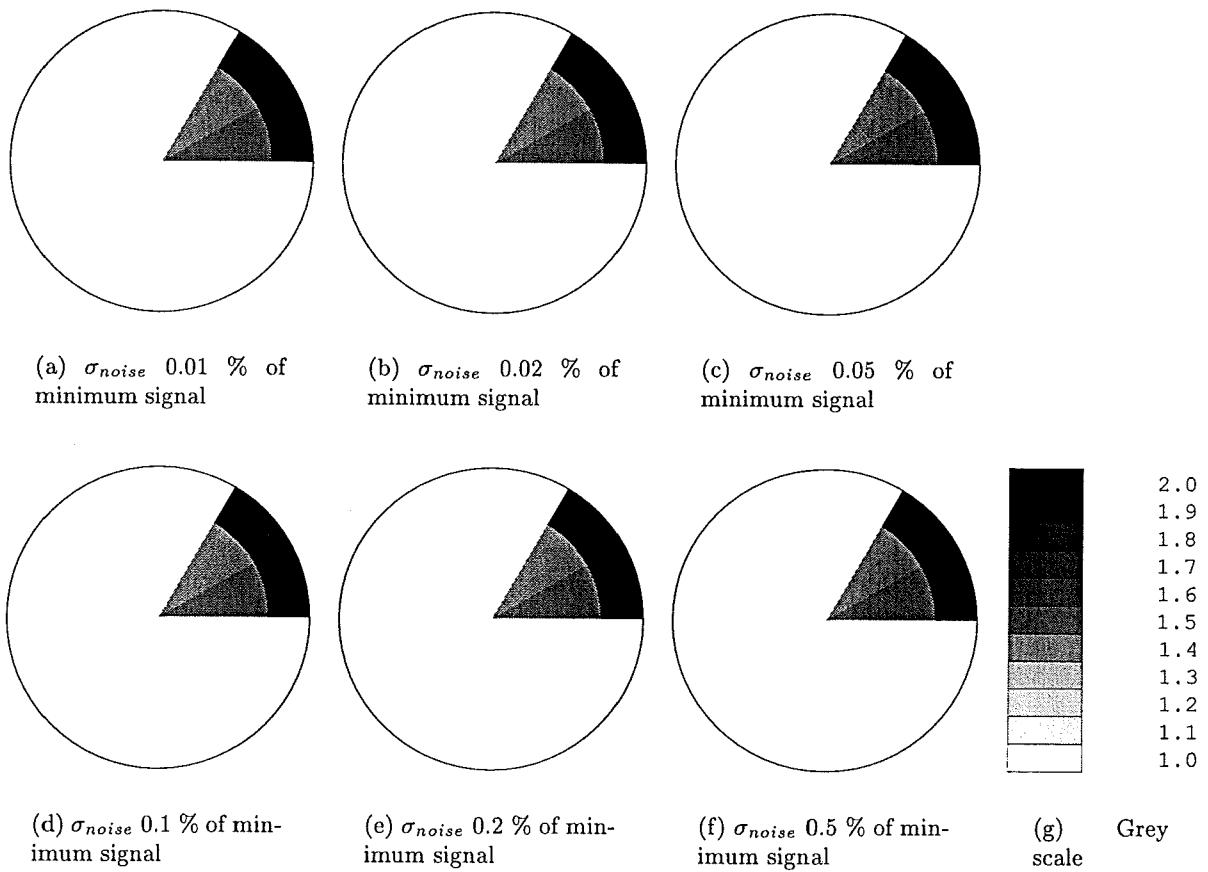


Figure A.1: Plots of the reconstructed distributions using the constrained least squares method for the first 6 noise levels added to test case 2

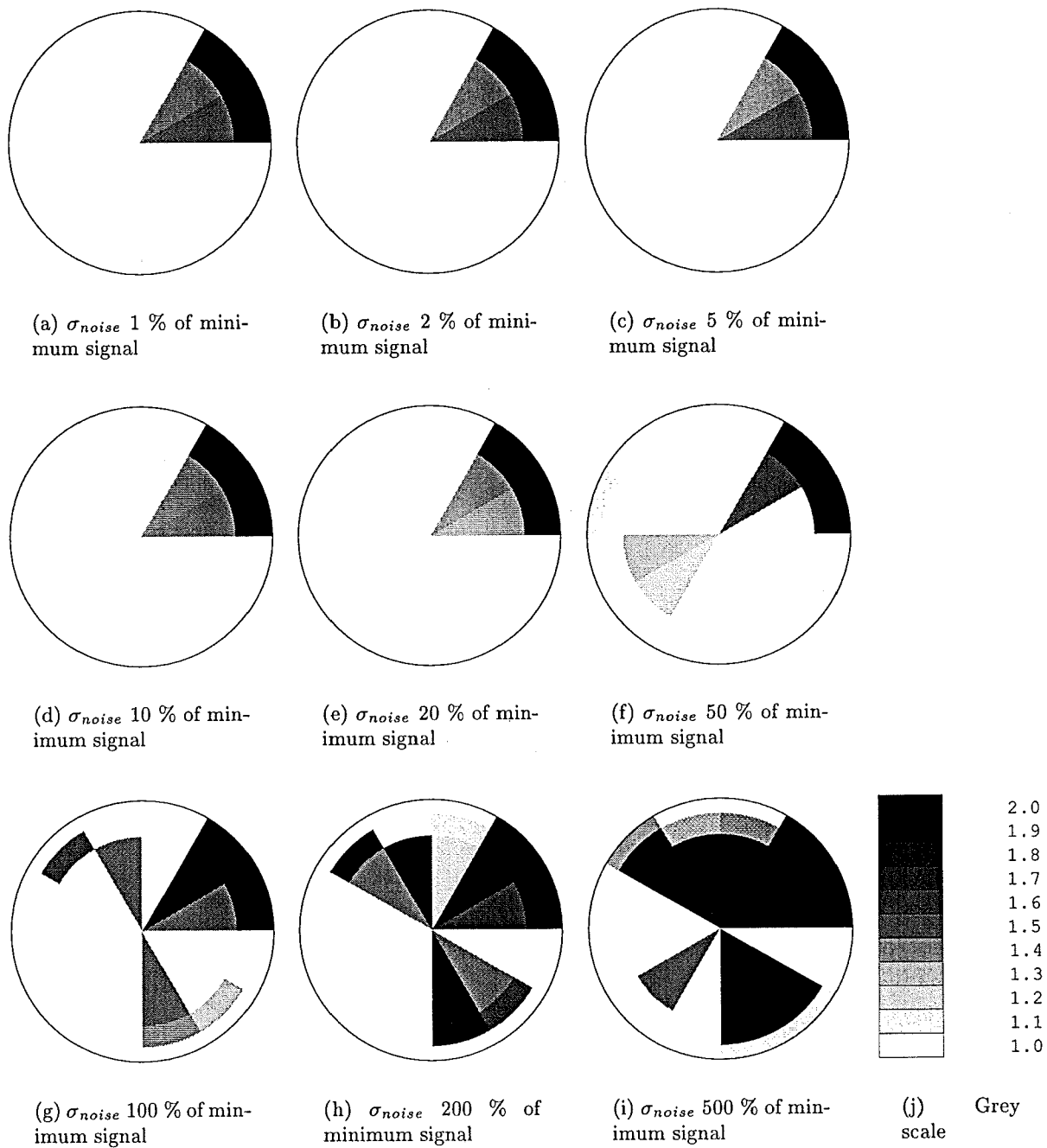


Figure A.2: plots of the reconstructed distributions using the constrained least squares method for the last 9 noise levels added to test case 2

## Appendix B

# Matlab scripts, conversion program ptl.c and circ.pl

### B.1 Matlab scripts

Total.m calculates 8 different least squares based reconstruction methods:

```
% Programma voor reconstrueren van gemeten datafiles
% met de PCECT software

% Schoonmaken matlabomgeving
clear;
close
close
close

% Opening van het programma met invoeren filename
disp('Reconstruction of measured datafiles with PCECT-software');
disp('by Joost Mulder. 25 Apr 1997');

fname = input('input Jacobian matrix (filename.dat)...','s')

fname = input('input file to be reconstructed (filename.dat)...','s')

% laden van datafiles
eval(['load ',fname,'.dat'])
eval(['load ',fname,'.dat'])
load eps_max.dat;
load eps_min.dat;
load c_min.dat
joost_c=eval(['fname'])';
```

```

load full_emp.dat;
joost_c=joost_c.*full_emp'; % Aanpassen van datafile voor de Jacobiaan
J=eval([fjname]');
x=eps_min + (eps_max-eps_min)/2;
% Openen figure 1
figure(1)

% Kleinste kwadraten oplossing
epslls=eps_min+inv(J'*J)*J'*(joost_c);
subplot(2,2,1),plot(epslls,'o')
hold on, plot(epslls), hold off
title('linear least squares solution')

% Laden dempingsmatrixen
load joost_I1.dat;
load joost_I2.dat;
R=joost_I1;
lambda=2.2E-5;

% Gedempte kleinste kwadraten oplossing
epsdlsa=eps_min+inv(J'*J+lambda*R'*R)*J'*(joost_c);
subplot(2,2,2),plot(epsdlsa), hold on, plot(epsdlsa,'o'), hold off
title('Damped Least Squares, only tangential linking')
R=joost_I2;
lambda=5.0E-6;
epsdlsb=eps_min+inv(J'*J+lambda*R'*R)*J'*(joost_c);
subplot(2,2,3),plot(epsdlsb), hold on, plot(epsdlsb,'o'), hold off
title('Damped Least Squares, radial & tangential linking')

% Laden van wegingsmatrixen
load joost_W2.dat;
load joost_W1.dat;

% Gewogen kleinste kwadraten oplossing
epswlsa=eps_min+inv(J'*joost_W1*J)*J'*joost_W1*(joost_c);
subplot(2,2,4);
plot(epswlsa,'o')
hold on
plot(epswlsa)
title('Weighted Least squares 1, diag CV matrix')
hold off

figure(2)

epswlsb=eps_min+inv(J'*joost_W2*J)*J'*joost_W2*(joost_c);

```



```
fclose(fid);

eps2dlsa=reshape(epsdlsa,12,3);
eps2dlsa=fliplr(eps2dlsa);
fid =fopen('epsdlsa.dt','w');
fprintf(fid,'%g \t %g \t %g \n %g \n',1,0.888,0.724,30);
fprintf(fid,'%f \t %f \n ',eps2dlsa);
fclose(fid);

eps2dlsb=reshape(epsdlsb,12,3);
eps2dlsb=fliplr(eps2dlsb);
fid =fopen('epsdlsb.dt','w');
fprintf(fid,'%g \t %g \t %g \n %g \n',1,0.888,0.724,30);
fprintf(fid,'%f \t %f \n ',eps2dlsb);
fclose(fid);

eps2wlsa=reshape(epswlsa,12,3);
eps2wlsa=fliplr(eps2wlsa);
fid =fopen('epswlsa.dt','w');
fprintf(fid,'%g \t %g \t %g \n %g \n',1,0.888,0.724,30);
fprintf(fid,'%f \t %f \n ',eps2wlsa);
fclose(fid);

eps2wlsb=reshape(epswlsb,12,3);
eps2wlsb=fliplr(eps2wlsb);
fid =fopen('epswlsb.dt','w');
fprintf(fid,'%g \t %g \t %g \n %g \n',1,0.888,0.724,30);
fprintf(fid,'%f \t %f \n ',eps2wlsb);
fclose(fid);

eps2dwls=reshape(epsdwls,12,3);
eps2dwls=fliplr(eps2dwls);
fid =fopen('epsdwls.dt','w');
fprintf(fid,'%g \t %g \t %g \n %g \n',1,0.888,0.724,30);
fprintf(fid,'%f \t %f \n ',eps2dwls);
fclose(fid);

eps2dwlsb=reshape(epsdwlsb,12,3);
eps2dwlsb=fliplr(eps2dwlsb);
fid =fopen('epsdwlsb.dt','w');
```



```

int    schrott;                /* variables                */
short  bin, dummy;           /* integer variables        */
char   a[30], b[20], c[20];  /* to create file names     */
FILE   *incal;               /* file with calibration data */
FILE   *indat;               /* file with capacitance data */
FILE   *out;                 /* file with image grey levels */
                                  /*******/

sprintf (a,"result/%s.asc", argv[1]);
/*sprintf (b,"data/%s.cal", argv[1]);*/
sprintf (c,"data/%s.mes", argv[1]);

/*******/
/* Error message and usage of the program: */
/*******/

if (argv[1]==0) {
printf ("      p t l\n\n");
printf ("      Program for the separation of capacitances\n");
printf ("      Upgrade by Da Mullie\n");
printf ("      Usage: ptl *1\n\n");
printf ("      *1: <filename> of files in /data without extension '.'\n");
printf ("      extension '.cal': ASCII-file with the calibration data\n");
printf ("      as produced by the ECT-system\n");
printf ("      extension '.mes': binary measurement file\n\n");
printf ("      The result is written to result/<filename>.asc\n\n");
exit(1);
}

/*******/
/* The calibration data is read: */
/*******/

/*incal = fopen (b, "r");*/
/*printf ("Reading calibration data ... \n");*/

/*******/
/* Reading the empty pipe calibration data: */
/*******/
/*fscanf (incal, "%d", &schrott);

/*for (i=0; i<11; i++) {*/
/*  for (j=0; j<11-i; j++) {*/
/*    fscanf (incal, "%f", &empty[i][j+i]);*/
/*  }*/

```

```

/*}*/
/*for (i=0; i<66; i++) {*/
/*fscanf (incal, "%d", &schrott);*/
/*}*/

/*****
/* Reading the full pipe calibration data: */
*****/

/*for (i=0; i<11; i++) {*/
/* for (j=0; j<11-i; j++) {*/
/* fscanf (incal, "%f", &full[i][j+i]);*/
/* }*/
/*}*/
/*fclose (incal);*/

out = fopen (a, "w");
indat = fopen (c,"rb");

/*****
/* Reading the total frame number: */
*****/

fread (&dummy, 2, 1, indat);

/*****
/* The first 100 frames of the measured capacitance data (66/frame) are */
/* thrown away (baseline correction): */
*****/

/* for (f=0; f<6600; f++) {*/

```

```

/* fread (&dummy, 2, 1, indat);*/
/*}*/
printf ("Reading the measured capacitances\n");

for (f=0; f<500; f++) {
/* fmax=59900                                */
  for (i=0; i<11; i++) {
    for (j=i; j<11; j++) {
      fread (&dummy, 2, 1, indat);
      swab (&dummy, &bin, 2);
      cap[i][j] = (bin)/4096.0;
/*      cap[i][j] = (bin-empty[i][j])/(full[i][j]-empty[i][j]); */
      fprintf (out,"%f\t", cap[i][j]);
    }
  }
  fread (&dummy, 2, 1, indat);
  fread (&dummy, 2, 1, indat);
  fprintf (out,"\n");
}
printf ("I am done!!!\n");
fclose (indat);
fclose (out);
}

```

### B.3 circ.pl

This Perl program converts the calculated permittivity values into a graphical representation in the reconstruction mesh:

```

#!/usr/local/bin/perl -w # --Perl--

$maxradius=100;      # radius in mm

print "!PS-Adobe-2.0\n";          # standard postscript header
print "%Creator: Martin Weiss\n";
print "%DocumentFonts: Helvetica\n";
print "%BoundingBox: 0 0 ",2*$maxradius/25.4*72," ",2*$maxradius/25.4*72," \n";
print "%Pages: 1\n";
print "%EndComments\n";
print 72/25.4," dup scale\n";      # from inch/72 to mm scale
print "$maxradius $maxradius translate\n"; # origin movement
print "0 setlinewidth\n";         # strange but necessary
@radii=split(' ',<>);             # read radial boundaries
$delta_angle=<>;                   # read delta angle

```

```
for ($row=0;$row<scalar(@radii);$row++) { # for all rows (=radii)
  @current_pixels=split(' ',<>); # read one row of pixels (R=const)
  for ($i=0;$i<scalar(@current_pixels);$i++) { # for all columns
    print(2-$current_pixels[$i]," setgray\n"); # set gray value
    print("0 0 ",$radii[$row]*$maxradius," ",$i*$delta_angle," ",
      ($i+1)*$delta_angle," arc 0 0 lineto closepath gsave fill
grestore stroke\n");
#    print "0 setgray 0.5 setlinewidth\n"; # set gray value
#    print("0 0 ",$radii[$row]*$maxradius," ",$i*$delta_angle," ",
#      ($i+1)*$delta_angle," arc 0 0 lineto closepath stroke 0
setlinewidth\n");
  }
}
print "0 setgray 0.5 setlinewidth 0 0 $maxradius 0 360 arc stroke\n";
print "showpage\n";
```



## Appendix C

# Capacitance measurements from simulations in SEPRAN

### C.1 Capacitance measurements

This Appendix describes the behaviour of the capacitance measurements from simulations in SEPRAN.

First a simulation was performed, to investigate the accuracy in the capacitance measurements. A permittivity distribution was generated with one centre pixel containing a relative permittivity of two, all the other pixels contained a relative permittivity of one (see Figure C.1).

For this permittivity distribution the Poisson equation was solved for all electrode combinations. So including for example  $C_{1-2}$  as well as  $C_{2-1}$ . From these solutions the total amount of charge, this is the same as the capacitance except for a constant, on either electrode was calculated in two different ways.

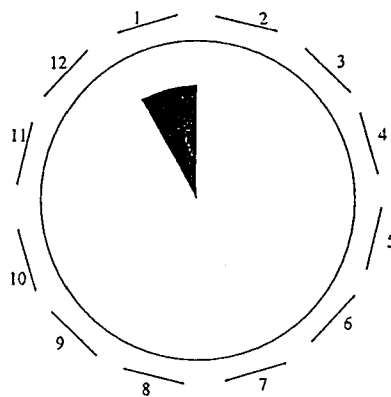


Figure C.1: Permittivity distribution in the cross-section.

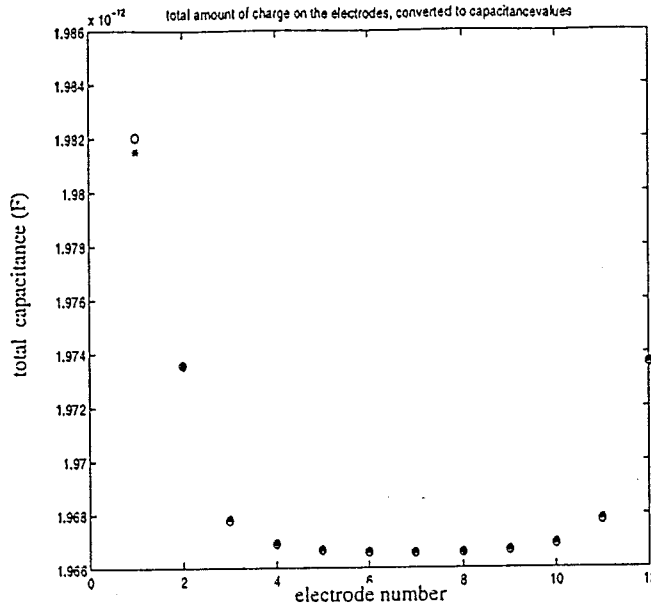


Figure C.2: The sum of charge on the different electrodes for the two different methods explained above. The '\*' refer to calculation method 1, the 'o' to calculation method 2.

1. The sum of charges on all detecting electrodes when one electrode, the source electrode, is at high potential.

$$\sum_{detector} q_{detector}^{source} \quad (C.1)$$

2. The sum of charge on a detecting electrode when all the other electrodes have been at high potential.

$$\sum_{source} q_{detector}^{source} \quad (C.2)$$

In Figure C.2 the 'total amount' of charge on the electrodes is found for the two different calculation methods. Also must be noticed that the total amount of charge on the source electrode is in fact  $\sum q_{detector} + q_{shield}$ . From these calculations we can conclude that the calculated capacitances are very accurate, except for a small error. Recently at the *Kramers Laboratorium voor Fysische Technologie* new simulations were performed using an other FEM-software package, which showed no differences in the capacitance values  $C_{ij}$  and  $C_{ji}$ . From these new simulations can be concluded that the differences found in the SEPRAN simulation stem from numerical errors and limited accuracy of the SEPRAN simulations.

We can look at the total amount of charge on one specific electrode. This is in fact the sum of charges found on all the detecting electrodes, when this specific electrode is set as source electrode high potential. In Figure C.2 we see that the total amount of charge found on the electrodes, when they are source electrode, is not a constant.

The electrodes near the pixel containing a permittivity of two, contain a bigger amount of charge than the other electrodes. Of course, when the relative permittivity distribution is constant, meaning all pixels have the same permittivity, the sum of charge on either source electrode is the same.

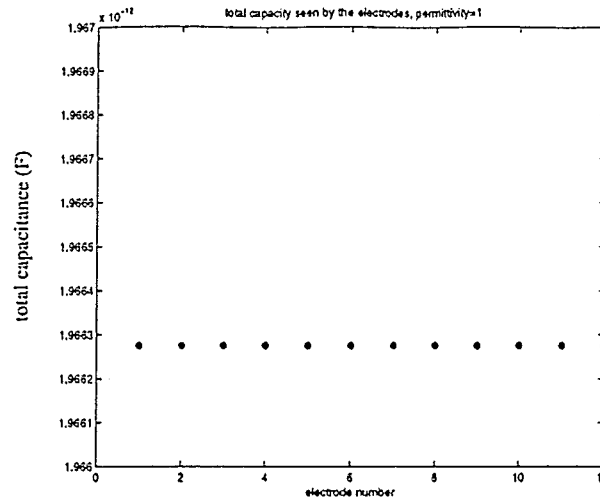


Figure C.3: The sum of charge on the different electrodes when the cross-section is filled with air (permittivity 1), converted to capacitances values. The '\*' refer to calculation method 1, the 'o' to calculation method 2.

This is evident, while the problem then contains full symmetry, and only two electrodes, thus one capacitor, had to be used (see Figure C.3).

When the constant relative permittivity of all pixels is increased several times by the same amount  $\delta\epsilon$ , all the capacitance measurements will increase linear.

In the simulation one centre pixel was increased from a permittivity one to a permittivity two with steps of 0.1. Looking at the total amount of charge found at the source electrode (see Figure C.2), this is the total charge on all the detecting electrodes and the charge found on the outer shield, we see that the total amount of charge on the source electrode is increased for every source electrode with respect to the total amount of charge found in the empty pipe situation, i.e. all pixels permittivity value of 1 (Figure C.3).

But when we look at the capacitances between two specific electrodes, we see an other effect. Looking for example to the capacitance between electrode 1 and electrode 2,  $C_{1-2}$ , and the capacitance between electrode 1 and electrode 7,  $C_{1-7}$ , we see that the capacitance  $C_{1-2}$  decreases, while pixel one is increased. On the contrary, if we look at the capacitance  $C_{1-7}$ , the capacitance increases if we increase the permittivity of pixel one (See Figure C.4).

The capacitances  $C_{1-2}$  and  $C_{1-7}$  decrease respectively increase almost linear. As explained in Chapter 4 the Jacobian matrix is calculated by finite differences,  $\frac{\Delta C_{ij}}{\Delta \epsilon_j}$ . Thus, since in Figures C.4a and b there is a small curve in both figures, the positions where the derivatives are calculated influence the Jacobian matrix.

From the figures in fig. C.4 can be seen that the capacitance between electrode one and two becomes lower than in the empty pipe, where all the pixels have permittivity one. This effect is due to the fact that the electric field depends on the permittivity distribution inside the cross-section. At the surface between two media of different permittivity the electric field lines will bend and therefore change the equipotential surfaces. This results in an electric field, which shows discontinuities at the intersection of the two media. In Figure C.5 the equipotential-lines are shown for the permittivity distribution, when one

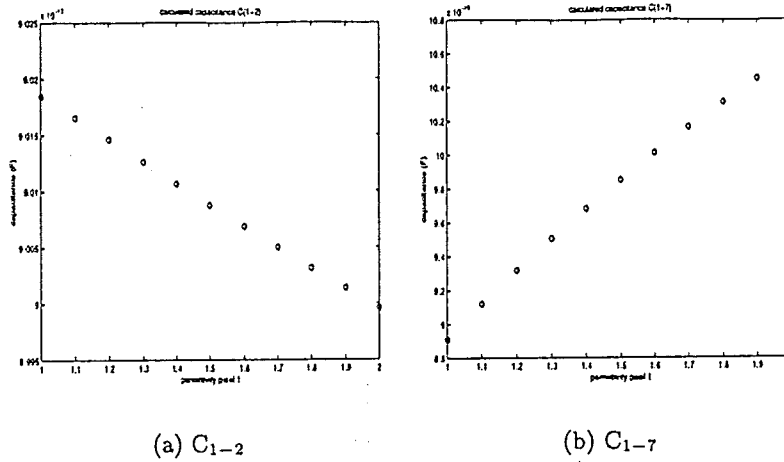


Figure C.4: Plots of the Capacitance values  $C_{1-2}$  and  $C_{1-7}$ , when one pixel is increased from a permittivity 1 to a permittivity 2 in steps of 0.1.

centre pixel is set to permittivity two and all the other pixels have permittivity one. This simulation shows that the electric field depends on the permittivity distribution. Qualitative this can be understood in the following way. In Figure C.5 electric field lines can be drawn beginning on the source electrode. In the pixel containing a permittivity of two the equipotential lines are much flatter than in the neighbour pixels. The electric field lines, which are perpendicular to the equipotential lines, will go more straight through the medium with permittivity two than in the case when this pixel had contained a permittivity of one, resulting in a bigger electric flux density in this pixel, as well.

On the contrary, when the permittivity distribution is constant over the cross-section, the electric field is not changed by different values of the permittivity over cross-section. Of course, in the latter case a linear relationship between the permittivity and the charge on the detecting electrodes is found.

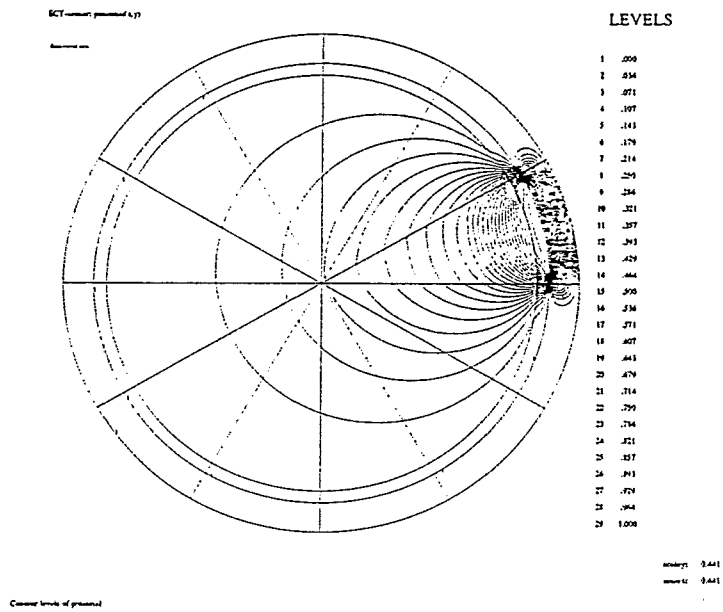


Figure C.5: Equipotential-lines for the permittivity distribution, when one centre pixel is set to a permittivity 2 in an empty pipe, i.e. all other pixel have permittivity 1.



## Appendix D

# Mesh-input file for the 16 electrode mesh

mesh2d

coarse (unit = 0.6)

points

pd1 = (0,0)

pd2 = (14.2,0)

pd3 = (15,0)

pd4 = (17,0)

pd5 = (15,2)

pd6 = (15,20.5)

pd12 = (14.2,22.5)

pd13 = (15,22.5)

pd14 = (17,22.5)

pd15 = (15,24.5)

pd16 = (15,43)

pd22 = (14.2,45)

pd23 = (15,45)

pd24 = (17,45)

pd25 = (15,47)

pd26 = (15,65.5)

pd32 = (14.2,67.5)

pd33 = (15,67.5)

pd34 = (17,67.5)

pd35 = (15,69.5)

pd36 = (15,88)

pd42 = (14.2,90)

pd43 = (15,90)  
pd44 = (17,90)  
pd45 = (15,92)  
pd46 = (15,110.5)

pd52 = (14.2,112.5)  
pd53 = (15,112.5)  
pd54 = (17,112.5)  
pd55 = (15,114.5)  
pd56 = (15,133)

pd62 = (14.2,135)  
pd63 = (15,135)  
pd64 = (17,135)  
pd65 = (15,137)  
pd66 = (15,155.5)

pd72 = (14.2,157.5)  
pd73 = (15,157.5)  
pd74 = (17,157.5)  
pd75 = (15,159.5)  
pd76 = (15,178)

pd82 = (14.2,180)  
pd83 = (15,180)  
pd84 = (17,180)  
pd85 = (15,182)  
pd86 = (15,200.5)

pd92 = (14.2,202.5)  
pd93 = (15,202.5)  
pd94 = (17,202.5)  
pd95 = (15,204.5)  
pd96 = (15,223)

pd102 = (14.2,225)  
pd103 = (15,225)  
pd104 = (17,225)  
pd105 = (15,227)  
pd106 = (15,245.5)

pd112 = (14.2,247.5)  
pd113 = (15,247.5)  
pd114 = (17,247.5)  
pd115 = (15,249.5)

pd116 = (15,268)

pd122 = (14.2,270)

pd123 = (15,270)

pd124 = (17,270)

pd125 = (15,272)

pd126 = (15,290.5)

pd132 = (14.2,292.5)

pd133 = (15,292.5)

pd134 = (17,292.5)

pd135 = (15,294.5)

pd136 = (15,313)

pd142 = (14.2,315)

pd143 = (15,315)

pd144 = (17,315)

pd145 = (15,317)

pd146 = (15,335.5)

pd152 = (14.2,337.5)

pd153 = (15,337.5)

pd154 = (17,337.5)

pd155 = (15,339.5)

pd156 = (15,358)

#### curves

c1 = cline1 (p1,p2)

c2 = cline1 (p2,p3)

c3 = cline1 (p3,p4)

c4 = carcl (p2,p12,p1)

c5 = carcl (p3,p5,p1)

c6 = carcl (p5,p6,p1)

c7 = carcl (p6,p13,p1)

c8 = carcl (p4,p14,p1)

c11 = rotate (c1,p1,p12)

c12 = rotate (c2,p12,p13)

c13 = rotate (c3,p13,p14)

c14 = rotate (c4,p12,p22)

c15 = rotate (c5,p13,p15)

c16 = rotate (c6,p15,p16)

c17 = rotate (c7,p16,p23)

c18 = rotate (c8,p14,p24)

c21 = rotate (c1,p1,p22)  
c22 = rotate (c2,p22,p23)  
c23 = rotate (c3,p23,p24)  
c24 = rotate (c4,p22,p32)  
c25 = rotate (c5,p23,p25)  
c26 = rotate (c6,p25,p26)  
c27 = rotate (c7,p26,p33)  
c28 = rotate (c8,p24,p34)

c31 = rotate (c1,p1,p32)  
c32 = rotate (c2,p32,p33)  
c33 = rotate (c3,p33,p34)  
c34 = rotate (c4,p32,p42)  
c35 = rotate (c5,p33,p35)  
c36 = rotate (c6,p35,p36)  
c37 = rotate (c7,p36,p43)  
c38 = rotate (c8,p34,p44)

c41 = rotate (c1,p1,p42)  
c42 = rotate (c2,p42,p43)  
c43 = rotate (c3,p43,p44)  
c44 = rotate (c4,p42,p52)  
c45 = rotate (c5,p43,p45)  
c46 = rotate (c6,p45,p46)  
c47 = rotate (c7,p46,p53)  
c48 = rotate (c8,p44,p54)

c51 = rotate (c1,p1,p52)  
c52 = rotate (c2,p52,p53)  
c53 = rotate (c3,p53,p54)  
c54 = rotate (c4,p52,p62)  
c55 = rotate (c5,p53,p55)  
c56 = rotate (c6,p55,p56)  
c57 = rotate (c7,p56,p63)  
c58 = rotate (c8,p54,p64)

c61 = rotate (c1,p1,p62)  
c62 = rotate (c2,p62,p63)  
c63 = rotate (c3,p63,p64)  
c64 = rotate (c4,p62,p72)  
c65 = rotate (c5,p63,p65)  
c66 = rotate (c6,p65,p66)  
c67 = rotate (c7,p66,p73)  
c68 = rotate (c8,p64,p74)

c71 = rotate (c1,p1,p72)  
c72 = rotate (c2,p72,p73)  
c73 = rotate (c3,p73,p74)  
c74 = rotate (c4,p72,p82)  
c75 = rotate (c5,p73,p75)  
c76 = rotate (c6,p75,p76)  
c77 = rotate (c7,p76,p83)  
c78 = rotate (c8,p74,p84)

c81 = rotate (c1,p1,p82)  
c82 = rotate (c2,p82,p83)  
c83 = rotate (c3,p83,p84)  
c84 = rotate (c4,p82,p92)  
c85 = rotate (c5,p83,p85)  
c86 = rotate (c6,p85,p86)  
c87 = rotate (c7,p86,p93)  
c88 = rotate (c8,p84,p94)

c91 = rotate (c1,p1,p92)  
c92 = rotate (c2,p92,p93)  
c93 = rotate (c3,p93,p94)  
c94 = rotate (c4,p92,p102)  
c95 = rotate (c5,p93,p95)  
c96 = rotate (c6,p95,p96)  
c97 = rotate (c7,p96,p103)  
c98 = rotate (c8,p94,p104)

c101 = rotate (c1,p1,p102)  
c102 = rotate (c2,p102,p103)  
c103 = rotate (c3,p103,p104)  
c104 = rotate (c4,p102,p112)  
c105 = rotate (c5,p103,p105)  
c106 = rotate (c6,p105,p106)  
c107 = rotate (c7,p106,p113)  
c108 = rotate (c8,p104,p114)

c111 = rotate (c1,p1,p112)  
c112 = rotate (c2,p112,p113)  
c113 = rotate (c3,p113,p114)  
c114 = rotate (c4,p112,p122)  
c115 = rotate (c5,p113,p115)  
c116 = rotate (c6,p115,p116)  
c117 = rotate (c7,p116,p123)  
c118 = rotate (c8,p114,p124)

```
c121 = rotate (c1,p1,p122)
c122 = rotate (c2,p122,p123)
c123 = rotate (c3,p123,p124)
c124 = rotate (c4,p122,p132)
c125 = rotate (c5,p123,p125)
c126 = rotate (c6,p125,p126)
c127 = rotate (c7,p126,p133)
c128 = rotate (c8,p124,p134)
```

```
c131 = rotate (c1,p1,p132)
c132 = rotate (c2,p132,p133)
c133 = rotate (c3,p133,p134)
c134 = rotate (c4,p132,p142)
c135 = rotate (c5,p133,p135)
c136 = rotate (c6,p135,p136)
c137 = rotate (c7,p136,p143)
c138 = rotate (c8,p134,p144)
```

```
c141 = rotate (c1,p1,p142)
c142 = rotate (c2,p142,p143)
c143 = rotate (c3,p143,p144)
c144 = rotate (c4,p142,p152)
c145 = rotate (c5,p143,p145)
c146 = rotate (c6,p145,p146)
c147 = rotate (c7,p146,p153)
c148 = rotate (c8,p144,p154)
```

```
c151 = rotate (c1,p1,p152)
c152 = rotate (c2,p152,p153)
c153 = rotate (c3,p153,p154)
c154 = rotate (c4,p152,p2)
c155 = rotate (c5,p153,p155)
c156 = rotate (c6,p155,p156)
c157 = rotate (c7,p156,p3)
c158 = rotate (c8,p154,p4)
```

#### surfaces

```
s1 = triangle3 (c1,c4,-c11)
s2 = rotate s1(c11,c14,-c21)
s3 = rotate s1(c21,c24,-c31)
s4 = rotate s1(c31,c34,-c41)
s5 = rotate s1(c41,c44,-c51)
```

```
s6 = rotate s1(c51,c54,-c61)
s7 = rotate s1(c61,c64,-c71)
s8 = rotate s1(c71,c74,-c81)
s9 = rotate s1(c81,c84,-c91)
s10 = rotate s1(c91,c94,-c101)
s11 = rotate s1(c101,c104,-c111)
s12 = rotate s1(c111,c114,-c121)
s13 = rotate s1(c121,c124,-c131)
s14 = rotate s1(c131,c134,-c141)
s15 = rotate s1(c141,c144,-c151)
s16 = rotate s1(c151,c154,-c1)

s21 = triangle3 (c2,c5,c6,c7,-c12,-c4)
s22 = rotate s21(c12,c15,c16,c17,-c22,-c14)
s23 = rotate s21(c22,c25,c26,c27,-c32,-c24)
s24 = rotate s21(c32,c35,c36,c37,-c42,-c34)
s25 = rotate s21(c42,c45,c46,c47,-c52,-c44)
s26 = rotate s21(c52,c55,c56,c57,-c62,-c54)
s27 = rotate s21(c62,c65,c66,c67,-c72,-c64)
s28 = rotate s21(c72,c75,c76,c77,-c82,-c74)
s29 = rotate s21(c82,c85,c86,c87,-c92,-c84)
s30 = rotate s21(c92,c95,c96,c97,-c102,-c94)
s31 = rotate s21(c102,c105,c106,c107,-c112,-c104)
s32 = rotate s21(c112,c115,c116,c117,-c122,-c114)
s33 = rotate s21(c122,c125,c126,c127,-c132,-c124)
s34 = rotate s21(c132,c135,c136,c137,-c142,-c134)
s35 = rotate s21(c142,c145,c146,c147,-c152,-c144)
s36 = rotate s21(c152,c155,c156,c157,-c2,-c154)

s41 = triangle3 (c3,c8,-c13,-c7,-c6,-c5)
s42 = rotate s41(c13,c18,-c23,-c17,-c16,-c15)
s43 = rotate s41(c23,c28,-c33,-c27,-c26,-c25)
s44 = rotate s41(c33,c38,-c43,-c37,-c36,-c35)
s45 = rotate s41(c43,c48,-c53,-c47,-c46,-c45)
s46 = rotate s41(c53,c58,-c63,-c57,-c56,-c55)
s47 = rotate s41(c63,c68,-c73,-c67,-c66,-c65)
s48 = rotate s41(c73,c78,-c83,-c77,-c76,-c75)
s49 = rotate s41(c83,c88,-c93,-c87,-c86,-c85)
s50 = rotate s41(c93,c98,-c103,-c97,-c96,-c95)
s51 = rotate s41(c103,c108,-c113,-c107,-c106,-c105)
s52 = rotate s41(c113,c118,-c123,-c117,-c116,-c115)
s53 = rotate s41(c123,c128,-c133,-c127,-c126,-c125)
s54 = rotate s41(c133,c138,-c143,-c137,-c136,-c135)
s55 = rotate s41(c143,c148,-c153,-c147,-c146,-c145)
s56 = rotate s41(c153,c158,-c3,-c157,-c156,-c155)
```

```
meshsurf
```

```
    selm1 = (s1,s16)
```

```
    selm2 = (s21,s36)
```

```
    selm3 = (s41,s56)
```

```
plot
```

```
end
```

# Bibliography

- Grootveld, C., 1996, Measuring and Modelling of concentrated settling suspensions using Electrical Impedance Tomography: Ph.D. thesis, Department of Chemical Engineering, Delft University of Technology, The Netherlands.
- Halow, J., and Fasching, G., 1993, Observations of a fluidised bed using capacitance imaging: *Chem. Eng. Sci.*, **48**, 643-659.
- Huang, S., Xie, C., Thorn, R., Snowden, D., and Beck, M., 1992, Disign of sensor electronics for electrical capacitance tomography: *IEE Proceedings-G*, **139**, no. 1, 83-88.
- Jackson, J., 1991, *A users's guide to principal components*: John Wiley & Sons, Inc.
- Kohn, R., and Vogelius, M., 1985, Determing conductivity by boundary measurements, ii, interior results.: *Comm. Pure Appl. Math.*, **38**, 643.
- Kühn, F., and van Halderen, P., 1997, Design of an active-differentiator-based capacitance transducer for electrical capacitance tomography: *Meas. Sci. Technol.*, **8**, 947-950.
- Kühn, F., Schouten, J., Mudde, R., van den Bleek, C., and Scarlett, B., 1996, Analysis of chaos in fluidization using electrical capacitance tomography: *Meas. Sci. Technol.*, **7**, 361-368.
- Kühn, F., 1997, Electrical Capacitance Tomography, development and application to fluidised beds: Ph.D. thesis, Department of Chemical Engineering, Delft University of Technology, The Netherlands.
- Lorrain, P., Corson, D., and Lorrain, F., 1987, *Electromagnetic Fields and Waves, Third Edition*: W.H. Freeman and Company.
- Menke, W., 1989, *Geophysical Data Analysis: Discrete Inverse Theory*: Academic press, Inc.
- Priestley, M., 1981, *Spectral Analysis and Time Series*: Academic Press Limited.
- PTL, 1996, *Electrical capacitance tomography system, type PTL300 instruction manual, issue 2*: Process tomography Ltd.
- Segal, G., 1993, *SEPRAN manuals*: Ingenieursbureau SEPRA, Leidschendam, The Netherlands.

- Silvester, P., and Ferrari, R., 1990, *Finite Elements for Electrical Engineers*: Cambridge University Press.
- Stewart, G., 1973, *Computer Science and Applied Mathematics*: Academic press, Inc.
- van Soest, J., 1992, *Elementaire statistiek*: DUM.
- Williams, R., and Beck, M., 1995, *Process Tomography*: Butterworth-Heinemann Ltd.
- Xie, C., Huang, S., Hoyle, B., R.Thorn, Lenn, C., Snowden, D., and Beck, M., 1992, Electrical capacitance tomography for flow imaging: system model for development of image reconstruction algorithms and design of primary sensors: *IEE Proceedings-G*, 139, no. 1, 89-98.